9-20-2018 1:30 PM

# A Biomechanical and Physiological Signal Monitoring System for Four Degrees of Upper Limb Movement

Allison R. Goldman, *The University of Western Ontario*

Supervisor: Trejos, Ana Luisa, *The University of Western Ontario*

A thesis submitted in partial fulfillment of the requirements for the Master of Engineering Science degree in Electrical and Computer Engineering

# Abstract

Musculoskeletal disorders (MSDs) are responsible for 3.4% of the total healthcare costs in Canada and 43% of all workplace lost-time claims and costs in Ontario. Specifically, 23% of all claims were related to the upper limb. A lack of adherence to prescribed physical therapy regimens results in improper healing; however, many societal and psychological barriers prevent proper adherence. These barriers are addressed through the system presented in this work consisting of the following components: an ambulatory biosignal acquisition sleeve, an electromyography (EMG) based motion repetition detection algorithm, and work towards the design of a compatible capacitive EMG acquisition module.

The biosignal acquisition sleeve was untethered, unobtrusive to motion, contained only modular components, and collected multi-modal sensor data. Biomechanical and physiological data were used to form full motion profiles of the following four degrees of freedom (DOF): elbow flexion—extension (EFE), forearm pronation—supination (PS), wrist flexion—extension (WFE), and ulnar–radial deviation (URD). Validation of the sleeve determined that it was able to collect information that fell within the DOFs' expected range of motion. The piloted sleeve was able to simultaneously collect data from four inertial sensors, two channels of EMG acquisition, and a flex bend sensor. A visualization application was also developed to process and present the information in an intuitive, meaningful manner.

As well, an EMG based motion repetition detector was developed for use within the system. The algorithm was developed and validated using an existing database of 23 subjects with varying musculoskeletal health. The detector was successful for 90.455% of EFE motions, 100% of PS motions, 97.5% of WFE motions, and 93.75% of URD motions. Modifications were made using inertial data to limit the detectors' search window for use with the biosignal acquisition sleeve. When tested on 15 datasets, the success rates were: 100% for EFE motion, 100% for PS motion, 95.6% for WFE, and 93.3% successful and 97.7% for URD motion.

Finally, progress was made towards the development of a non-obtrusive EMG sensing module, which could be embedded within the biosignal acquisition sleeve. Three iterations of the module were fabricated and assembled. The impacts of input bias components and bootstrap feedback were observed during benchtop testing on iteration 2; however, on-arm testing failed due to an overabundance of noise. Finally, another approach to the design was proposed, which relied upon a unique structure of materials to create the layers for sensing, guarding, shielding, and insulation techniques.

A prototype was presented of an effective, resource-conscious tool for multi-modality tracking of elbow, forearm, and wrist motion. Future work on this system would allow it to be feasibly integrating into a physical rehabilitation regimen for upper limb MSDs.

**Keywords:** Rehabilitation, musculoskeletal disorders, wearable devices, upper limb motion, body-worn sensing, electromyography, biosignals

# Acknowledgements

First and foremost, I would like to thank my supervisor, Dr. Ana Luisa Trejos for her advice, support, and endless patience. While the process took longer than I had anticipated, I appreciate that she gave me opportunity to make the most of this experience and greatly improve my technical skills. She allowed me the flexibility to make errors but provided guidance when needed to reign myself back in when necessary. I greatly appreciate her encouragement and help completing this work when I did not believe it to be capable. She truly made this experience possible and acted as a mentor for myself and the other members of the Wearable Biomechatronics Lab.

As well, I would like to acknowledge the patience and support of the past and current members of the Wearable Biomechatronics Lab. Particularly, I'd like to thank Yue Zhou and Jacob Tryon for their instruction and assistance with PCB design and teaching me techniques involved in soldering surface mount components. I'd like to thank Raneem Haddara for use of the EMG database collected over the course of her Master's thesis and Myles Lidka for assistance with the magnetic tracking system. I also want to thank Eugen Porter and Ken Strong from the Western University Electronics shop for help with component selection, use of tools, and assistance with practical circuit design.

The work of this thesis was funded by a Natural Sciences and Engineering Research Council (NSERC) by a Canada Graduate Scholarship and under grant RGPIN-2014-03815, and by the Ontario Ministry of Economic Development, Trade and Employment and the Ontario Ministry of Research and Innovation through the Early Researcher Award, and by infrastructure grants from the Canada Foundation for Innovation and the Ontario Research Fund. Additionally, Intronix Technologies Corporation is acknowledged for collaborating with the Wearable Mechatronics Lab and providing the signal conditioning unit and software suite used to collect data for the existing database used within this work.

Lastly, I'd like to thank the people who have helped me with balance throughout the process and provided me with support outside of the laboratory environment. A special thanks is extended to both old friends who have stood with me and those I have made along the way. Finally, I thank my parents, Kimberley and Gad, and my brother, Adam, for their ongoing and unconditional love and support.

# Contents

# List of Figures

# List of Tables

# Nomenclature and Acronyms

## Acronyms

| | |
|---|---|
| MSD | Musculoskeletal disorder |
| WRMSD | Work related musculoskeletal disorder |
| EBIC | Canada's Economic Burden of Illness in Canada |
| OHSCO | Occupational Health and Safety Council of Ontario |
| QHSM | Quantitative-self reporting hybrid model |
| WSIB | Workplace Safety Insurance Board |
| OA | Osteoarthritis |
| EMG | Electromyography |
| sEMG | Surface electromyography |
| ADL | Activities of daily living |
| ROM | Range of motion |
| DOF | Degrees of freedom |
| MIP | Metacarpopholangeal joint |
| PIP | Proximal interphalangeal joint |
| DIP | Distal interphalangeal joints |
| ISB | International Society of Biomechanics |
| JCS | Joint coordinate system |
| EFE | Elbow flexion–extension |
| PS | Pronation–supination |
| WFE | Wrist felxion–extension |

| | |
|---|---|
| URD | Ulnar–radial deviation |
| RUD | Radial–ulnar deviation |
| IMU | Inertial measurement unit |
| MoCap | Motion capture |
| LED | Light emitting diode |
| GPS | Global positioning sensor |
| IC | Integrated circuit |
| I2C | Inter-integrated circuit |
| SPI | Serial peripheral interface |
| MISO | Master-in slave-out |
| MOSI | Master-out slave-in |
| SCLK or SCK | Serial clock |
| TRIAD | Three-axis attitude determination |
| ABS | Acrylonitrile Butadiene Systrene |
| SD | Secure digital card |
| USB | Universal serial bus |
| RMSE | Root mean square error |
| MMG | Mechanomyography |
| CMRR | Common mode rejection ratio |
| CMR | Common mode rejection |
| ADC | Analog-to-digital converter |
| PCB | Printed circuit board |
| MCU | Microcontroller |
| LDO | Low drop-out regulator |
| IDE | Integrated development environment |
| FMA | Finite moving average |
| AGLR | Approximated generalized likelihood ratio |

| | |
|---|---|
| TKEO | Teager-Kaiser energy operator |
| V/D | Visual detection |
| DC | Direct current |
| AC | Alternating current |
| FET | Field emitting transistor |
| PWM | Pulse-width modulation |
| csv | Comma seperated variables |
| SENIAM | Surface ElectroMyoGraphy for the Non-Invasive Assessment of Muscle |
| RC | Resistor-capacitor |
| SNR | Signal to noise ration |
| EEG | Electroencephalogram |
| ECG | Electrocardiogram |
| MEMS | Micro-electro-mechancial sensing |
| AFE | Analog front end |
| Op-amp | Operational amplifier |
| In-amp | Instrumentation amplifier |
| CAD | Computer aided design |
| DTW | Dynamic time warping |
| RFI | Radio frequency interference |
| EMI | Electromagnetic interference |
| DAQ | Data acquisition |

## Variables

| | |
|---|---|
| B | Magnetic field strength |
| $\overrightarrow{M}$ | Magnetometer vector |
| $\overrightarrow{c}$ | Ellipsoid centre |
| $\widehat{U}$ | Upper triangular matrix |

| | |
|---|---|
| $\widehat{A}$ | Factorized magnetic field calibration matrix |
| $\widehat{S}$ | Normalized acceleration vector |
| $\widehat{M}$ | Normalized magnetometer vector |
| $\widehat{s}$ | Normalized gravity vector in world frame |
| $\widehat{m}$ | Normalized magnetic field vector in world frame |
| $R_{world}^{uArm}$ | Rotation matrix of the upper arm sensor orientation with respect to the world frame |
| $R_{world}^{uF}$ | Rotation matrix of the upper forearm sensor orientation with respect to the world frame |
| $R_{world}^{lF}$ | Rotation matrix of the lower forearm sensor orientation with respect to the world frame |
| $R_{world}^{Hand}$ | Rotation matrix of the hand sensor orientation with respect to the world frame |
| Q | Transformation matrix between adjacent sensors' rotation matrices |
| $R_{distal}$ | Rotation matrix of the distal sensor orientation with respect to the world frame |
| $R_{proximal}$ | Rotation matrix of the proximal sensor orientation with respect to the world frame |
| RMSE | Root mean square error |
| $n$ | Sample index |
| $\phi$ | Teagan-Kaiser energy operator |
| T | Threshold value |
| $\mu$ | Mean value of data stream |
| $\sigma$ | Variance of a data stream |
| $f$ | Frequency |
| $Z_{in}$ | Input impedance |
| $Z_{out}$ | Output impedance |
| CMRR | Common mode rejection ratio |
| $\epsilon_0$ | Permittivity in a vacuum |
| $\epsilon_R$ | Relative permittivity, with respect to free space |
| A | Area |
| d | Thickness |

## Units

| | |
|---|---|
| $^\circ$ | Degrees |
| N | Newton |
| m | Meter |
| $N \cdot M$ | Newton meter |
| Hz | Hertz |
| V | Volt |
| s | Seconds |
| samples | Samples |
| $^\circ$/s | Degrees per second |
| g | Gravity (9.81 m/s) |
| m/s | Meters per second |
| G | Gauss |
| bps | Bits per second |
| bits | Bits |
| $\Omega$ | Ohms |
| kB | kiloBytes |
| I | Ampere |
| $in^2$ | Squared inches |
| F | Farad |
| g | Gram |
| dB | decibals |

# Chapter 1

# Introduction

Musculoskeletal disorders (MSDs) are prevalent in Canadian society and have a significant negative impact. MSDs are injuries and disorders affecting the musculoskeletal system, which includes: muscles, tendons, tendon sheaths, nerves, bursa, blood vessels, joints, and ligaments. An overwhelming amount of MSDs of the upper limb are classified as work related (WRMSDs) and develop over time from the repetitive use and overuse of the arms and hands, often in an awkward fashion. Often, WRMSDs are characterized by pain, weakness, and fatigue.

Recovery from such MSDs places a significant burden on individuals, businesses, and the government. On a national level, the Public Health Agency of Canada's Economic Burden of Illness in Canada (EBIC) reports growing costs of hospital care, drugs, and physician care directly related to MSDs; in fact, these disorders' associated costs rose from $2.46 billion in 1993 [4] to $2.65 billion in 1997 [5] before arriving at $5.8 billion in 2008. In this most recent period, MSDs are the fourth most costly diagnostic category in the EBIC survey, consisting of 3.4% of all direct cost expenditures [6].

Provincially, the effects of MSDs in the workplace have been analyzed by the Occupational Health and Safety Council of Ontario (OHSCO), a council within the Ontario Ministry of Labour. OHSCO has determined that MSDs account for 41% of lost-time claims, 49% of lost-time days, and 41% of lost-time benefit claim costs between 1996 and 2003 [1]. Between 2003 and 2007, the percentage of all claims and claim costs rose to 43%, indicating the increasing pervasiveness of MSDs in the workplace [2]. The growing number of claims indicates the impact of MSDs on both the physical well-being of the Ontario workforce and the province's economic performance.

The WSIB's 2015 statistical report provides further insight into the impact of MSDs on society; here, it was found that the most frequent cause for allowed claims was bodily reaction, which are injuries resulting from external influence, and exertion, making up 36.6% of all claims. This category consists of activity that frequently causes MSDs such as: repetitive movement, over-exertion, static postures, and bodily reaction. The second and third most common causes can also be associated with musculoskeletal injuries, which were contact with objects and equipment at 28.4%, and falls at 20.8% [3].

From the same WSIB study, it is also notable that the upper extremity was found to be the body part most affected. Twenty-three percent of all claims were related to the fingers, hands, wrist, and arms [3]. Limited use of the upper limb caused by MSDs affects not only one's ability to function in the workplace, but also inhibits one's ability to perform activities of daily living, take physical care of one's self, and participate in recreational activities. The impact of upper limb related MSDs is felt greatly.

## 1.1 Motivation

The typical intervention for such MSDs is physical rehabilitation, consisting of visits with clinicians and at-home exercise regimens intended to restore the capabilities of the affected limb to its pre-disordered state. Strengthening of the limb, increasing range of motion, and reducing pain and fatigue are some of the goals achieved through adherence to such programs. To demonstrate the impact of proper regimen adherence, a study of 87 recruited patients with an MSD of the knee indicated that after 5 months patients felt an overall decrease in pain and increase in strength; however, after one year, most of the individuals had abandoned the prescribed regimen and their conditions had reverted to pre-treatment levels [7].

There are numerous reasons why a physical rehabilitation outpatient may not comply with treatment, both of physical and psychological nature. The former includes barriers, such as a low level of physical activity at the baseline and high levels of pain that inhibit movement. The latter is largely due to a lack of social support and a lack of control over their treatment.

Nevertheless, many of the existing barriers to adherence do not fit neatly into this dichotomy, as patients are unable to equate their mental and physical states. For instance, patients of Campbell's aforementioned osteoarthritis study based their decisions to quit their exercises is based on the

perception of their symptoms and the effectiveness of the treatment. Papi *et al.* also found that limited markers of progress prevented adherence to intervention regimens [8]. This fundamental gap in the patients' understanding of their condition and of the exercise content inhibits improvements in patient compliance and therefore the outcome of the treatment.

Another major segment of barriers includes those of an organizational nature. It has been found that patients with more contact time with healthcare professionals are more compliant and show more signs of recovery; however, it is challenging for many to receive that level of care. Exercises and appointments are difficult for some to incorporate into their daily routines due to constraints in: time, finances, transportation, and childcare needs [10]. To improve MSD physical rehabilitation interventions, it is clear that increased communication and remote options are essential.

Many of these adherence concerns can be mitigated through tools that allow the patients to participate in their own healthcare management. The use of wearable devices provides a possible solution through the collection of quantifiable biometrics in a non-clinical environment. This type of telemonitoring permits both clinicians and patients to retrieve objective information; furthermore, quantitative-self reporting hybrid models (QHSM) create a communication link between the involved parties through the incorporation of patients' qualitative input [9]. This model of device allows dynamic adaptations to be made to treatment plans based on the way the patient interacts in their day-to-day environment. By providing ownership and access to one's health data, patients are given a new sense of agency, a basis for self-motivation, and resultantly a catalyst for positive behavioral changes.

The impact of losses due to MSDs of the upper limb could be greatly reduced if barriers to therapy regimen adherence were reduced as well. An ambulatory tool for tracking the health and motion of the upper limb would provide a way for patients to get quantifiable metrics relating to their recovery process in the location of their convenience; thus, alleviating some of the organizational and psychological barriers to recovery.

## 1.2 Research Objectives and Scope

### 1.2.1 Research aims

The objective of this thesis is to develop an initial prototype of an effective, resource-conscious tool for multi-modality tracking of human motion of the upper limb. This is the preliminary work

towards a wearable system to be used for remote monitoring of patients with MSDs, which can be incorporated into a physical rehabilitation regimen for musculoskeletal disorders of the upper limb. The ambulatory sensor-based system will be able to be worn in a home or workplace study. It will: collect and process biometric data in order to track the motion and muscle recruitment of the patient and display information in a meaningful manner to both the user and any other interested party, such as a researcher or a clinician. The system is intended to supplement the expertise of professional healthcare providers by providing access of quantifiable data related to the MSD in an everyday environment. A low cost, simple interface and the highly accurate feedback would make the system easy to incorporate into an MSD recovery care program.

### 1.2.2 Research scope

In this work, a functional prototype of the system is presented that fulfills the requirements outlined in the research aims. The work focuses on providing biofeedback for part of the upper limb; specifically, the wrist and elbow joints, as well as the related metrics pertaining to the forearm and upper arm. The shoulder joint is not be considered at this time. For the stated joints, the system must be able to provide both biomechanical and physiological data in order to provide a well-rounded profile of the movement. The work presented in this thesis is composed of three major components, as follows:

1. A biosignal acquisition sleeve,
2. A software component to process the obtained electromyography (EMG) signals and detect individual repetitions of gross motions associated with the upper limb,
3. Work towards the design of a non-contact EMG acquisition module that can be used in conjunction with the sleeve.

An overview of these components is shown visually in Figure 1.1.

The first component, the sleeve, is intended to be a fully ambulatory, untethered wearable device that the patient is able to operate outside of a clinical environment. Measures were taken to make the sleeve modular, such that off-the-shelf sensor systems can be removed and others can be inserted in place.

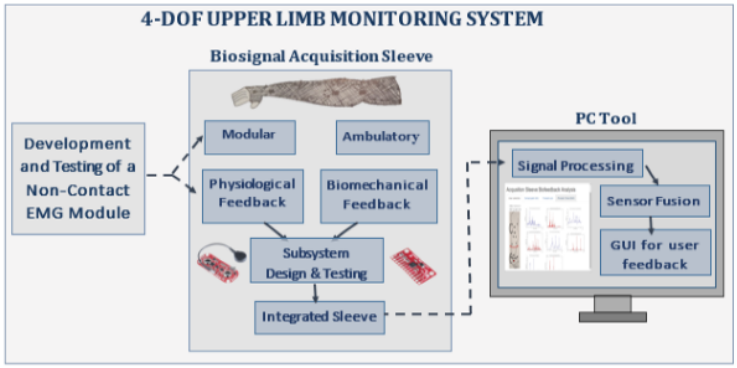


Figure 1.1: Overall system and the major components of this work.

An algorithm was developed in order to detect repetitions of motions that a patient may be prescribed in an upper limb MSD physical rehabilitation regimen. This piece of software was developed within MathWorks' MATLAB to determine onset and offset points within a EMG signal stream. The system does not provide biofeedback in real time.

A non-contact EMG acquisition system was designed to address the need for unobtrusive physiological feedback to incorporate within the sleeve. The criteria informing the module's design was based off of partial prototypes and prior art found via literature review. A low-noise, high-accuracy analog front end buffer was designed and simulated.

## 1.3 Thesis Structure

The content of this thesis is organized to represent the work-flow of the research process. Each chapter is dedicated to a major component of this work and can be outlined as follows:

**Chapter 1** Introduction: The first chapter provides context to this work, introducing the problem at hand, and discussing limitations of current treatment methods. Once the need for a new solution has been established, the research objectives and contributions are described before outlining the thesis.

**Chapter 2** Background and prior art: The intent of the second chapter is to provide a general foundation of knowledge for the reader. Due to the breadth of topics explored throughout the literature review process, this chapter will not act as a complete literature review; instead, it will be a high level overview. This chapter can be divided

into two major components: 1) The anatomy of the upper limb and related MSDs 2) Existing systems that provide biofeedback for monitoring the upper limb Analysis of this background knowledge informs the design presented later in this work. Other topic-specific prior art will be included within the relevant chapters for completeness and cohesion.

**Chapter 3** Development of the acquisition sleeve: Introduces the design of a biosignal acquisition sleeve. This chapter also walks through the development process of two individual unimodal sensor systems used to determine design requirements. These are then used to inform the integrated multimodal sleeve and its physical structure, where additional emphasis is placed on modularity.

**Chapter 4** Algorithm for detecting motion repetitions and gesture classification: This chapter first provides a partial literature review of techniques used for determining onset and offset points of EMG activity within a signal stream. Then, an algorithm was proposed to detect repetitions associated with the major gross motions of the elbow, forearm, and wrist. This algorithm is then tested and validated in two manners: firstly, on an existing EMG database, consisting of subjects with varying muscle health; and secondly, using data collected from the low-cost biosignal acquisition sleeve presented in Chapter 3.

**Chapter 5** Design and work towards the development of a non-contact EMG acquisition module: Focuses on the design of a surface electromyography module that can be used in conjunction with the developed acquisition sleeve. Here, there will be a partial literature covering various types of surface electrogmyography (sEMG) acquisition technologies, existing non-contact electrode designs, and their characteristics. The design of the module's capacitive electrode and low-noise analogue front end will be presented. Testing of a failed first prototype, a dual-pronged approach for future test modules towards the development of this module will also be included in this chapter.

**Chapter 6** Conclusions: The final chapter acts as a conclusion of the work presented, providing a brief overview, contributions to the field, and areas for future work.

# Chapter 2

# Background and Prior Art

This chapter presents relevant background information required to inform the design of the wearable upper limb monitoring tool. One of the focuses is the underlying anatomy of the upper limb, such that the expected muscle activity and movements to be observed are well understood and to provide design requirements. This information was acquired between September 2015 and May 2016 through online library services by the combining keywords including: physical rehabilitation, upper limb, elbow, wrist, forearm, biomechanics, and musculoskeletal disorders. This information makes up the content of Sections 2.1 and 2.2. The second component of this chapter focuses on prior art in the area of wearable upper limb devices. The sources pertaining to these existing systems were found between September 2015 and July 2016. Systems developed in academia were found through Google Scholar and the university library services' summon search. Commercially available systems were found through survey papers and simple search engine inquiries with the keywords: upper limb, wearable devices, monitoring, biofeedback sensing, and tracking system. This section determines commonalties, shortcomings, and gaps within the developed systems through the comparison of characteristics, such as: sensing modalities, data fusion methods, and monitored limb segments. The review informs design specifications and identifies limitations amongst the existing solutions. Further relevant information is presented at the beginning of Chapters 4 and 5.

## 2.1 Anatomy of the Upper Limb

As the intention of this work is to develop a tool to quantify metrics relating to rehabilitation of upper limb MSDs, the upper limb's anatomy is necessary to inform the device requirements. Here, the elbow, forearm, and wrist are the limb segments of focus. For each segment, the associated movements, joints, muscles, and biomechanical properties are reviewed in order to provide a basis of knowledge when designing the device, such as: methods of determining joint angles, expected ROM, and muscles with expected activity during particular motions.

### 2.1.1 Movement of the elbow

The most proximal joint segment within the scope is the elbow, which exhibits one gross motion: flexion–extension. Flexion is the bending of the elbow joint such that the angle between the forearm and upper arm decreases. Arthrokinematically, the ulna rolls and glides posteriorly on the humerus, the radius moves distally, and the radius and ulnar spread apart. During extension, the opposite phenomenon occurs. The ulna moves anteriorly, the radius moves proximally, and the two bones ultimately move closer together. This can be seen as the bending of the elbow joint resulting in a greater angle between the forearm and upper arm [11].

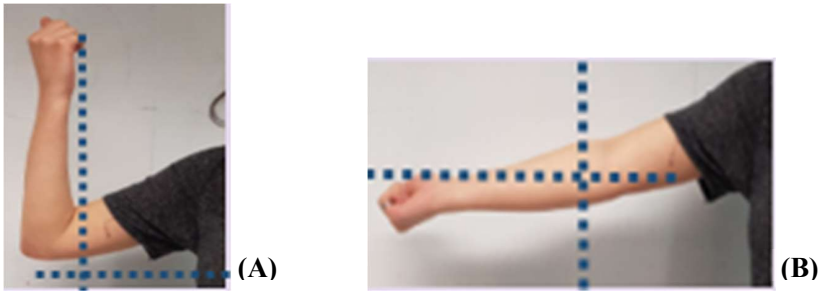


Figure 2.1: Motion of the elbow in the sagittal plane.
(A) An flexed elbow. (B) An extended elbow.

#### 2.1.1.1 Joints of the elbow

The elbow structure is a compound synovial joint composed of the humero-ulnar joint, which is located between the distal end of the humerus and the proximal end of the ulna, and the humero-radial joint, which is the articulation between the distal end of the humerus and the proximal

end of the radius. It may be considered to be a modified hinge joint, as it predominately allows motion to occur within only the sagittal plane; however, there is a deviation of the rotation axis throughout the elbow's range of motion (ROM). This unipolar motion is the flexion–extension of the elbow around the stationary medial-lateral axis of rotation, which experiences side-to-side motion and axial rotation. These additional motions are unintentional, uncontrollable, and are thus not considered as additional active degrees of freedom; as well, they do not occur directly at the elbow joint.

#### 2.1.1.2 Muscles of the elbow

Table 2.1 below displays the muscles required for the flexion–extension motion of the elbow and the corresponding label where the muscle is shown in Figure 2.2.

Table 2.1: Muscles required for elbow motion.

| **Muscle** | **Primary Purpose** | **Secondary Purpose** | **Label in Figure** |
|---|---|---|---|
| *Coracobrachialis* | Flexion | – | a |
| *Biceps brachii* | Flexion | Forearm supination | b |
| *Brachialis* | Flexion | – | c |
| *Brachioradialis* | Flexion | – | d |
| *Triceps* | Extension | – | e |

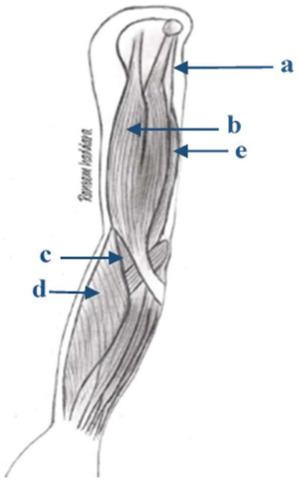


Figure 2.2: Muscles within the elbow used in flexion–extension.

### 2.1.2 Movement of the forearm

The second limb segment of interest is the forearm, which lies distal to the elbow. The gross movement associated with the forearm is the rotary pronation–supination motion, which allows the independent rotation of the hand without that of either the humerus or ulna. Pronation occurs when the radius and the hand rotate anteriorly and medially to cross over the ulna obliquely. In a fully pronated arm, the palm is facing down, as shown in Figure 2.3. Conversely, supination is the reverse motion, in which the radius returns to be lateral to the ulna and the palm ends facing up. The radius and ulna will now be parallel to one another [11].

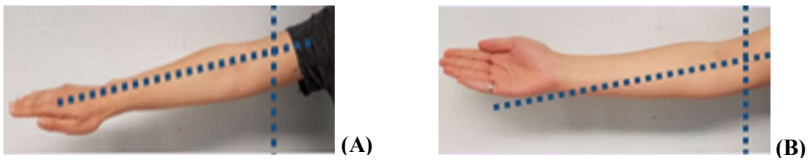


Figure 2.3: Movement of the forearm in the transverse plane.
(A) Pronation of the forearm. (B) Supination of the forearm.

#### 2.1.2.1 Joints within the forearm

The joints required for both the pronation–supination motion of the forearm are the proximal and distal radio–ulnar joints. The former is the articulation between the head of the radius and radial notch of the ulna, located near the elbow; conversely, the latter is the articulation between the ulnar notch of the radius and the ulnar head found near the wrist. Both are classified as pivot joints, as they are synovial joints allowing only rotary movement. Here, the movement axis runs from the radial head proximally to the ulnar head distally.

#### 2.1.2.2 Muscles of the forearm

Table 2.2 displays the muscles required for the pronation –supination motion of the elbow. The location of these muscles are shown in Figure 2.4.

Table 2.2: Muscles required for forearm motion.

| Compartment | Muscle | Primary Purpose | Secondary Purpose | Label in Figure |
|---|---|---|---|---|
| Superficial flexor | *Pronator teres* | Forearm pronation | Elbow flexion | a |
| Deep flexor | *Pronator quadratus* | Elbow flexion | Forearm supination | b |
| Deep extensor | *Supinator* | Forearm supination | – | c |

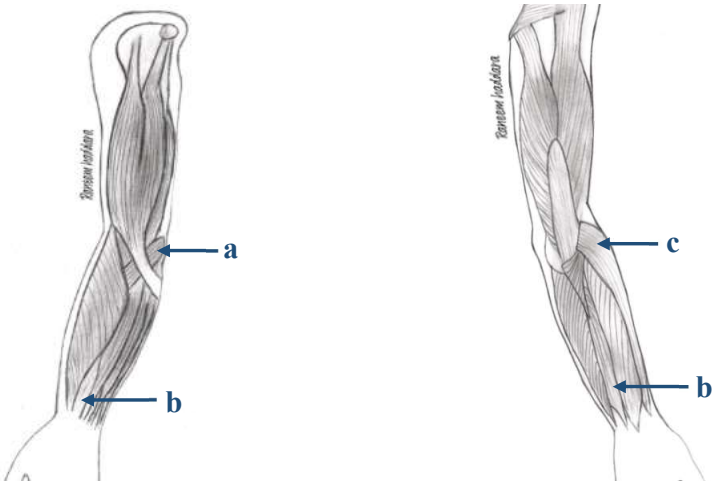


Figure 2.4: Muscles within the forearm used in pronation–supination motions.

### 2.1.3 Movement of the wrist

The final joint of interest is the wrist, which allows two major distinctive degrees of freedom that are displayed in Figures 2.5 and 2.6. One is the flexion–extension of the wrist, which is a rotation around the lateral axis proximal to the head of the capitate near the lunate and in the sagittal plane. The flexion movement is the forwards bending of the wrist; here, the scaphoid and lunate roll anteriorly and glide posteriorly along the concave surface of the radius and ulna. Conversely, the extension is the bending of the palm and fingers upwards, where the scaphoid and lunate roll posteriorly and glide anteriorly.

The other gross movement is the radial–ulnar deviation in the frontal plane. It occurs along the antero–posterior axis at the center of the capitate head and perpendicular to the axis of flexion–extension. This movement may also be referred to as the abduction–adduction of the wrist. During ulnar deviation, the scaphoid and lunate roll towards the ulna and glide towards the radius. This appears as the bending of the wrist towards the side of the hand with the thumb, which is medial

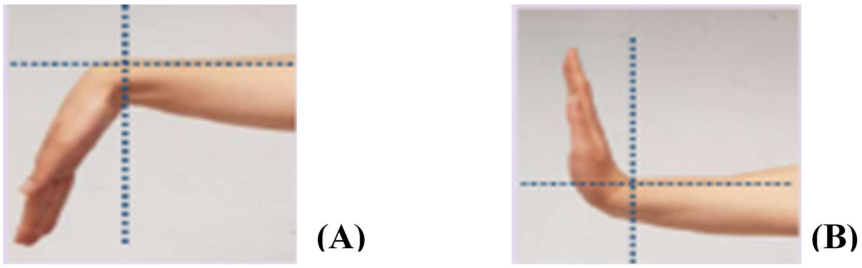


Figure 2.5: Movement of the wrist in the sagittal plane.
(A) Flexion of the wrist. (B) Extension of the wrist

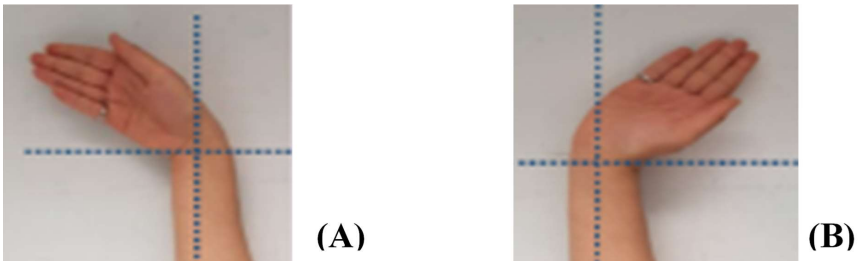


Figure 2.6: Movement of the wrist in the frontal plane.
(A) Ulnar deviation. (B) Radial deviation.

to the body from one's perspective if their palms are facing away from them. Radial deviation is the opposite motion, such that the hand bends in the opposite direction, which is lateral to the body if the palm is facing away from one in the frontal plane.

The wrist structure is composed of the radiocarpal, midcarpal, and intercarpal joints, which exist in a common synovial cavity allowing for flexion–extension, radial and ulnar deviation, and circumduction motion to be possible. As the wrist can be modeled as a condyloid joint, circular motion can be preformed; however, circumduction is the combination of flexion, extension, adduction, and abduction motions. It does not occur in a singular plane, and therefore will not be considered a gross motion in this work.

The midcarpal joint is the articulation between the proximal and distal rows of the carpal bones, which can be divided into the medial and lateral compartments. The medial compartment can be modelled as a ball-and-socket joint, in which the ball is formed by the convex head of the capitate and apex of the hamate and the socket is considered to be the convex recess formed by the scaphoid, lunate, and triquetrum bones. The midcarpal joint is primarily responsible for the wrist's flexion and radial deviation.

#### 2.1.3.1 Muscles of the wrist

Tthe muscles required for the flexion–extension and radial–ulnar deviation motions of the wrist are described in Table 2.3 [11].

Table 2.3: Muscles required for wrist motion.

| Compartment | Muscle | Primary Purpose | Secondary Purpose |
|---|---|---|---|
| Superficial flexor (forearm) | *Flexor carpi radialis* | Wrist flexion | Radial deviation |
| | *Palmaris longus* | Wrist flexion | — |
| | *Flexor carpi ulanris* | Wrist flexion | Ulnar deviation |
| | *Flexor digitorum superficialis* | Wrist flexion | Flexion of the MP[A.] and PIP[B.] joints |
| Deep flexor (forearm) | *Flexor digitorum profundus* | Wrist flexion | Flexion of the MP[A.], PIP[B.], DIP[C.] joints |
| | *Extensor carpi radialis longus* | Wrist extension | Radial deviation |
| | *Extensor carpi radialis brevus* | Wrist extension | Radial deviation |
| Superficial extensor (forearm) | *Extensor digitorum* | Wrist extension | Extension of the MP[A.], DIP[B.], and PIP[C.] joints |
| | *Extensor digiti minimus* | Digit minimus extension | Wrist extension |
| | *Extensor carpi ulnaris* | Ulnar deviation | Wrist extension |
| | *Abductor pollicus longus* | Abducts thumb | Radial deviation and thumb extension |
| Deep extensor (forearm) | *Extensor pollicus brevis* | Abducts thumb | Radial deviation and thumb extension |
| | *Extensor indicis* | Extends wrist, index finger | — |

A. MP – metacarpophalangeal, B. PIP –Interphalangeal, C. DIP –proximal interphalangeal joints

### 2.1.4 Four degrees of freedom (DOF) model of the upper limb

The elbow, forearm, and wrist of the human body can be characterized as three rigid-link segments with four degrees of freedom existing between them. These four degrees describe the elbow flexion–extension, forearm pronation–supination, wrist flexion–extension, and radial–ulnar deviation. These are shown schematically in Figure 2.7. The imperfections of the hinge joint at the elbow are unintentional and small enough to discount as an additional degree of freedom; similarly, the circumduction of the wrist can also be neglected.

In addition to the standard 4-DOF model, the International Society of Biomechanics (ISB)

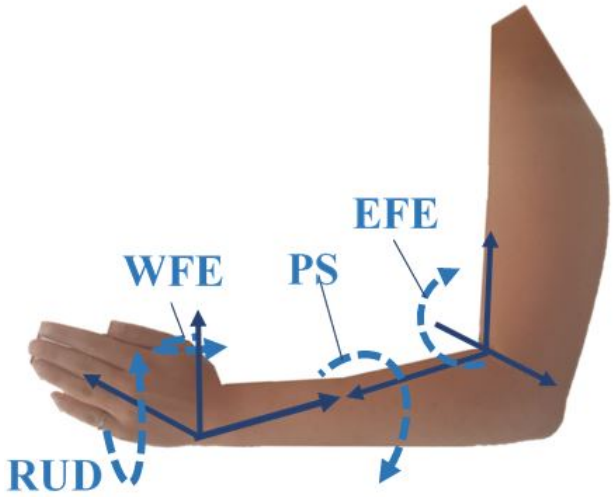


Figure 2.7: Four degree of freedom model of the elbow, forearm, and wrist, with the axis of rotation and direction shown of elbow flexion–extension (EFE), forearm pronation–supination (PS), wrist flexion–extension (WFE), and radial–ulnar deviation (RUD).

developed a standardized system of selecting joint coordinate systems (JCS) that describe human body motion.The concept was originated by Grood and Suntay [12], specifically for the knee joint, and later expanded upon by Wu *et al* [13]. This system creates a relative coordinate system between two anatomical landmarks, where the rotation angles measured between a fixed and floating axis provides information describing a particular motion; consequently, these angles form the basis of Euler or Cardan representation of the relative movement. The axes are formed as non-orthogonal unit base vectors, two of which are embedded on the anatomical bodies of interest. These axes move with the body in question to provide a relative description of motion The last axis is referred to as a floating axis, which moves with respect to the other two and is defined as a vector perpendicular to both fixed axes. Tables 2.4, 2.5, and 2.6 describes the anatomical landmarks of interest, the definitions of the JCS axes, the corresponding Cardan representation, and the practical representation of the resultant angles.

Table 2.4: ISB joint coordinate system of the elbow.

| Joint | Axis Definitions | Cardan Order | Angle Interpretations |
|---|---|---|---|
| **Elbow Fig. 2.8** | $e_1$: proximal segment, coincident with $z$ of the humerus<br>$e_3$: distal segment, coincident with $y$ of forearm<br>$e_2$: perpendicular to $e_1$ and $e_3$ | $z$, $x$, $y$ | $\alpha$: elbow flexion (+) and extension (-)<br>$\beta$: internal (+) and external (-) ulnar axial rotation<br>$\gamma$: carrying angle of the elbow |

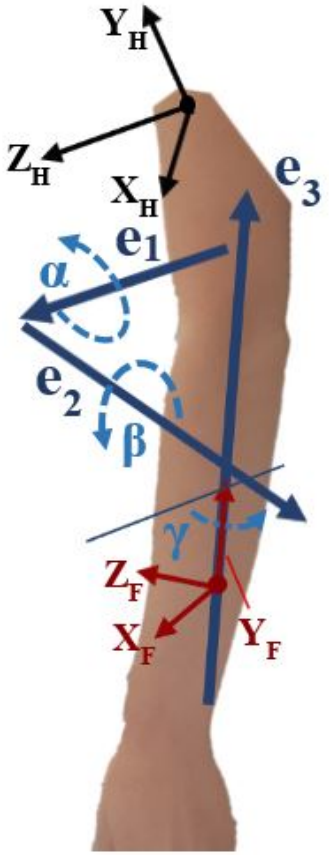


Figure 2.8: ISB joint coordinate system of elbow motion, as described in Table 2.4.

Table 2.5: ISB joint coordinate system of the forearm.

| Joint | Axis Definitions | Cardan Order | Angle Interpretations |
|---|---|---|---|
| **Forearm Fig. 2.9** | $e_1$: proximal segment, coincident with $x$ of the ulna<br>$e_3$: distal segment, coincident with $y$ of the radius<br>$e_2$: perpendicular to $e_1$ and $e_3$ | $x$, $z$, $y$ | $\alpha$: radial abduction(+) and adduction(-)<br>$\beta$: saggital rotation of the radius<br>$\gamma$: radial pronation(+) and supination(-) |

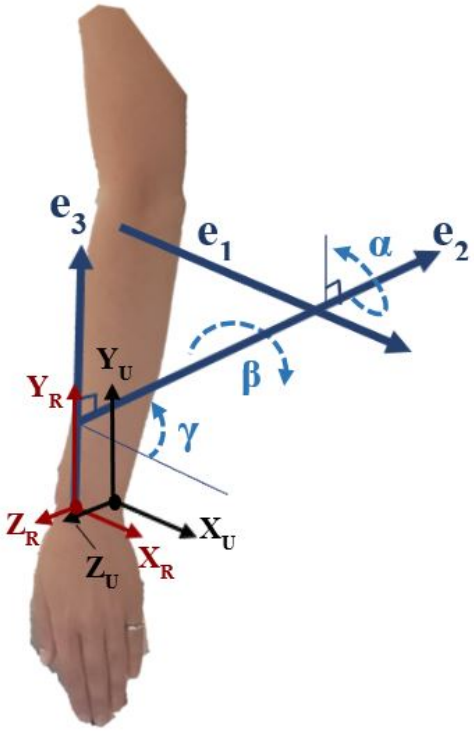


Figure 2.9: ISB joint coordinate system of forearm motion, as described in Table 2.5.

Table 2.6: ISB joint coordinate system of the wrist.

| Joint | Axis Definitions | Cardan Order | Angle Interpretations |
|---|---|---|---|
| **Wrist Fig. 2.10** | $e_1$: proximal segment, coincident with $z$ of the proximal segment's coordinate system | $x$, $y$, $z$ | $\alpha$: wrist flexion (+) and extension (-) |
| | $e_3$: distal segment, coincident with $y$ of the distal coordinate system | | $\beta$: radial (+) and ulnar (-) deviation |
| | $e_2$: perpendicular to $e_1$ and $e_3$ | | $\gamma$: forearm pronation (+) and supination (-) |

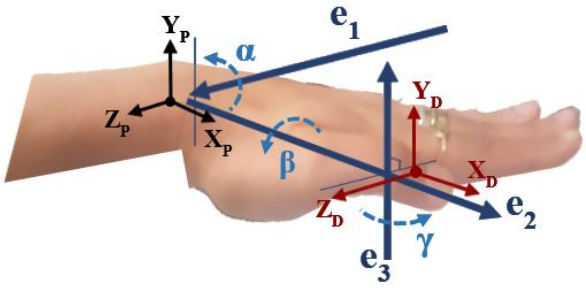


Figure 2.10: ISB joint coordinate system of wrist motion, as described in Table 2.6.

Figures 2.8, 2.9, and 2.10 correspond to the ISB JCS of the elbow, forearm, and wrist, respectively, as described in Tables 2.4, 2.5, and 2.6, respectively.

#### 2.1.4.1 Biomechanical properties of gross movements of upper arm limb segments

Particular biomechanical properties exist within a healthy human body. An understanding of these capabilities provides a set of expectations for a healthy subject and goals for an individual receiving physical rehabilitation for the upper limb; subsequently, a patient meeting these goals would indicate a completion point for therapeutic intervention. This set of biomechanical properties also provides specification for the sensors used in an upper limb tracking device. The chosen sensors must be able to represent the entirety of the expected ranges of motion and torque without aliasing to provide meaningful data.

Table 2.7: Range of motion of gross movements of the elbow, forearm, and wrist.

| **Limb Segment** | **Muscle Group** | **ROM (°)** | Active ROM (°) |
|---|---|---|---|
| Elbow | Flexion | 145 | 30 – 130 |
| | Extension | -5 | 0 |
| Forearm | Pronation | -75 | 50 |
| | Supination | 85 | 50 |
| Wrist | Flexion | 70—85 | 40 |
| | Extension | -60 – -75 | -40 |
| | Radial deviation | -15 – -20 | -10 |
| | Ulnar deviation | 35 – 40 | 30 |

Table 2.8: Torques associated with four degrees of freedom in the elbow, forearm, and wrist [11]

| **Limb Segment** | **Muscle Group** | **Mean Peak Torque (N·m)** | **Standard Deviation (N·m)** |
|---|---|---|---|
| Elbow | Flexion | 71.1 | 15.1 |
| | Extension | 41.4 | 10.7 |
| Forearm | Pronation | 7.2 | 1.8 |
| | Supination | 8.9 | 2.3 |
| Wrist | Flexion | 12.2 | 3.7 |
| | Extension | 7.1 | 2.1 |
| | Radial deviation | 11.0 | 2.0 |
| | Ulnar deviation | 9.5 | 2.2 |

## 2.2 Existing Systems

Wearable tools for physical rehabilitation of the upper limb are becoming more prevalent both in research and clinics due to recent advances in technology. Consistently, biofeedback has been made a key component in the operation of such systems, as it allows some combination of the user, healthcare professional, or the device itself to gain insight into the affected individuals' condition and respond accordingly. Tracking systems primarily focus on monitoring physiological and biomechanical signals to provide information to the user. Exoskeletons are body-worn mechatronic systems consisting of: sensors to detect the body's signals, a control system to interpret this feedback and provide instructions, and actuators that use these commands to assist the user in motion. Robotic arms have also been developed. The scope and capabilities of existing systems vary extensively. Some of these are compared in the following section.

### 2.2.1 Exoskeletons

Exoskeletons are rigid structures that provide an organism with means of support, protection, and the ability to sense its environment. This concept can be directly extended to robotic exoskeletons, which perform the same tasks to enhance the skeleton of the human during rehabilitation. These devices consist of a series of rigid links that mimic the functionality of the limb: the mechanical structures provide support to the weakened limb; sensors mimic the humans' sensory capabilities; the control system processes this information; and the actuators exert the response.

More specifically, upper limb exoskeletons are wearable systems that enact desired motion by providing the user with the necessary mechanical power. They can be used to perform rehabilitative exercises or assist in activities of daily living by producing the torque and force needed to complete these tasks without causing too much fatigue; likewise, it is important to ensure that use of the device does not have a net metabolic carrying cost on the user. In order to address this, many systems are not entirely portable but grounded or attached to a table.

To be effective, exoskeleton systems should simulate natural human motion as closely as possible, mitigating abnormal jerks and vibrations. This is an incredibly challenging task due to the complex nature of the upper limb and would require an intricate control system. Selection of actuator technology is a critical component; here, high power-to-weight ratios and back-drivability are ideal.

#### 2.2.1.1 Existing exoskeleton-based systems

Exoskeletons for the upper limb have been developed by research institutions worldwide. Although the primary goal of these devices is similar, the methods and mechanisms used to achieve this vary greatly. This is highlighted by the extensive technology reviews conducted by researchers such as Maciejasz [14], Gopura [32], and Jarrassé [15]. A subset of these existing devices are listed below in Tables 2.9, 2.10, and 2.11. Criteria for this comparison include the following: the segments of the upper arm included in the design, the number of allowed active degrees of freedom, the sensors used to retrieve physiological and biomechanical feedback from the user, and any notable features of the system's control architecture.

Table 2.9: Biofeedback in existing systems for upper limb exoskeletons.

| System | Segments Included | D.O.F. | Biomechanical Feedback | Control Techniques | |
|---|---|---|---|---|---|
| **RUPERT** Sugar [16] | Shoulder, elbow, forearm, wrist | 4 | N/A | Potentiometers (T-Noble, Model XV094N) on oulder, elbow, wrist, Analog Devices ADXL320 accelerometer on trunk | PID control |
| Udea *et al.* [17] | Elbow, forearm and wrist | 4 | surface EMG collection on *brachialis*, *brachioradialis*, and *flexor carpi ulnaris* | unspecified | Muscle–force control system computes interaction between the human muscle forces and forces generated by the exoskeleton |
| Xiao *et al.* [18] | Elbow, forearm, and wrist | 4 | Emotiv EEG headset | N/A | Joint control based on EEG activity thresholds |
| Desplenter *et al.* [19] | Elbow | 1 | Biosignalsplux wearable bodysensing platform, electrode on *biceps brachii* | N/A | EMG muscle model based control |
| Kyrylova [20] | Elbow | 1 | Biosignalsplux, lectrode on *biceps brachii* and *triceps brachii* | Biosignalsplux accelerometer on elbow | Cascade controller with PID EMG control and position-based outer loop control |
| Benitez *et al.* [21] | Elbow | 1 | BrainAmp ExG MR amplifier collects EMG from *biceps brachii* and *triceps brachii* | Baluff inductive sensor | Multi-input, single output model structures using EMG and force models |
| Kim *et al.* [22] | Elbow | 1 | Muscular stiffness force (MSF) sensor over *biceps brachii*, *triceps brachii*, and *brachioradialis* | Piezoelectric resistive sensing | Active control using recorded muscular stiffness force |

Table 2.10: Biofeedback in existing systems for upper limb exoskeletons –2.

| System | Segments Included | D.O.F. | Biomechanical Feedback | Control Techniques | |
|---|---|---|---|---|---|
| **AVSER** Wang *et al.* [23] | Elbow | 1 | Two EMG electrodes on *biceps brachii* and *triceps brachii* | Encoder to measure elbow angle | Joint–position control or force control |
| Tang *et al.* [27] | Elbow | 1 | MyoScan sEMG sensor on *biceps brachii*, *brachioradialis*, *triceps brachhi*, and *anconeus* | Potentiometer fixed to elbow joint | Proportional myoelectric control using neural networks |
| Ando *et al.* [24] | Elbow | 1 | Active AgCl electrodes on *biceps brachii* and *triceps brachii* | N/A | Use of EMG control within artificial neural networks and short-Time Fourier Transformation |
| Andrikopolous *et al.* [25] | Wrist | 2 | N/A | Spectra Symbol FS-L series linear flex sensors clamped in pairs | PID-based control |
| Xiao *et al.* [26] | Wrist | 2 | sEMG electrodes on *Extensor carpi ulnaris*, *extensor digitorum*, *palmaris longus*, and *flexor carpi ulnaris* | Torque sensor along wrist axis of rotation | Position control for passive repetitive movement, and torque control for torque amplification applications. |
| Tsagarakis and Caldwell [28] | Shoulder, elbow, forearm, wrist | 7 | N/A | Strain gauges inside pulleys of each joint form torque sensors, high-linearity position sensors | Each joint employs torque feedback control, overall system uses impedance control |
| **MGA exoskeleton** Carignan *et al.* [29] | Shoulder, elbow, forearm | 6 | N/A | JR3 force-torque sensor | Force-sensing dependent selection between shoulder-elbow admittance model and shoulder impedance model |
| **WOTAS** Rocon *et al.* [30] | Elbow, forearm, wrist | 3 | N/A | Strain gauges in full Wheatstone bridge, two accelerometers, two GYROSTAR ENC-03M surface-mount gyroscopes | Tremor suppression: active (notch filtering) and passive (impedance control) |

Table 2.11: Biofeedback in existing systems for upper limb exoskeletons – 3.

| System | Segments Included | D.O.F. | Physiological Feedback | Biomechanical Feedback | Control Techniques |
|---|---|---|---|---|---|
| **SUEFUL-7** Gopura and Kiguchi [31] [32] | Shoulder, elbow, forearm, wrist | 7 | 16 NE-101A, Nihon Kodel Co. electrodes for sEMG | Force/torque sensors, strain gauges, potentiometer | Selection between fuzzy muscle-model based EMG impedance control and/or force/ torque control |
| **(CADEN)-7** Perry and Rosen [33] | Shoulder, elbow, forearm, wrist | 7 | N/A | Midori and Fullerton potentiometers, HP encoders | unknown |
| **MAHI** Gupta [34] | Elbow, forearm, wrist | 5 | N/A | Euler angle position via encoders: US Digital E3-2048-500-H, MicroE Systems Mercury 1500, Reinshaw RGH24 | unknown |
| **RehabRoby** Ozkul *et al.* [37] | Shoulder, elbow, forearm, wrist | 6 | N/A | Kistler press force sensors | Low level admittance control with inner robust position control loop, using a discrete linear Kalman filter) and high level position control states for active-assisted, passive assistive, and passive modes). |
| **ETS-MARSE** Rahman *et al.* [35] | Shoulder, elbow, forearm, wrist | 7 | N/A | ATI, MINI40E force sensors | Nonlinear modified computed torque control |
| **ExoRob,2010** (Rahman *et al.* [36]) | elbow, forearm, wrist | 4 | N/A | Potentiometers, Nano 17, ATI 6-axis force sensor | Nonlinear sliding mode control for trajectory tracking |

### 2.2.2 Tracking systems

In addition to full exoskeleton systems, researchers have developed upper limb tracking systems. These can be used as tools to allow healthcare professionals and affected individuals to obtain biofeedback. The use of such a system can ensure that the limb is able to regain its pre-injury functionality through the frequent monitoring and correction of biomechanical and physiological properties. By pinpointing the areas in need of improvement, it is likely that the rehabilitation process can be made more effective and expedient. There are many types of sensors that can be used to implement an upper limb motion tracking system while achieving the same goal; however, the operating principle of different sensor types affects their performance in this application. Zhou's survey on human motion tracking for rehabilitation provides an overview of existing technologies, their advantages and drawbacks. Overall, they can be grouped as 'visual' or 'non-visual' tracking systems, where the former consists of optical/motion-capture systems and the latter includes: inertial based, magnetic based, and glove based systems [38].

#### 2.2.2.1 Inertial systems

Inertial systems are able to track biomechanical metrics through the use of inertial sensors. Devices such as accelerometers and gyroscopes monitor the angular acceleration, velocity and position of the limb segment. Magnetometers are often incorporated into inertial measurement units (IMUs) to measure the effect of Earth′s magnetic field to correct the heading and attach it to a fixed reference frame.

Additional body-worn sensors can also be included in human motion tracking systems to supplement the information obtained by IMUs. This may include: more mechanical feedback, such as force and torque sensors; acoustic representations of muscle movement, using ultrasonic sources and microphones; and physiological information through sEMG.

Inertial systems are generally advantageous as portable tools throughout the rehabilitation process. They are accessible due to their low cost. As well, they are light and compact, enabling them to be easily integrated into a system without impeding on the natural movement of the user. Since they are not bulky or obtrusive, the data collected is more likely to reflect the affected individual's capabilities better. They can be highly accurate and computationally efficient; however, proper sensor placement and calibration processes are essential to the system's efficacy. A major

challenge facing inertial systems is the effect of gyroscope drift, causing the orientation estimation to deteriorate over time. Most of this can be mitigated through sensor fusion techniques.

Some of the developed inertial tracking systems are listed below in Table 2.12. Measures for this comparison include: the segments of the upper arm included in the design, the number of allowed active degrees of freedom, the sensors used to retrieve physiological and biomechanical feedback from the user, and the sensor fusion algorithms employed to convert the data into a form that is meaningful to the user. Inclusion criteria for this table were as follows:

- Must describe both the biomechanical sensing and control techniques used.
- Must monitor activity from at least two of the following: elbow, forearm, or wrist.
- Tracking systems must include at least two of the following: accelerometers, gyroscopes, magnetometers, EMG acquisition modules, or ultrasonic sensors.

#### 2.2.2.2 Optical motion capture systems

On the other hand, motion Capture, or MoCap, devices record the movement of the human body or other objects using optical or magnetic sensors. These systems use multiple cameras with overlapping projections to extrapolate motion based on specific markers or features. Typically, MoCap systems are not designed for a particular structure and are more commercially available than non-optical systems. This is due to their overwhelming presence in the entertainment and military industries; in fact, some systems designed for recreation, such as the Microsoft Kinect, have been re-purposed by researchers to study human movement throughout the rehabilitation process. Optical MoCap systems can be subdivided into two categories: marker based and marker free. The use of markers indicates the points between which the system must triangulate to obtain the link′s positions; alternatively, the omission of markers causes reliance on optical sensors to dynamically track surface features.

**Visual marker based systems:** Visual marker based systems use markers as identifiers for particular structures within the limb. Information regarding the complexity of human movement is not compromised due to the ability of optical sensors to triangulate most degrees of freedom; thus, these systems are considered to be very accurate and often the "gold standard" of motion tracking [38]. However, unavailability of resources such as space and money may deter one from

Table 2.12: Biofeedback in existing systems for upper limb tracking systems

| System | Segments Included | D.O.F. | Biomechanical Feedback | Control Techniques |
|---|---|---|---|---|
| Pérez [39] | Shoulder, elbow, forearm, wrist | 6 | 4 MTi XSens inertial sensors, includes accelerometer, gyroscope, magnetometer | Controller undescribed —- handles calibration, communication, recovery |
| Zhang [40] | Shoulder, elbow, forearm | 5 | Sensor units consisting of 3-axis accelerometer, 3-axis gyroscope, magnetometer | Unscented Kalman filter geometric constraints (fusion) |
| Balbinot [42] | Shoulder, elbow, forearm, wrist | 7 | ArduIMUV3 inertial sensors (gyroscope, accelerometer, magnetometer) | Analyzes Tait Bryan angles through model generated by Make-Human and Blender |
| Hyde [43] | Shoulder, elbow, forearm, wrist | 9 | Accelerometers, gyroscopes | Composite filter, uses control over estimation accuracy as a function of frequency |
| Roetenberg [44] | Entire body (XSense MVN sensor system) | — | XSens MTx sensors (3D gyroscopes, 3D accelerometers, 3D magnetometers) | Prediction stage, where segments kinematics are estimated with inertial navigation algorithms (Kalman filter) and a correction stage based on joint kinematics, external contacts, and aiding sensors |
| Tian [45] | Elbow, forearm | 2 | interSense Inertiacube 3 IMUs each surrounded by four markers for Qualysis optical tracking system | Fusion based on strap-down IMU navigation algorithm with an unscented Kalman filter and geometric constraints |
| Bai [46] | Shoulder, elbow, forearm, wrist | 7 | XSens MTx sensors (ADXL202E biaxial accelerometers, ENC-03J single axis gyroscopes, KMZ51magneto-resistive sensors) | XKF Kalman filter for fusion, attempts single-sensor dead reckoning methods with ZUPT correction |
| Vlasic [47] | Entire body (upper limb, lower limb, neck, etc) | — | 18 sensor units consisting of: 3-axis accelerometers, 3-axis gyroscopes, microphone, 8 ultrasonic sources | Extended Kalman filter |

choosing this solution. Due to the setup of the cameras, systems are far from compact and a controlled environment is required for correct operation; as well, they are costly and computationally expensive.

Active marker based motion capture places markers with embedded LEDs on the links of a kinematic chain. Using an infrared sensor, the camera system is able to identify the markers based on their self-emitted infrared light. The position of the link segments are determined through the identification of markers based on their positions relative to one another, and triangulating the distances between them. In order to accurately resolve the three dimensional image without succumbing to occlusions, the LED markers can be illuminated individually.

Conversely, the markers used in passive optical systems do not emit their own light; instead, they incorporate retro-reflective balls. These markers reflect the light that illuminates them, which is generated by infrared emitters mounted to the motion-observing cameras. Passive markers rely on *a priori* knowledge of the relative marker placement and temporal continuity of the kinematic chain in order to mitigate ambiguities. The information observed by a single camera uses density to estimate the centroid of the marker on a two dimensional image; however, multiple cameras are required to resolve a three dimensional representation. Passive marker based systems require more time to resolve occlusions and more extensive manual cleanup on the software end in order to obtain meaningful data.

**Marker free optical tracking systems:** Marker free systems omit the use of body-worn markers in motion tracking; instead, they rely on powerful cameras to identify structures within the human body and measure the position of its linkage structures accordingly. Without dependence on markers to identify features, the sources of error associated with sensor attachment and marker visibility are mitigated. This also makes the system more compact and often less expensive. In order to retain high accuracy, complex algorithms have been developed to recognize the boundaries and features of the human body, without being limited to any number of degrees of freedom. Naturally, this becomes computationally expensive. Hardware used within the system must also support this: the cameras used must have a very high resolution and speed for effective detection.

Factors affecting the operating modalities of marker free systems include: the number of cameras and their configurations, the use of global, local, or dependence-graph-based feature selection, and the dimensionality of the model used. Two dimensional systems are only concerned with motion that takes place within a defined image plane. The 2-D method can be expanded upon

to include *a priori* knowledge of human movement in order to segment the body and to track active shape modules through background deletion. A three dimensional approach recovers articulated poses over time by representing the skeletal structure as either a stick figure or volumetric model consisting of elliptical cylinders. Time-of-flight infrared technology provides the basis for systems such as those developed by: SoftKinect [49], Organic Motion [48], and PrimeSense. This approach uses the known speed of light to measure the signal between the camera and the subject, illuminating the area with modulated infrared light to create 3-D depth maps.

The most popular 3-D marker-free system is Microsoft's Kinect [50]. Its software development kit provides the user with skeleton joint angles; as well, there are open source libraries specifically for human motion tracking such as Skeltrack [51]. As it follows, SeeMe [52], VirtualRehab [53], and Jintronix [54] have all used the Kinect platform to create commercially available systems for motion tracking, diagnostics, and therapeutic games. Additionally, academic studies have been conducted using the Kinect for motion tracking of the upper limb; for instance: Metcalf *et al.* [55] uses it for hand kinematic analysis, Tian combines the Kinect data with IMUs [45], Otten has conducted a feasibility study [56], Scano [58], and Li [57] also looked at this technology for upper limb rehabilitation.

## 2.3 Conclusions

Through this literature review, it can be determined that there is a need for the development of an additional upper limb tracking system for the purpose of monitoring physical rehabilitation from MSDs. This chapter began by reviewing the affected anatomy of the elbow, forearm, and wrist, which need attention following the occurrence of injury; here, focus was placed on the characteristics of motion that should be observed, including its angular range and active muscles. From here, existing monitoring systems and exoskeletons used in the physical rehabilitation of the upper limb were sorted according to the following criteria: limb segments analyzed, biomechanical sensing, physiological sensing, and control and sensor fusion techniques. Other monitoring techniques were explored. From the exploration of existing technologies, it appears as though a gap exists for a monitoring system for the wrist, forearm, and elbow that can be used in a non-laboratory setting with both biomechanical and physiological feedback.

# Chapter 3

# Development and Evaluation of a Biosignal Acquisition Sleeve

## 3.1 Introduction

As noted in the prior art component of the previous chapter, body-worn sensor-based systems are ubiquitous in mobile monitoring tools. This chapter focuses on the development of a biosignal acquisition sleeve for the upper limb in order to collect information relevant to MSD recovery. It discusses the ideal hardware design and an initial sleeve prototype.

The chapter begins with Section 3.2, where the initial design criteria and specifications are established. Sections 3.3 and 3.4 describe the sensor selection and the construction of single-modality sensor networks. The former, Section 3.3, will focus on biomechanical feedback while the latter, Section 3.4 centers on the acquisition of digital physiological signals. Results from each of these partial prototypes can be used to inform more specifications for the system; consequently, the microprocessor selection and integration of the subsystems into the electronics design is presented in Section 3.4. Section 3.5 describes the implementation of a preliminary sleeve prototype using primarily off-the-shelf components, as well as the physical structure of the sleeve; additionally, sample results from multi-modality sensor data collection is presented. The chapter is concluded in Section 3.7.

## 3.2 Initial Design Considerations

The goal of this work is to develop a wearable upper limb monitoring device. It should be able to acquire biometric data such that a complete profile of the user's motion is formed; principally, allowing one to track progress in the recovery of a musculoskeletal disorder. This section focuses on the creation of a signal acquisition sleeve to collect the pertinent information, outlining an initial set of specifications and the steps required to obtain additional specifications to inform the next iteration of the design. The process can be seen in Figure 3.1.

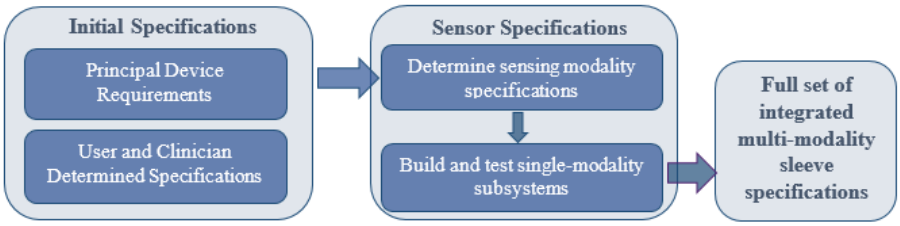


Figure 3.1: Process describing the determination of design specifications for the biosignal acquisition sleeve.

As seen above, the primary functional requirements of the device were first defined. They are outlined as follows:

1. Able to form a full motion profile of the following four degrees of freedom:
   (a) elbow flexion–extension,
   (b) forearm pronation–supination,
   (c) wrist flexion–extension, and
   (d) ulnar–radial deviation.
2. Include methods of obtaining biomechanical feedback, physiological feedback, and other sensory information required to use these data in existing research-based models of upper-limb motion.
3. Allow for modularity.
4. Be fully ambulatory and untethered; ensure that the hardware is self-contained.
5. The sleeve should be able to be reprocessed and washed.

The qualitative and psychosocial aspects of the design can also be determined prior to building any partial prototypes. Many of these can be derived through existing studies, such as the ones conducted by Bergmann and Macgregor [59], Belsi [60], and Papi *et al.* [61], which have surveyed healthcare professionals and potential users of such medical devices. By adhering to the desires of the users, compliance of the system and consequently, outcomes of physical rehabilitation, could be greatly improved. Some of these criteria are as follows:

- Users would prefer to avoid the stigmatization of using a medical device. To do so, the following conditions must be met:
  - The sleeve should be esthetically pleasing and not draw unwanted attention.
  - The sleeve should contain small and embedded sensors to reduce bulk.
  - The sleeve should be comfortable and the components should distribute the pressure.
- The device should not be obtrusive or affect one's ability to perform ADLs; its impact on motion should be minimal.
- The sleeve should be comfortable for the user to wear for prolonged periods of time.
- Operation of the sleeve should be simplistic enough to be accessible to patients and professionals.

## 3.3 Single Modality Subsystem — Biomechanical

To determine additional design specifications for the final iteration of the biosignal acquisition sleeve, single-modality sensing networks were first built and tested. The first single-modality subsystem focuses on obtaining reliable biomechanical feedback, as it is a stated requirement within the previous section. The data collected should be representative of the specific motion performed by the user. In order to determine the modality, factors including the accuracy, cost, complexity, and size of the sensors must be considered. As well, one of the sleeve's requirements is the self-containment of hardware and the ability to use the device in a variety of environments. Through a qualitative comparison of technologies in Table 3.1, it is evident that the modality most suitable for this application is the inertial measurement unit (IMU).

Table 3.1: Functional comparison of biomechanical tracking modalities.

| **Modality** | **Accuracy** | **Computational Complexity** | **Cost** | **Portability** |
|---|---|---|---|---|
| Inertial measurement unit | High | Low | Low | High |
| Optical tracking– marker | High (gold standard) | High | Mid-range | Low |
| Optical tracking– marker-free | High | High | Low | Low |
| Magnetic tracking | Mid-range | Low | Low | Mid-range |

### 3.3.1 IMU requirements and selection

To create a proper biomechanical motion profile, the IMU selected must provide representative information of the limb's orientation, position, angular velocity, and angular acceleration. Accelerometers are shown to be capable of obtaining such signals in many motion tracking studies; however, the calculation of metrics such as position are susceptible to non-negligible integration error. The main component of the signal is the acting gravitational force, such that the other parts of the signal are obscured. As well, highly accurate, linear accelerometer measurements are challenging to obtain without the use of very expensive sensors. Typically, gyroscopes are used in conjunction with accelerometers to provide an additional three degrees of freedom. Gyroscopes cannot be used independently due to the significant accumulation error, or drift, present in the signal. Still, IMUs are able to compensate for the shortcomings of the accelerometers. The drift problem can be solved through the use of additional sensors that are able to orient themselves with respect to the Earth's gravitational force, such as magnetometers or GPS sensors. The data should accurately reflect the position of the arm, such that changes in posture and the occurrences of gross motions can easily be identified, as well as compared with the expected motion. These signals should be obtained at a rate of 10 Hz, which is approximately twice the expected frequency of human motion (0–5 Hz) in accordance with Nyquist criteria.

#### 3.3.1.1 IMU component selection

Ultimately, the IMU module selected was the 9 DOF LSM9DS1 by STMicroelectronics. The IC is a package, pictured in Figure 3.2, consisting of a 3-axis linear accelerometer, a 3-axis magnetometer, and a 3-axis gyroscope. It is of relatively low cost for a commercially available 9 DOF sensor. The

IMU can be configured to operate with an *I2C*, 3 wire SPI, or 4 wire SPI communication interface. The full scale values of all three sensors can be set within the device registers to be made suitable for this application. It has a 16 bit output resolution, which is sufficient to represent the data to the desired degree of accuracy for human motion. The IMU has the ability to self-test, to enable interrupts, and to power-off particular sensors within the IC. This sort of flexibility may become beneficial later for particular testing scenarios and to support modularity within the system. The LSM9DS1 is a well-documented, well-supported integrated circuit; in fact, both SparkFun and Adafruit have released free libraries for Arduino and other common microprocessors on GitHub. This allows for minimal setup and coding, enabling rapid partial prototyping.

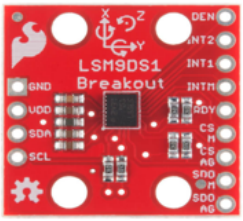


Figure 3.2: LSM9DS1 inertial measurement unit IC package.

### 3.3.2 IMU partial prototype setup

A sensor network that collected data from the IMUs was built in order to test their capabilities and to determine additional hardware specifications. Four LSM9DS1 ICs were placed along the upper limb. The sensors' placement was determined such that biomechanical information could be obtained and joint angles of the system's four DOF could be calculated. To minimize motion artefacts due to skin displacement, they were placed along the following bony structures:

- The distal end of the upper arm near the elbow,
- The proximal end of the forearm near the elbow,
- The distal end of the forearm at the base of the wrist, on the dorsal side,
- The base of the back of the hand.

The four LSM9DS1 IMUs communicate using a four wire serial peripheral interface (SPI) communication bus. Each sensor's serial data out pin is connected into the master-in slave-out

(MISO) pin in the following sensor of the chain and are returned into the master-out slave-in (MOSI) pin of the microcontroller. It was determined that these sensors do not easily support daisy-chaining, so individual chip selects were used for each sensor's accelerometer–gyroscope pair and magnetometer.

The data were collected using an Arduino Teensy 3.5 microcontroller, which was supplied with 5V through the use of a USB cable connected to a PC. The output of the microcontroller's 3.3V regulator was used to power the sensors. The script used to collect data from the sensor uses SparkFun's open source library from GitHub, and printed the data as a comma delimited list.

#### 3.3.2.1 IMU calibration and data processing

Data from the IMUs were collected on an on-board SD card and saved as comma delimited lists. The microcontroller script uses the open source LSM9DS1 library from Sparkfun. To provide accurate joint angle information, the data collected by the four inertial sensors underwent calibration and orientation estimation. A function from the SparkFun LSM9DS1 library for Arduino was used to calibrate the accelerometer and gyroscope in real time. This function determines sensor bias through the averaging of collected raw data. This bias is converted to the appropriate unit (degrees/s for the gyroscope and g for accelerometer) and removed from the current value. All values are scaled with respect to the resolution calculated from the selected sensor sensitivity.

While the magnetometer uses the same resolution scaling process, the remainder of its calibration was completed off-board using Merayo *et al.*'s method for scalar calibration of vector magnetometers using linear parameterization [62]. First, raw data is collected from the sensor using the Arduino Teensy 3.5. The sensor is moved through as many orientations and positions as possible to create a full data profile. Then, the data were saved as a comma delimited list and entered into Mathworks' MATLAB.

Here, Merayo's technique is applied, with the understanding that three orthogonal components of $B$, the magnetic field, should exist on a sphere's surface where its radius is equal to the normalized vector. The field can be expressed as follows:

$$B = \alpha_1 u_1 + \alpha_2 u_2 + \alpha_3 u_3 = \beta_1 w_1 + \beta_2 w_2 + \beta_3 w_3 \tag{3.1}$$

where $\alpha$ and $\beta$ represent the vectors' components in the orthonormal basis $[u_1, u_2, u_3]$ and the

arbitrary basis $[w_1, w_2, w_3]$, respectively, which describe the intrinsic characteristics of the sensor. The data is mapped to an ellipsoid, where calibration occurs when the following equation is minimized:

$$(\overrightarrow{M} - \overrightarrow{c})'(\widehat{U}'\widehat{U})(\overrightarrow{M} - \overrightarrow{c}) = 1. \tag{3.2}$$

Here $\overrightarrow{M}$ is the magnetometer input, $\overrightarrow{c}$ is the ellipsoid center, and $\widehat{U}$ is an upper triangular matrix that can be obtained from decomposing the ellipsoid. Through linear parameterization and Cholesky factorization, the matrix $\widehat{A}$, equal to the expression $\widehat{U}'\widehat{U}$, can be determined. Ultimately, this matrix is a three-by-three representation of the unit scaling factors required for spherical mapping of the existing data; subsequently, $\overrightarrow{c}$ is a three-by-one vector representing the offset bias. The results of the calibration are applied to future collected data sets through the following expression:

$$\widehat{A} * (\overrightarrow{M} - \overrightarrow{c}) \tag{3.3}$$

Figure3.3 shows the results of applying the ellipsoid mapping function to data collected from the four IMU sensors in every possible orientation. Equation 3.2 was used to apply the offset and scaling matrix to the raw data, resulting in the appearance of a sphere. The more "filled" and ideal-shape spheres indicate more successful calibrations. The figure also lists the values of $\widehat{A}$ and $\overrightarrow{c}$ found in the laboratory environment for the four sensors.

Following the input of collected motion data, the initial position was calculated using the three-axis attitude determination (TRIAD) algorithm [63]. The TRIAD algorithm is based on the construction of two triads of orthonormal unit vectors, which are components of the same reference frame. The multiplication of the two triads provides $\widehat{A}$, a direct cosine matrix representing the estimated initial position, which is defined as follows:

$$\widehat{A} = \left[\widehat{S} \;\vdots\; \widehat{M} \;\vdots\; \widehat{S} \times \widehat{M}\right] \left[\widehat{s} \;\vdots\; \widehat{m} \;\vdots\; \widehat{s} \times \widehat{m}\right]^T. \tag{3.4}$$

Here, $\widehat{S}$ and $\widehat{M}$ were the respective normalized accelerometer and magnetometer reading vectors in the body frame, and $\widehat{s}$ and $\widehat{m}$ were the respective normalized gravity and magnetic field vectors in the world frame.

Finally, each sensor's orientation was estimated in quaternions using the Madgwick filter [64]. This method was chosen due to its open-source code implementation, lack of complexity, relatively

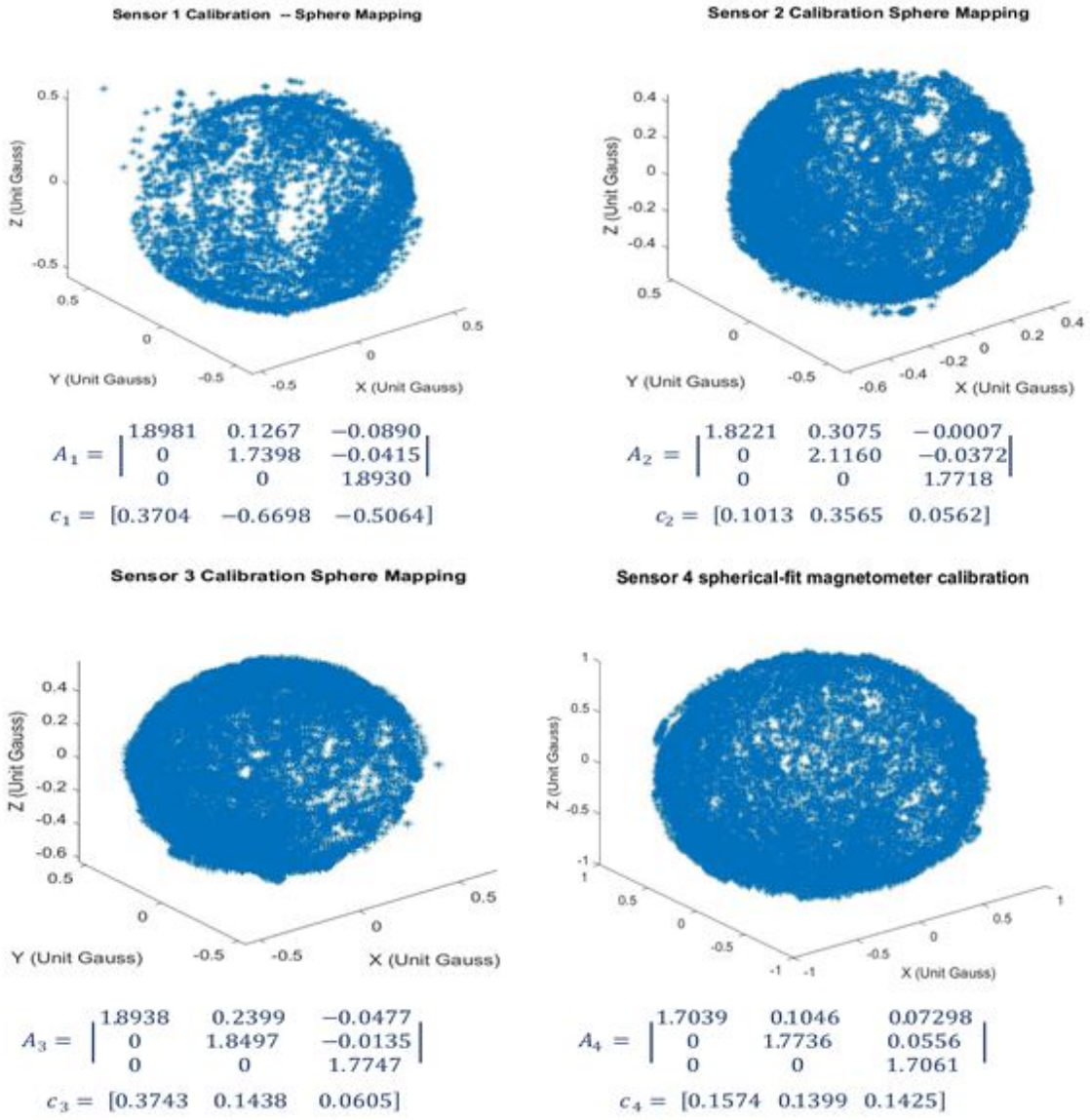


Figure 3.3: Results of the Merayo ellipsoid-to-sphere mapping calibration for each of the four LSM9DS1 IMUs.

small computational load with acccuracy comparable to Kalman-type filters. The direct cosine matrix from the TRIAD algorithm was converted to a quaternion and used as the initial position.

First, the accelerometer and magnetometer measurements were normalized. Then, these data and knowledge of the magnetic field in both the Earth and sensor frames were used as inputs to the gradient descent algorithm. The inverse Jacobian and objective functions were multiplied together and then normalized to provide the step orientation estimation. Afterwards, drift compensation

was performed through the computation of the angular gyroscope error direction, the removal of gyroscope biases, and the computation of the quaternion rate of change measured by the gyroscope.

The quaternion rate of change was found through integrating: the *a priori* estimate, the measured gyroscope quaternion, and the gradient descent estimation with unity gain factor of $\beta$. The result was normalized and the quaternion orientation was determined at the given time step.

#### 3.3.2.2 IMU partial prototype testing, results, and discussion.

This subsystem is programmed such that the representative voltages from the accelerometer, gyroscope, and magnetometer are read, converted into angular acceleration, velocity, and heading respectively through functions in existing libraries, and stored into a .csv file for further abstraction. The intent of this partial prototype is to check the efficacy of the communication protocol and the signals collected.

To accomplish the first objectives, a simple test program was used to verify the functionality of the SPI communication protocol. Through testing, it was determined that daisy-chaining the sensors was not appropriate for the collecting data from the chosen IMUs; instead, the multiple chip select method was used. It was possible to connect four LSM9DS1 sensors and use SPI communication to read the accelerometer, gyroscope, and magnetometer data at the desired sampling rate (952 Hz for accelerometers, 952 Hz for gyroscopes, and 100 Hz for magnetometers) at a baud rate of 115200 bits per second.

The efficacy of the subsystem was determined in two ways:

- Through visual analysis of the data collected while performing basic motions representing the four degrees of freedom of the elbow and wrist,
- and through the comparison of the Euler angle readings processed from each sensor to those collected simultaneously using a commercially available tracking system.

In order to observe the joint angles in the first efficacy test, the IMU data is returned and stored in terms of $x$,$y$,$z$ components of the accelerometer, gyroscope, and magnetometer data. In this verification procedure, the sensor chain was donned by the user and it was ensured that the sensors were properly located. The microcontroller was instructed to begin collecting data, initially with the user standing in an anatomically neutral position for ten seconds. The user was

asked to perform one repetition of elbow flexion–extension, forearm pronation–supination, wrist flexion–extension, and ulnar–radial deviation with three seconds between each motion type.

The data collected on the SD card was input into MathWorks' MATLAB for further processing. Here, the quaternion representation of each sensor's data were transformed into a rotation matrix. Rhe rotation matrices are as follows:

- $R_{world}^{uArm}$ , the data collected on the sensor located on the upper arm, proximal of the elbow, with respect to the world frame.
- $R_{world}^{uF}$ , the data collected on the sensor on the upper forearm arm, distal of the elbow, with respect to the world frame.
- $R_{world}^{lF}$ , the data collected on the sensor on the lower forearm arm, proximal of the wrist, with respect to the world frame.
- $R_{world}^{Hand}$ , the data collected on the sensor on the back of the hand, distal of the wrist, with respect to the world frame.

In order to determine the transformation matrix between adjacent sensors' rotation matrix, the general formula was applied:

$$Q = {R_{distal}}^{-1} R_{proximal}. \tag{3.5}$$

The transformation for each gross motion's angle is dependent on the joint coordinate system (JCS) guidelines provided by the International Society of Biomechanics. The JCS used to define the motions of interest are described in Section 2.1.4. For the elbow joint, the JCS indicates that elbow flexion–extension motion can be described across the forearm relative to the humerus in the $z$,$x$,$y$ Carden order. Equation 3.5 can first be applied to find the transformation matrix that relates the sensor data from $R_{world}^{uF}$ with respect to $R_{world}^{uArm}$ as

$$Q_{elbow} = {R_{world}^{uArm}}^{-1} R_{world}^{uF} \tag{3.6}$$

This transformation matrix can then be decomposed based on its order to yield:

$$Q_{elbow} = Q_y Q_x Q_z = \begin{bmatrix} c_\gamma & 0 & s_\gamma \\ 0 & 1 & 0 \\ -s\gamma & 0 & c_\gamma \end{bmatrix} \begin{bmatrix} 1 & 0 & 0 \\ 0 & c_\beta & -s_\beta \\ 0 & s_\beta & c_\beta \end{bmatrix} \begin{bmatrix} c_\alpha & -s_\alpha & 0 \\ s_\alpha & c_\alpha & 0 \\ 0 & 0 & 1 \end{bmatrix} \tag{3.7}$$

and then re-multiplied, resulting in the following:

$$Q_{elbow} = \begin{bmatrix} c_\gamma c_\alpha - s_\alpha s_\beta s_\gamma & -s_\gamma c_\alpha & c_\alpha s_\gamma + s_\beta s_\alpha c_\gamma \\ c_\gamma s_\alpha + c_\alpha s_\beta s_\gamma & c_\alpha c_\beta & s_\alpha s_\gamma - c_\alpha c_\gamma s_\beta \\ -c_\beta s_\gamma & s_\beta & c_\beta c_\gamma \end{bmatrix} \tag{3.8}$$

As the ISB guidelines indicate, $\alpha$ is representative of the flexion–extension joint motion.

The JCS describes the radio-ulnar joint using the motion from the radius with respect to the ulna along a *x,z,y* Carden order. Here, Equation 3.5 is applied as: $Q_{forearm} = {R^{uF}_{world}}^{-1} \cdot R^{lF}_{world}$ and then decomposed based on its order as follows:

$$\begin{aligned} Q_{forearm} = Q_y Q_z Q_x &= \begin{bmatrix} c_\gamma & 0 & s_\gamma \\ 0 & 1 & 0 \\ -s_\gamma & 0 & c_\gamma \end{bmatrix} \begin{bmatrix} c_\beta & -s_\beta & 0 \\ s_\beta & c_\beta & 0 \\ 0 & 0 & 1 \end{bmatrix} \begin{bmatrix} 1 & 0 & 0 \\ 0 & c_\alpha & -s_\alpha \\ 0 & s_\alpha & c_\alpha \end{bmatrix} \\ Q_{forearm} = Q_y Q_z Q_x &= \begin{bmatrix} c_\beta c_\gamma & -s_\beta & c_\beta s_\gamma \\ s_\alpha s_\gamma + c_\alpha c_\gamma s_\beta & c_\alpha c_\beta & c_\alpha s_\beta s_\gamma - c_\gamma s_\alpha \\ c_\gamma s_\alpha s_\beta & c_\beta s_\alpha & c_\alpha c_\gamma + s_\alpha s_\beta s_\gamma \end{bmatrix} \end{aligned} \tag{3.9}$$

Within this coordinate frame, the angle of interest is also $\alpha$, which is the pronation–supination motion.

The wrist uses a JCS that measures the sensor on the hand with respect to the sensor located on the distal side of the wrist. Using *x,y,z* Carden angles, $Q_{wrist} = {R^{lf}_{world}}^{-1} \cdot R^{hand}_{world}$ is decomposed

Table 3.2: Comparison of the mean ROM recorded from the IMU subsystem to the expected values from literature

| | **Motion** | **Recorded mean ROM (°)** | **Expected ROM (°)** |
|---|---|---|---|
| EFE | Flexion | 135.4341 | 145 |
| | Extension | -3.3802 | -5 |
| PS | Pronation | -75.2062 | -75 |
| | Supination | 82.3386 | 85 |
| WFE | Flexion | 79.0954 | 70–85 |
| | Extension | -69.8707 | -60– -75 |
| URD | Ulnar deviation | 30.7455 | 35–40 |
| | Radial deviation | -20.8011 | -15– -20 |

as:

$$
\begin{aligned}
Q_{wrist} = Q_x Q_y Q_z &= \begin{bmatrix} c_\gamma & -s_\gamma & 0 \\ s_\gamma & c_\gamma & 0 \\ 0 & 0 & 1 \end{bmatrix} \begin{bmatrix} c_\beta & 0 & s_\beta \\ 0 & 1 & 0 \\ -s\beta & 0 & c_\beta) \end{bmatrix} \begin{bmatrix} 1 & 0 & 0 \\ 0 & c_\alpha & -s_\alpha \\ 0 & s_\alpha & c_\alpha) \end{bmatrix} \\
Q_{wrist} = Q_x Q_y Q_z &= \begin{bmatrix} c_\beta c_\gamma & -c_\beta s_\gamma & s_\beta \\ c_\alpha s_\gamma + c_\gamma s_\alpha s_\beta & c_\alpha c_\gamma - s_\alpha s_\beta s_\gamma & -c_\beta s_\alpha \\ s_\alpha s_\gamma - c_\alpha c_\gamma s_\beta & c_\gamma s_\alpha + c_\alpha s_\beta s_\gamma & c_\alpha c_\beta \end{bmatrix}
\end{aligned} \tag{3.10}
$$

The guideline indicates that wrist flexion–extension motion is represented by the angle $\alpha$ and the ulnar–radial deviation is represented by $\beta$. These two angles are isolated and found as the angles representative of these gross motions.

These biomechanical representations are applied to their corresponding gross motions from the dataset collected. For each gross motion, ten data sets, consisting of three repetitions, were collected. The mean maximum and minimum values for each gross motion were recorded, interpreted, and compared to the expected ROM in Table 3.2.

As well, sample plots of each of the four specified gross motions are displayed in Figure 3.4. These new data are plotted as the joint angle, in degrees, with respect to time, in samples.

One is able to determine that the ISB based representation shows the four gross motions as expected through comparison of the obtained peak values from ten trials to the reported ROMs

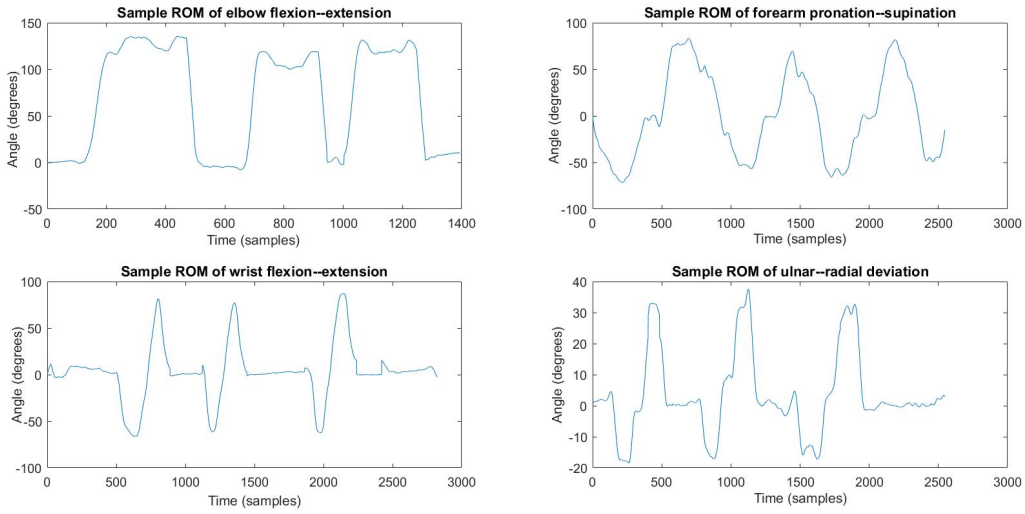


Figure 3.4: Sample plots of the range of motion obtained using the IMU subsystem, the Madgwick filter, and the ISB JCS angle decompositions.

in literature.

The second verification task uses the Aurora commercial magnetic tracking system (Northern Digital Inc. Medical, Waterloo) as a ground truth to compare the recorded values of the magnetic sensors to those collected using the IMUs. Data were logged from the Aurora and the IMU system simultaneously, using the proprietary NDI Tracker tool for the former and the SD card on-board the Arduino Teensy 3.5 for the latter. As the NDI Tracker arbitrarily defines the fourth dimension of each quaternion as zero, Euler angles were used as the basis of comparison. Since the Aurora tracking probes are only capable of tracking two degrees of freedom of rotation, two probes were required to track each sensor site. In order to track the IMU position, a small 3-D printed Acrylonitrile Butadiene Styrene (ABS) cube was affixed to the sensor. One probe was taped to the top of the cube and the other on the side, such that they are perpendicular to one another. The cube provides a physical support to hold the probes at the same angle as the sensor; additionally, it provides a slight barrier between the two sensing modalities and reducing the level of magnetic interference. The sensor–probe set up is shown in Figure 3.5.

To collect the data for comparison, a user was asked to don a sleeve with the IMUs fixed to the four aforementioned positions. The IMU with the affixed magnetic tracking probes was considered to be the IMU of interest. The user was asked to perform the four selected gross motions that involves the sensor of interest, with five seconds of rest prior to movement after both

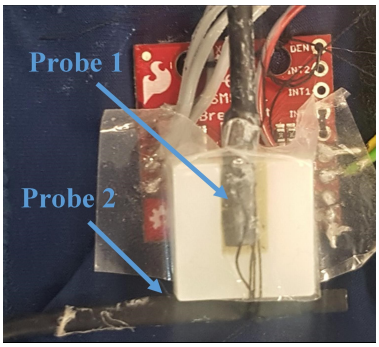


Figure 3.5: LSM9DS1 IMU with the attached ABS plastic block and two magnetic tracking probes.

the microcontroller and Aurora programs began recording. The motions were performed with the user facing forwards, towards the magnetic field generator. The orientation of the sleeve with respect to the field generator, and the directions of roll, pitch, and yaw Euler angles are shown in Figure 3.6. Following collection of all pertinent data for the sensor, the ABS block and magnetic probes were moved to a new sensor of interest, and the data collection process was repeated.

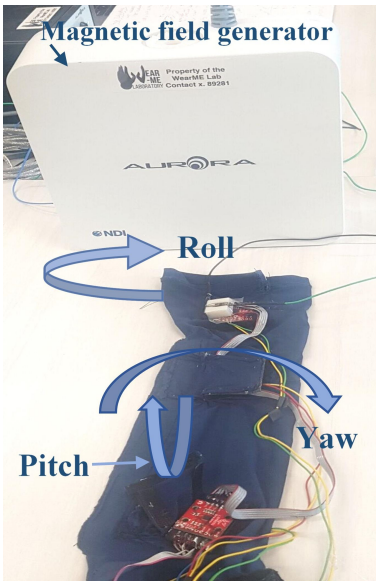


Figure 3.6: Partial set-up of the second IMU validation method, with the field generator and IMU subsystem shown. The arrows indicate the direction of roll, pitch, and yaw motion as seen by the Aurora and IMU collection systems.

Both the Aurora and IMU datasets were saved as .csv files and input to MathWorks' MATLAB. The raw 9-DOF gyroscope, accelerometer, and magnetometer data from the IMU were filtered, the data stream's initial quaternion was found using the TRIAD algorithm, and the orientation over

the collection period was estimated using the Madgwick filter. The output was then converted to Euler angles to provide a direct basis of comparison to the Aurora data. Here, the samples were first matched up based upon the five second rest period at the beginning of the collection protocol. The data stream was truncated to remove data collected before this rest period and following the return to anatomical position at the end of the trial. As the Aurora collected data at a rate of 40 Hz and the Teensy 3.5 at a rate of 100 Hz, the Aurora data were up-sampled to ensure that there were an equal number of data points for each system. The initial bias was determined to be the difference, in degrees, between the first data points of each dataset; subsequently, this initial bias level was removed for every point in the data series. After the data series were aligned, the root mean square error (RMSE) between the Euler angle values was calculated for the roll, pitch, and yaw of each motion. These RMSE values are reported in Table 3.3.

Table 3.3: RMSE of the IMU subsystem to track human motion, with respect to the NDI Aurora magnetic tracking system

| **Sensor** | **Motion** | **Axis RMSE (°)** | | |
|---|---|---|---|---|
| | | Roll | Pitch | Yaw |
| S1 | EFE | 3.3774 | 2.6061 | 6.7474 |
| S2 | EFE | 17.948 | 10.8534 | 5.118 |
| | PS | 4.4546 | missing* | 3.5311 |
| S3 | PS | 8.8853 | 4.6959 | 7.8376 |
| | WFE | 10.6168 | 5.1243 | 14.4573 |
| | URD | 0.6802 | 1.6945 | 10.6431 |
| S4 | WFE | 5.2633 | 4.3349 | 11.3678 |
| | URD | 8.0466 | 1.5983 | 2.0307 |

*Roll component of sensor 2's forearm pronation–supination omitted due to corrupted data from the corresponding magnetic tracking probe.

The reported RMSE ranges from 0.6802° to 17.948°, with the former being the roll component of the radial–ulnar deviation measured distally from the wrist and the latter being the roll component of elbow flexion–extension distally from the elbow. As they both occur along the same axis of rotation, this is unlikely due to physical error of probe placement with respect to the IMU or an error innate to the probe measurement itself. The discrepancy may be a result of the visibility of the probes to the magnetic field generator, interference between the magnetometer, magnetic tracking probes, and surrounding electronics, or alignment error between the two data

streams. While the commercial magnetic tracking system is considered to be ground truth, there are instances in the plotted data stream that appear to be the result of disturbances; as well, both systems experienced issues with data points surround the singularity points when expressed in terms of Euler angles. As some of the higher RMSE values reported in Table 3.3 are largely due to signal alignment issues, the two data streams collected for each motion are displayed in figures, as follows:

- Sensor 1, proximal to the elbow, in Figure 3.7;
- Sensor 2, distal to the elbow, in Figures 3.8 and 3.9;
- Sensor 3, proximal to the wrist, in Figures 3.10, 3.11,and 3.12; and,
- Sensor 4, distal to the wrist, in Figures 3.13, and 3.14.

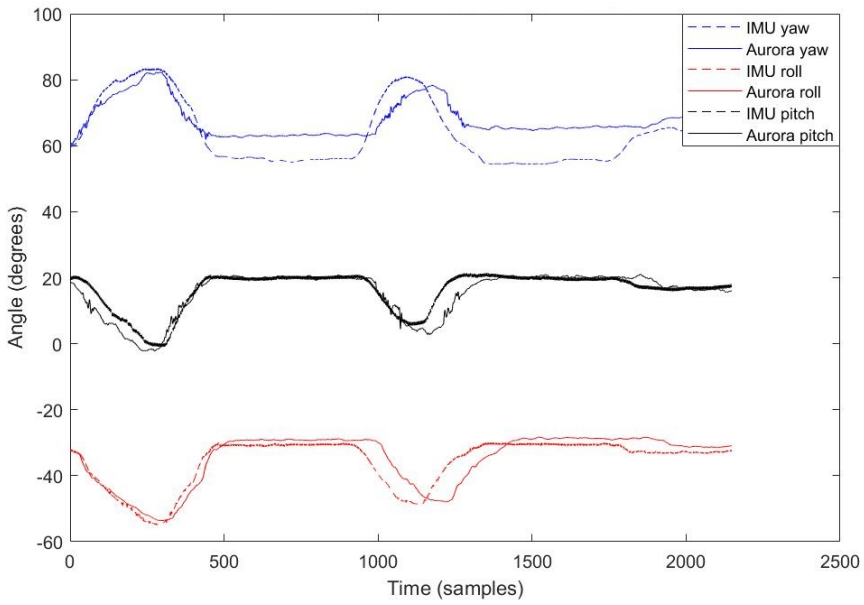


Figure 3.7: Plot comparing the Euler angles recorded by the IMU subsystem (dotted lines) and the Aurora magnetic tracking system (solid lines) during two repetitions of elbow flexion–extension, collected from the sensor proximal to the elbow. The plot displays the yaw (blue), roll (red), and pitch (black) in degrees with respect to time.

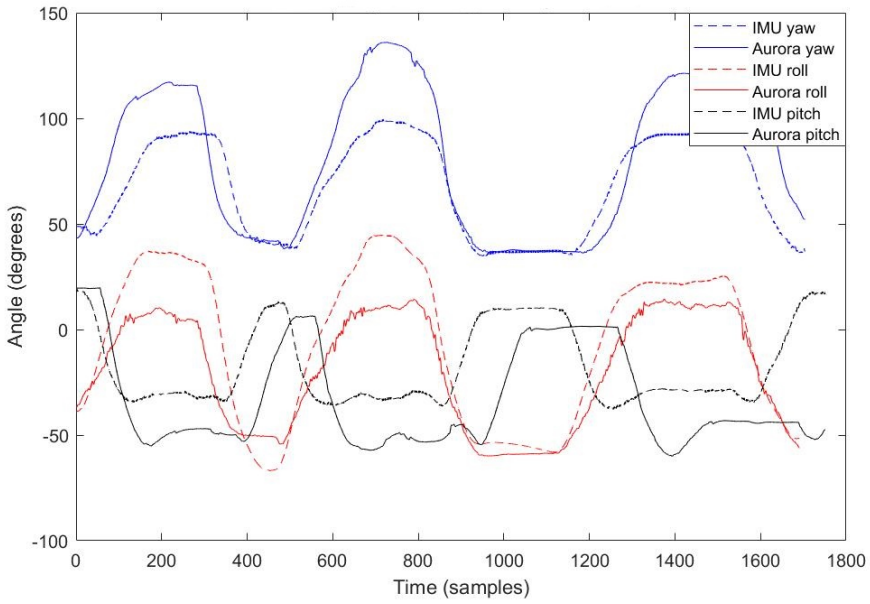


Figure 3.8: Plot comparing the Euler angles recorded by the IMU subsystem (dotted lines) and the Aurora magnetic tracking system (solid lines) during two repetitions of elbow flexion–extension, collected from the sensor distal to the elbow. The plot displays the yaw (blue), roll (red), and pitch (black) in degrees with respect to time.

Based on the findings of the first validation method, the IMU subsystem is capable of tracking and recording motion within the expected ROM. The second method of validation was able to quantify the closeness of tracking joint angles during human upper-limb motion with respect to a ground truth system.

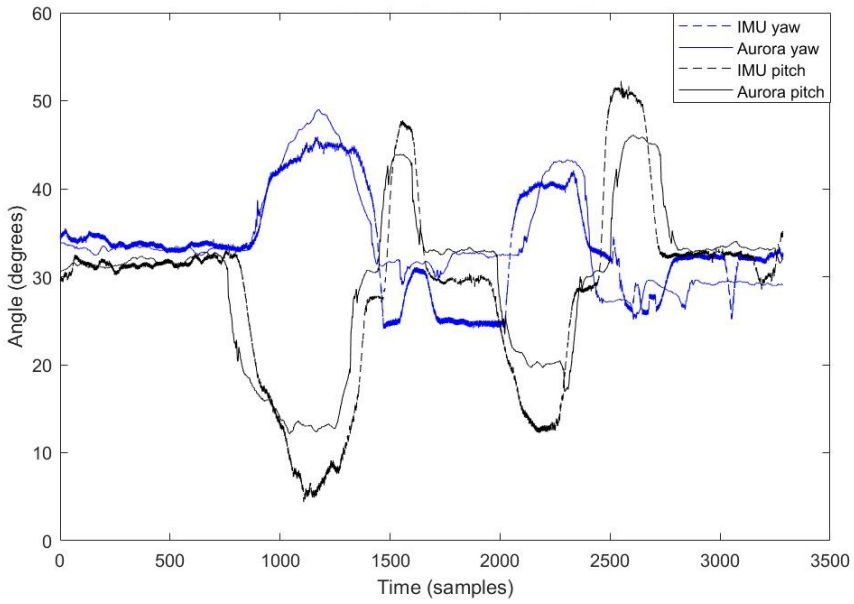


Figure 3.9: Plot comparing the Euler angles recorded by the IMU subsystem (dotted lines) and the Aurora magnetic tracking system (solid lines) during two repetitions of forearm pronation–supination, collected from the sensor distal to the elbow. The plot displays the yaw (blue) and pitch (black) in degrees with respect to time.

## 3.4 Single Modality Subsystem — Physiological

It is also stipulated that physiological feedback information can be collected through the biosignal acquisition sleeve. For insight into human upper limb motion, the pertinent physiological functions to be observed are neuro-musculoskeletal in nature; consequently, signals relating to the action potentials generated during muscle recruitment should be collected. To do so, an appropriate transducer is required to convert these raw data into a representative voltage that can later be abstracted into something meaningful.

There are three sensing modalities that have been explored for this type of physiological sensing. The first is electromyography (EMG), which is the observation of the motor neurons' electrical signals that cause muscle contractions. EMG systems typically require both an electrode to act as an interface to the human body and an analog front end to acquire the signal. This modality has been well studied; as a result, many variations of sensors and acquisition systems have been developed, allowing for flexibility within the system. The scale, accuracy, portability, and cost of the system can be controlled. More importantly, the processing of EMG signals has been

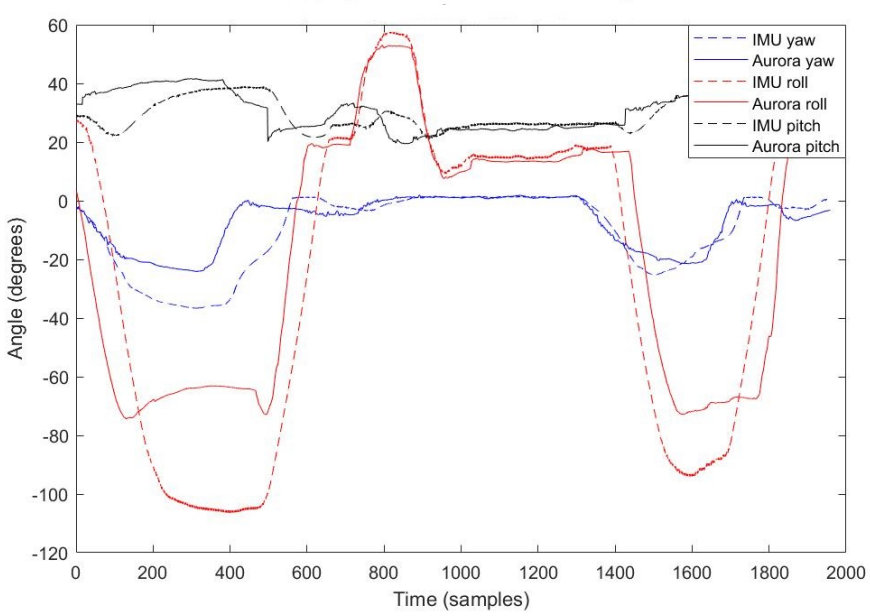


Figure 3.10: Plot comparing the Euler angles recorded by the IMU subsystem (dotted lines) and the Aurora magnetic tracking system (solid lines) during two repetitions of forearm pronation–supination, collected from the sensor proximal to the wrist. The plot displays the yaw (blue), roll (red), and pitch (black) in degrees with respect to time.

thoroughly researched such that there are numerous techniques and models with which to analyze the collected signals.

More recently, mechanomyography (MMG) has been studied as an alternative to EMG. This type of physiological sensing collects the mechanical vibrational signals that occur at the skin's surface following a muscle contraction. Easily accessible, low cost, analog sensors can be used to obtain this signal, such as accelerometers and microphones. Unlike EMG, MMG is not susceptible to changing skin impedance and excessive noise due to sensor placement; however, the low frequency range of the signals causes them to be easily obscured during dynamic movement. Between this and the lack of information available on MMG processing, it was not used within this design. Lastly, neuro-muscular information can be obtained through medical imaging techniques. Nevertheless, this modality will not be discussed or considered due its lack of portability.

#### 3.4.0.1 EMG acquisition requirements

To obtain electromyography signals from the sleeve, an appropriate module must be selected in accordance with the design criteria. One of the primary requirements is portability and unobtru-

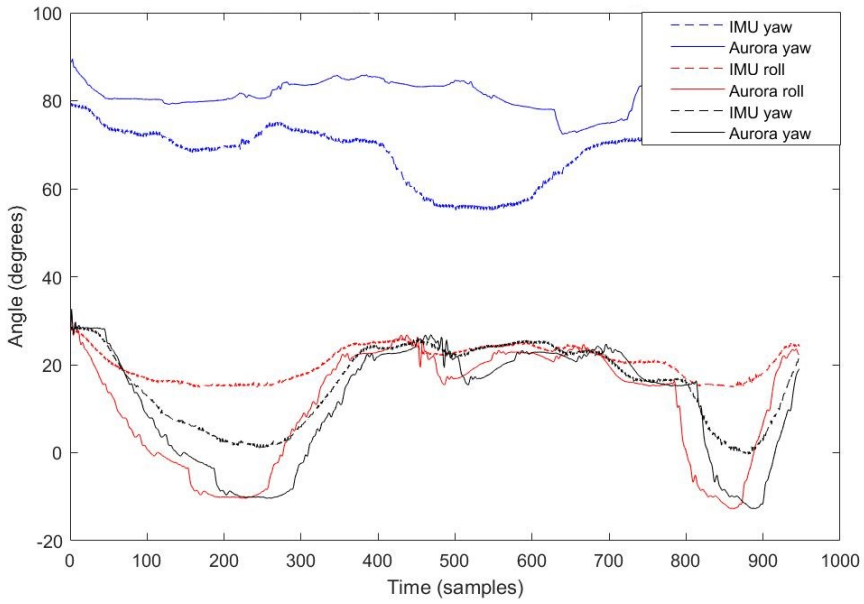


Figure 3.11: Plot comparing the Euler angles recorded by the IMU subsystem (dotted lines) and the Aurora magnetic tracking system (solid lines) during two repetitions of wrist flexion–extension, collected from the sensor proximal to the wrist. The plot displays the yaw (blue), roll (red), and pitch (black) in degrees with respect to time.

siveness; thus, limiting the capabilities of the EMG acquisition system. It should not be tethered or large, reducing the processing power and thus the number of feasible sampling sites. One of the challenges is to maintain the efficacy of the information without the need for expensive and large equipment. One important specification of the EMG module is the sampling rate. The anticipated spectrum of muscle activation signals ranges between 5 and 500 Hz; thus, the minimum acceptable sampling rate of the sensors is 1000 Hz as per the Nyquist criteria. The acquisition module should be able to limit interface noise and motion artefacts through a high common mode rejection ratio (CMRR) exceeding 90 and a high input impedance. More information on specific sensor criteria can be found in Chapter 4.

Though most EMG transducers provide an analog output, it is more desirable to have a digital representation of the signal. This can be done through the use of a suitable ADC and allows for more flexibility in device communication. Digital signals can be transmitted through the $I^2C$ or SPI bus, such that the complexity, wiring, and number of pins on the microprocessor can be reduced. Still, this ADC would require a high-resolution output to prevent decimation of the desired signal content. To prevent aliasing in the ADC conversion process, the raw EMG data

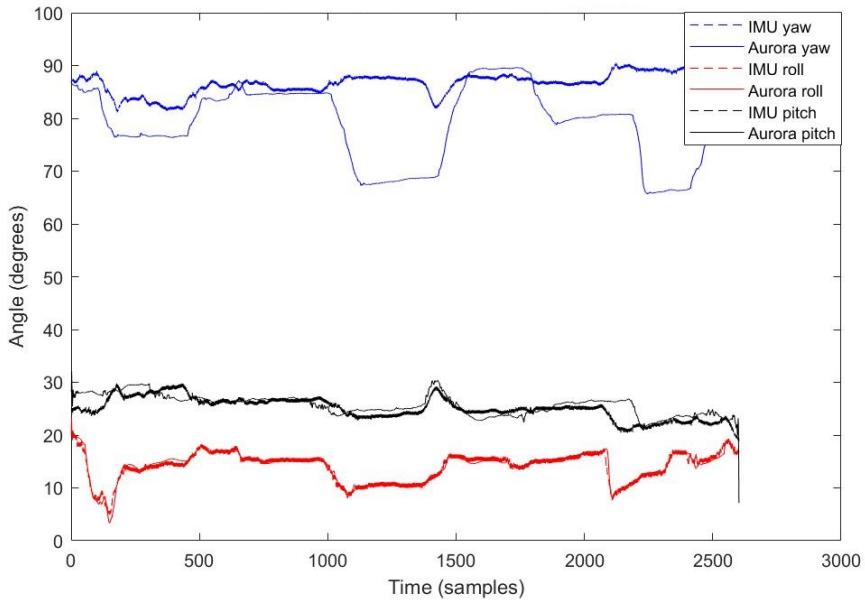


Figure 3.12: Plot comparing the Euler angles recorded by the IMU subsystem (dotted lines) and the Aurora magnetic tracking system (solid lines) during two repetitions of ulnar–radial deviation, collected from the sensor proximal to the wrist. The plot displays the yaw (blue), roll (red), and pitch (black) in degrees with respect to time.

should be collected and stored for later processing.

#### 3.4.0.2 EMG module component selection

For the initial prototype, the Advancer Technology's MyoWare Muscle Sensor was one of the modules used to collect the EMG signals within the acquisition sleeve. This is a commercially available component that acts as a self-contained module. It can be connected to a microcontroller-based existing system without the need for an additional full hardware system and software suite. It is small, unobtrusive, and untethered to an external base unit. Through a cursory search of online retailers such as Digikey, Sparkfun, RobotShop, and Canada Robotix, it does not appear as though there are other devices available that fulfill this criteria; though other technologies considered, such as the Delsys Trigno Mini, were unavailable or too costly. The module is relatively inexpensive and easy to incorporate into the sleeve, making it possible for users to make application-specific modifications.

The MyoWare acts as the analog front end of the collection module, which is capable of providing either a raw or enveloped version of the signal to a microprocessor. The MyoWare's gain

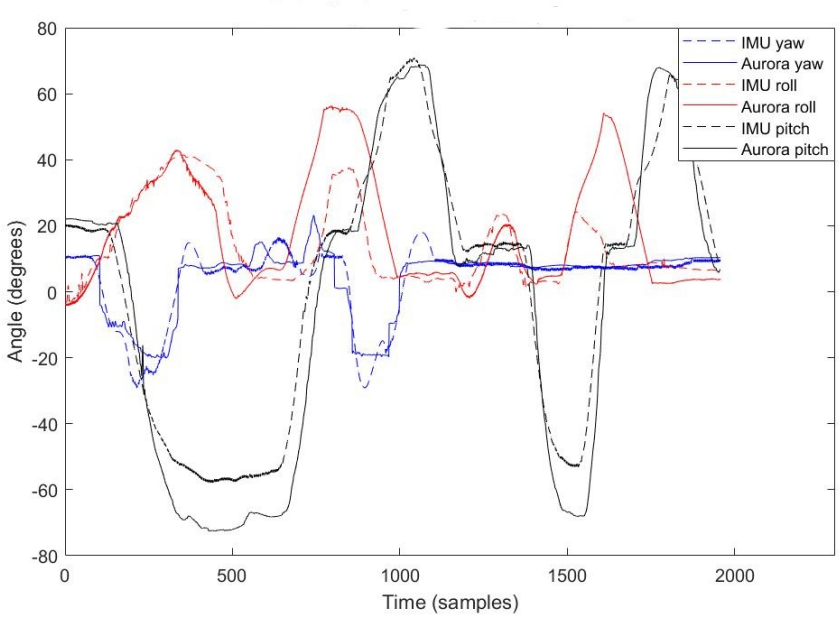


Figure 3.13: Plot comparing the Euler angles recorded by the IMU subsystem (dotted lines) and the Aurora magnetic tracking system (solid lines) during two repetitions of wrist flexion–extension, collected from the sensor distal to the wrist. The plot displays the yaw (blue), roll (red), and pitch (black) in degrees with respect to time.

is adjustable such that it can be tailored to provide high quality outputs for the desired muscles. As well, it has an acceptably high CMRR of 110 and an input impedance of 110 GΩ.

It only requires a low voltage, 3.3 V, single supply, making it simple to integrate into a sensor network. The module contains two snaps in order to form a bipolar electrode configuration, where a differential amplifier can remove the common mode component of the signal across the muscle belly. The snaps allow one to interchange the types of electrodes used in the spirit of modularity.

#### 3.4.0.3 ADC component selection

Unlike the MyoWare muscle sensors, the ADCs they will be connected to are not designed to be interchangeable. The ADCs are responsible for conversion and transmission of the A/C EMG signal; due to the complexity and particularity of this procedure, modularity here would require changes in both hardware and software that would be too challenging for the typical user to implement.

The ADC package selected for the biosignal acquisition sleeve is Texas Instruments ADS129X series. This device has an above-average output resolution of 32 bits, ensuring that none of the

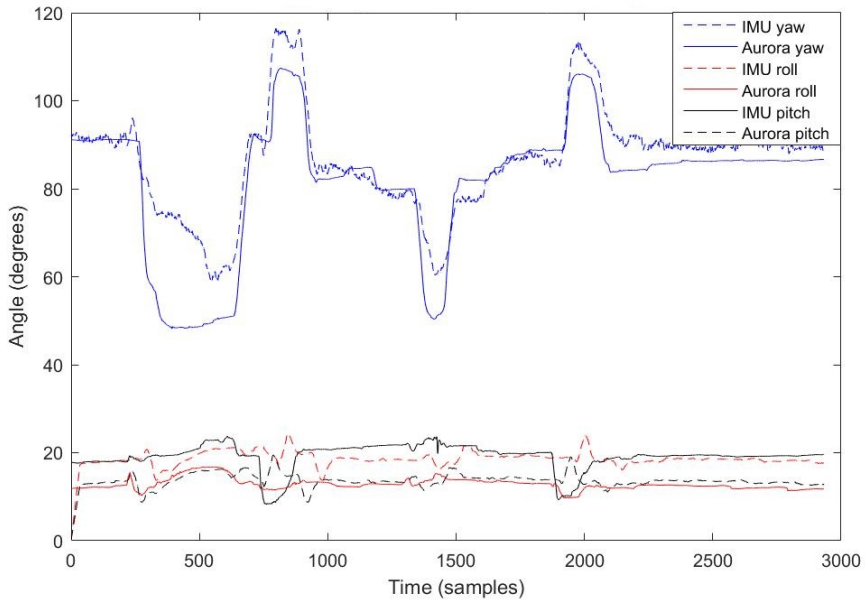


Figure 3.14: Plot comparing the Euler angles recorded by the IMU subsystem (dotted lines) and the Aurora magnetic tracking system (solid lines) during two repetitions of radial–ulnar deviation, collected from the sensor distal to the wrist. The plot displays the yaw (blue), roll (red), and pitch (black) in degrees with respect to time.

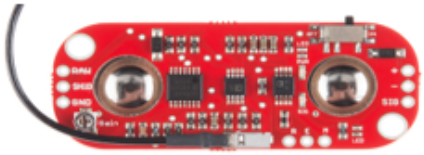

Figure 3.15: MyoWare EMG acquisition module.

information is obscured by noise in the digitization process. This inherently allows for the collection of raw signals, such that no filtering is necessary in the hardware. The ADS1292R is a medical grade device and has features that reflect this, such as: a right-leg drive, to reduce the common mode noise; lead detection, to ensure the electrode leads are connected properly; and a temperature sensor, to provide data that may be necessary in some muscle models. It also supports the SPI communication protocol, such that wiring and complexity are reduced.

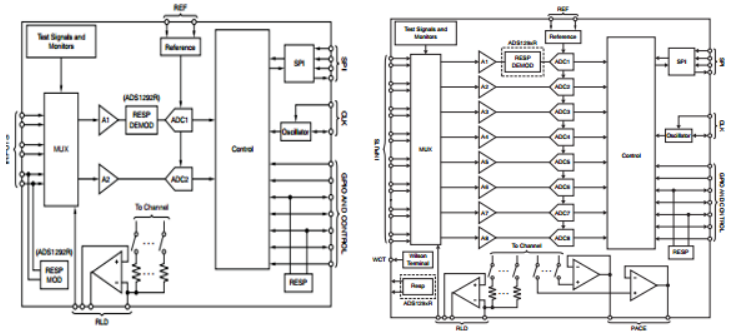

Figure 3.16: Functional block diagrams of (left) the ADS1292 2-channel ADC (right) the ADS1298 8-channel ADC.

Table 3.4: Electrode placement of the EMG subsystem

| Muscle | Primary Gross Motion | Secondary Gross Motion | Location in 3.17 |
|---|---|---|---|
| *Biceps brachii* | Elbow flexion | Forearm supination | a. |
| *Triceps brachii* | Elbow extension | – | b. |
| *Pronator teres* | Forearm pronation | Elbow flexion | c. |
| *Flexor carpi ulnaris* | Wrist Flexion | Ulnar deviation | d. |
| *Extensor carpi ulnaris* | Ulnar deviation | Wrist extension | e. |

#### 3.4.0.4 Electrode placement

In order to record electromyography signals indicative of the four DOFs within the sleeve's scope, the EMG modules are placed on accessible surface muscles, indicative of a particular gross motion, as informed by Tables 2.1, 2.2, and 2.3 in 3. The six selected muscles and the subsequent placement of their associated electrodes is described in Figure 3.4.

Figure 3.17 illustrates the location of the EMG electrodes as described in the fourth column of the table above. Without proper, deliberate sensor placement, little of the desired signal content will be picked up through the acquisition model and either cross talk or common noise will dominate the response. As well, the figure below indicates the location of the active reference electrode, used to further reduce common mode noise within the system. This is placed on the body structure of the elbow.

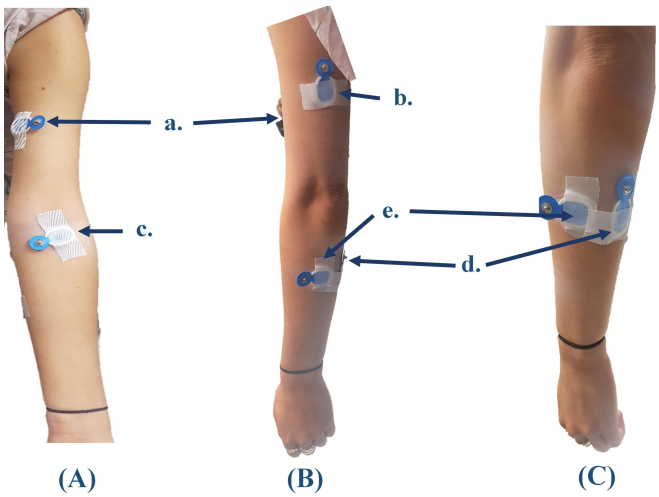


Figure 3.17: Placement of electrodes for use within the biosignal acquisition sleeve. (A) View of electrodes placed on the anterior side of the upper limb in the coronal plane. (B) View of electrodes placed on the posterior side of the upper limb in the sagittal plane. (C) View of electrodes placed around the posterior of the elbow in the coronal plane.

### 3.4.1 EMG partial prototype setup 1 — MyoWare modules

Two separate EMG single modality subsystems were tested. For the sake of simplicity, the subsystems focused on the flexion–extension motion of the elbow. In both cases, gelled electrodes were used to validate the change in muscle activity during the motion from the *biceps brachii* and *triceps brachii* muscles.

The first setup used the MyoWare modules to collect raw EMG signal data from one bipolar electrode site, the *biceps brachii*. A gelled electrode was placed at the terminals of the two female snap locations on the sensor, as well as on the driven right leg attachment cable on the module. Looking at the internal schematic of the sensor, the raw data signal comes from the output of a Texas Instruments INA106 difference amplifier. This has a common mode rejection of 86 dB and a fairly low input impedance of 110 kΩ , making it unsuitable for passive capacitive electrodes. The MyoWare module's signal was collected using a simple analog read function on the Arduino Teensy 3.5. It was powered using 3.3 V from the microcontroller's regulator.

The subject was asked to preform three repetitions of elbow flexion–extension motion. The digitized signals were displayed in the serial monitor and copied into a .csv file; consequently, the data were input into MathWork's MATLAB. Here, it underwent filtration and amplification. The resultant data were plotted such that visual detection could be used to determine if the data

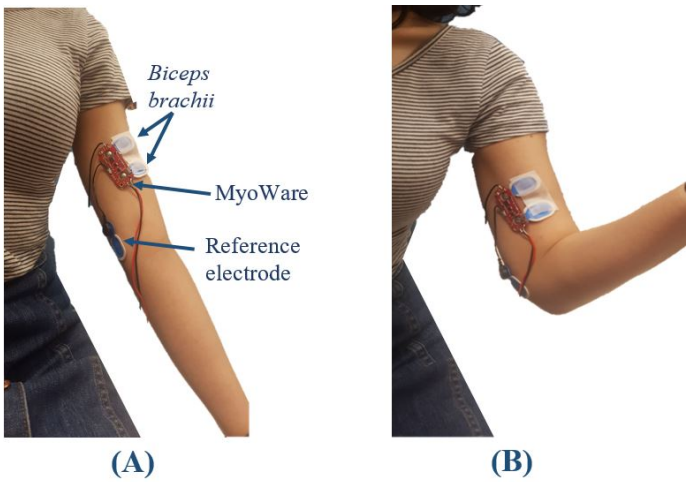


Figure 3.18: Placement of the MyoWare EMG acquisiton modules on the *biceps brachii* and *triceps brachii* for sensor validation.

collected by the subsystem were characteristic of the anticipated signal. A sample of these data can be seen in Figure 3.19 below:

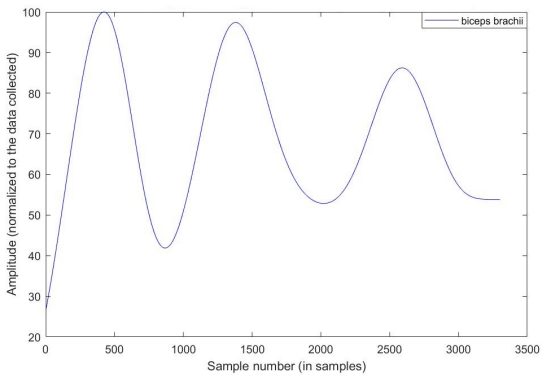


Figure 3.19: Plots displaying the muscle activity of the *biceps brachii*, in blue, and the *tricps brachii*, in red, during three repetitions of elbow flexion–extension with respect to sample number. The data have been rectified, filtered, amplified, and normalized with respect to the maxmimum value observed in the signal stream.

Figure 3.19 displays a plot of the sensor's voltage representation of muscle activity with respect to time, expressed in terms of the sample number. The sensor collects data at a sampling rate of 500 Hz, which is the expected frequency of EMG signals. Through visual detection, one can observe three bursts in muscle activity on both data channels, which are indicative of the three elbow flexion–extension repetitions preformed by the subject. This can be seen as a simple validation of

the sensor.

### 3.4.2 EMG partial prototype setup 2 — ADS1292R

Another possible set-up for collection of EMG data from muscle sites is through the use of the selected analog-to-digital converter. Here, an ADS1292R ECG/Respiration Breakout Kit was purchased from ProtoCentral Inc. to be used within this protocol. This board contains the ADC, regulated analog and digital power supplies, inputs for two electrode channels and a driven right leg reference. The inputs are interfaced to the board via a jacks with three strands of sheilded cable, each terminated by a female snap receiver. Like the previous subsystem setup, gelled electrodes were snapped into the terminals of the snap receivers; however, monopolar signals were collected at the *biceps brachii* and *triceps brachii* sites. A driven right leg electrode was attched to the bony structure of the elbow to provide a reference signal. The setup of this trial is shown below in Figure 3.20.

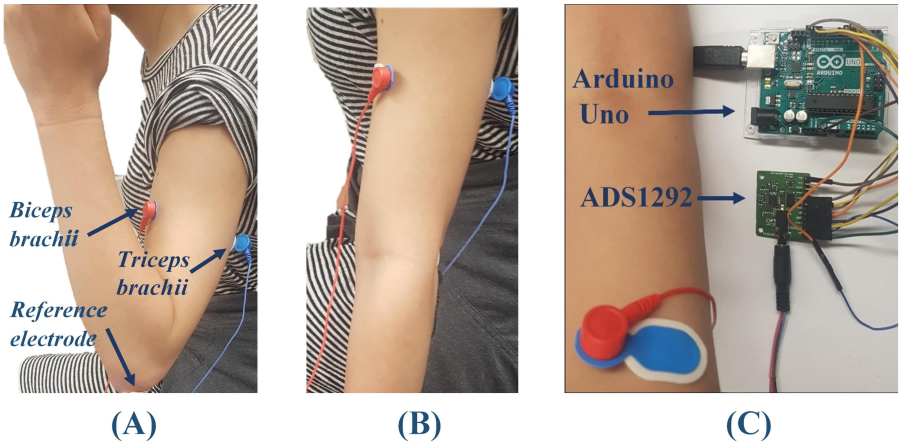


Figure 3.20: Placement of the gelled electrodes on the *biceps brachii* and *triceps brachii*, connected to the ADS1292 for EMG sensing validation.

The ADS1292R breakout board was wired to an Arduino Uno microcontroller and a test program was used to acquire digitized voltage representation of muscular activities from the three sites. The Uno was used due to the breakout board's required 5 V input that can be drawn from this microcontroller itself. The ability to communicate with the module through the SPI protocol was verified and the functionality of some of the ADC's features was tested.

Following this verification, the subject was asked to preform three repetitions of elbow flexion–

extension motion. The digitized signals were displayed in the serial monitor and copied into a .csv file, input into MATLAB, and processed in the same manner as the raw signals obtained using the MyoWare sensors in the first subsystem protocol. These data were plotted as the normalized representative voltage with respect to the sample number, as seen in Figure 3.21.

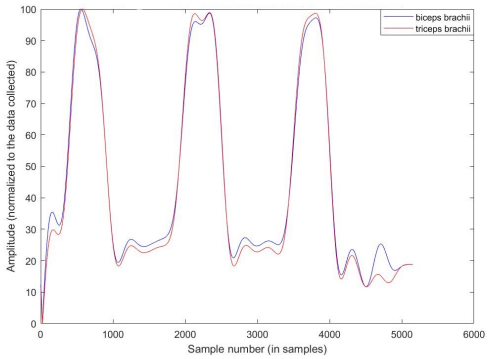


Figure 3.21: Plots displaying the muscle activity of the *biceps brachii*, in blue, and the *tricps brachii*, in red, during three repetitions of elbow flexion–extension with respect to sample number. The data are collected from the 24-bit ADS1292R breakout boards and have been rectified, filtered, amplified, and normalized.

Like the MyoWare setup, the data acquired through the ADC exhibited three bursts of muscle activity, coinciding with the three motion repetitions. Specifically, the *biceps brachii* is activated first through the flexion portion of the motion, followed by the *triceps brachii* during extension. The observed signal matches the expected activation pattern.

## 3.5 Integrated Sleeve Design

### 3.5.1 Revised design considerations

Following the attempts at construction and testing of the two single-modality systems, the design specifications of the integrated sleeve could be further defined. The microprocessor was selected through analysis of the sensor program requirements and consideration of other peripherals. Data transfer, communication, and the power circuitry have been designed around the aforementioned constraints in order to limit the electronics, aside from the sensors, to a series of PCBs.

### 3.5.2 Microcontroller selection

The microcontroller selected for the integrated design is part of Microchip's PIC32 family. This chip is capable of supporting the peripheral sensors and communication devices included in the design, and is compatible with all of the components. It contains three SPI communication channels, so it can support the two different sensing modalities and the device's external communication measures simultaneously; as well, there is an $I^2C$ channel for a battery management IC, such that the system's power can be transferred and monitored. The MCU's 32-bit processor ensures that there is no aliasing of recorded data; particularly, the 32-bit channel ensures that the EMG signals quantized by the ADS1298 maintain their level of precision for effective processing results later on. The MCU is able to run off of a 3.3 V supply rail, which is compatible with the chosen sensors. This reduces the amount of boost/buck conversion circuitry required for the system and decreases the likelihood of logic level shifting errors in the system design.

### 3.5.3 Board designs of major components

The main electronic components of the signal acquisition sleeve PCB were broken down into the following three modules:

1. **Microcontroller board**: this board contains the PIC32MZ series microcontroller and its supporting circuitry. It has buttons for both the manual reset of the board and the power. As well, this module acts as a central hub for the electronics system of the sleeve and contains a housing to interface with connectors that allow the other modules, as well as sensors, to be attached to the system and routing for all three power supplies. The schematics and board design are presented in Figures 3.22 and 3.23.

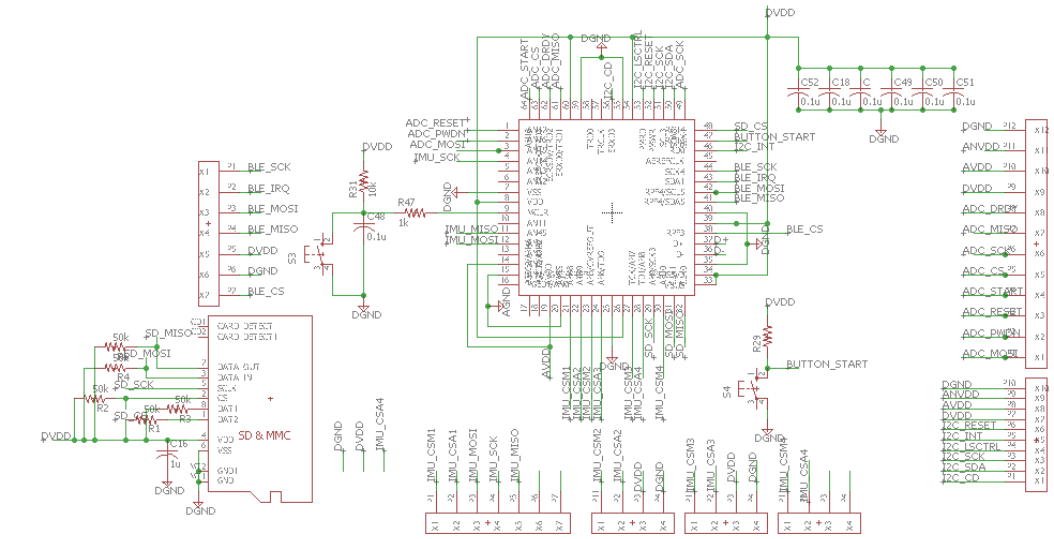


Figure 3.22: Schematic of the integrated sleeve's microcontroller module PCB.

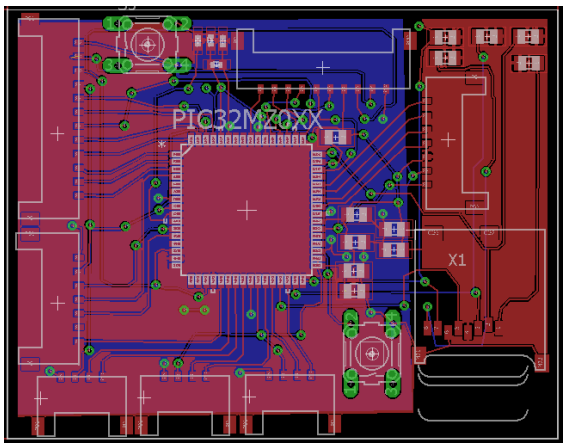


Figure 3.23: Board layout of the integrated sleeve's microcontroller module PCB.

2. **ADC board:** this board contains the eight channel ADS1298 analog-to-digital converter. It has board housing to connect to the electrode module inputs, RFID protection for these signals, and driven right leg circuitry to collect the common-mode signal from an external source. The schematic, board design, and a photo of the fabricated board are presented in Figures 3.24 and 3.25.

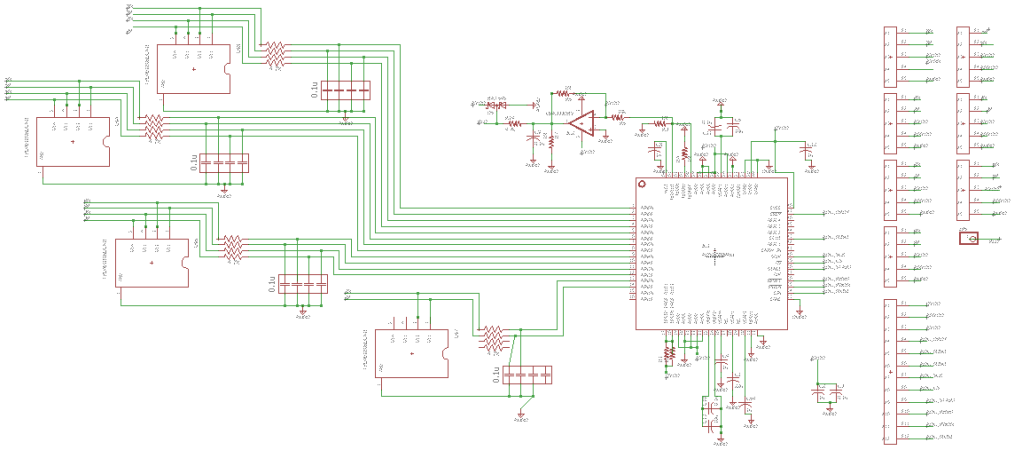

Figure 3.24: Schematic of the integrated sleeve's microcontroller module PCB.

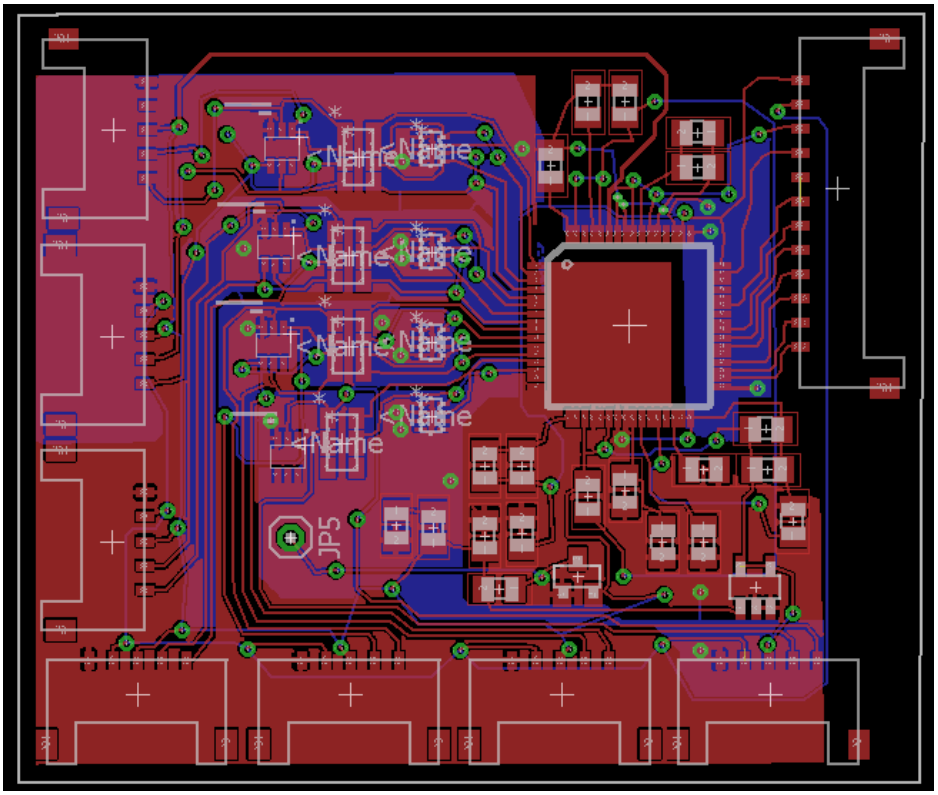


Figure 3.25: Board layout of the integrated sleeve's ADC module PCB.

3. **Power management:** This module is used to establish the three necessary power supplies for the other modules and sensors used within the system. The design and fabrication of this

module faced many iterations and challenges, which are further described in Section 3.5.3.1.

#### 3.5.3.1 Power considerations

As the integrated sleeve is intended to be an untethered biomonitoring device, the electronic components must be able to remain powered without a wired connection for the duration of a typical at-home physical therapy regimen. This implies that it must be battery powered. A 400 mAh lithium-ion rechargeable coin cell battery from Illinois Capacitors' RJD line was used to provide power to the system. This chemical structure has been proven to be stable and safe for consumer use; however, some power protection circuitry is required. Li-ion batteries have a high energy density and are typically lightweight and durable. The coin-cell packaging of this particular battery further reduces the footprint, such that the mass, size, and comfort of the device is not compromised for functionality. This battery is considered to be memoryless, such that capacitance is not sacrificed when charging the battery before it is fully discharged.

In the design, Texas Instruments' BQ29702 chip was used to safeguard both the battery cell and the wearer from high discharge currents and overcharge conditions using external FET monitoring and trigger thresholds. This IC, and the remainder of the power circuitry, is displayed in Figure 3.27.

The power management system was then re-designed and greatly simplified from the initial design shown in Appendix 1. The level of complexity and features within the ball grid array chip were deemed unnecessary. Instead, MAXIM Integrated Products' MAX1555 Dual-Input USB/AC adapter 1-Cell Li+ battery charger was used. This chip uses a SOT23 package with only five pins, making implementation significantly easier and does not require the $I^2C$ communication protocol. Like the previous design, it receives power from the microUSB module without additional protection. The battery output pin connects to the battery via Texas Instruments' BQ29702 chip for protection before branching off to two separate regulators.

One branch leads to the establishment of a separate +/- 5 V analog power source for both the mixed-signal ADC and the electrode modules. A dual supply is output from this LDO, as many EMG analog front end circuit modules use differential amplification and require the use of both a positive and negative supply rail. Here, Texas Instrument's TPS7379 is incorporated to provide the desired output. The other regulator establishes a 3.3 V digital power supply. The board includes housing for the connector cables that attach to the MCU module, providing power

to the rest of the system. The board schematic and layout are presented in Figures 3.26 and 3.27.

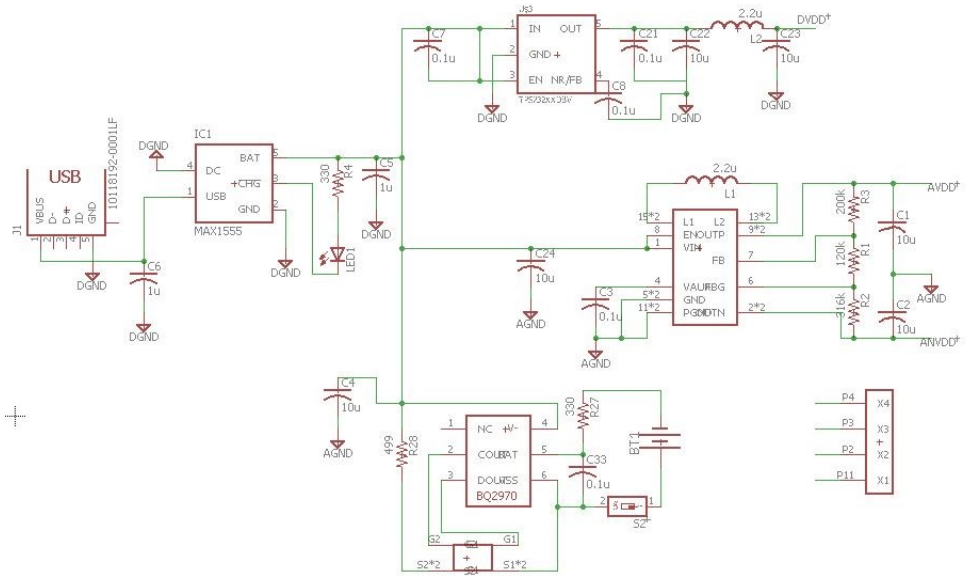


Figure 3.26: Schematic diagram of final iteration of power management circuitry.

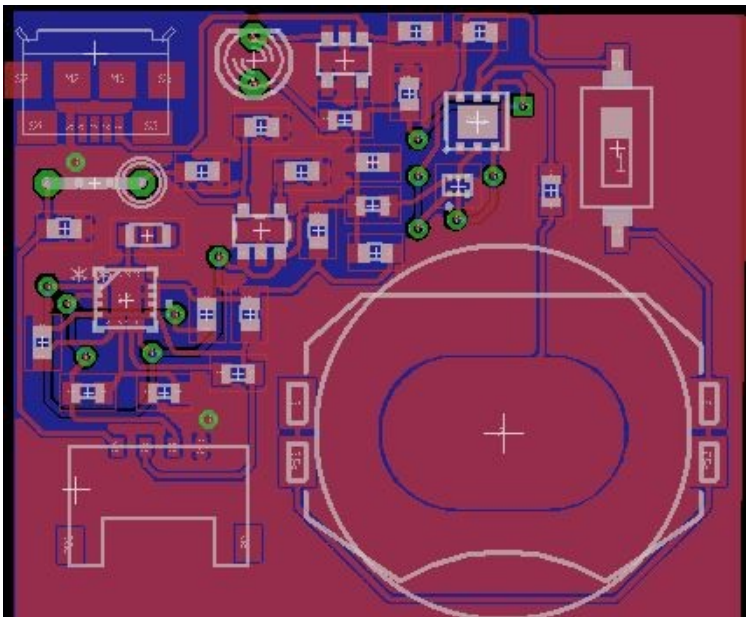

Figure 3.27: Board layout of the final iteration of power management circuitry.

## 3.6 First Sleeve Prototype

A preliminary prototype of the biosignal acquisition sleeve was constructed utilizing the selected sensing modalities and the sensor locations described earlier in this chapter; however, the microcontroller and major board designs presented in Section 3.5 were not used due to limitations of resources, time, and technical skills needed to implement and troubleshoot the module designs.

Still, the prototype fulfills the major criteria of the sleeve described in Section 3.2:

- The sensors remained modular,
- The system did not impede upon movement related to major gross motions,
- Both biomechanical and physiological sensing modalities were incorporated,
- The prototype was simple to use.

The developed prototype, including the physical sleeve and its electronic components, are shown off-arm in Figure 3.28 and on-arm in Figure 3.29.

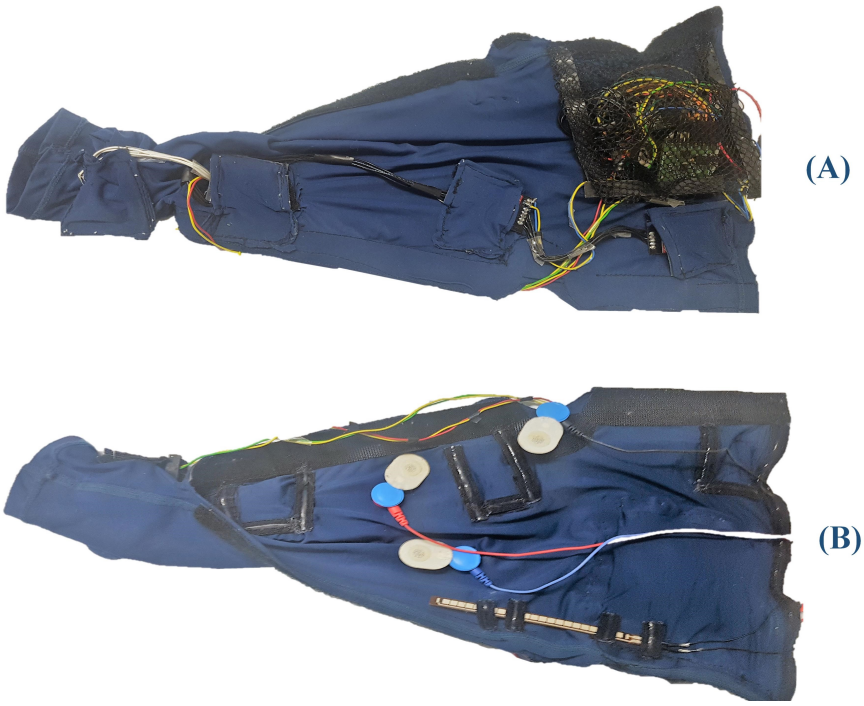


Figure 3.28: First prototype of the biosignal acquisition sleeve. (A) View of the exterior of the sleeve laid flat, with the microcontroller and ADC inside the mesh pocket and the IMUs in their pockets. (B) View of the interior of the sleeve laid flat, with the elbow flex sensor and electrodes laid over possible placement sites.


Figure 3.29: First prototype of the biosignal acquisition sleeve, shown on the arm of a user. (A) View of the exterior of the sleeve, along the coronal plane of the arm. (B) View of the exterior of the sleeve on-arm, along the sagittal plane. The sleeve is partially un-velcroed to reveal the EMG acquisition electrodes.

The remainder of this section describes the changes made from the intended design to the current prototype, the mechanisms for modularity, the physical design of the sleeve, and a quick "common-sense" test where the prototype is used to obtain data from the four major gross motions of the upper limb.

### 3.6.1 Microcontroller and power

While the initial integrated design uses individual board designs for the microcontroller/peripheral hub and the system's power management, the first version simplified and combined these boards for rapid prototyping as shown in Figure 3.30. The Arduino Teensy 3.5 was used in place of the Microchip MZ series microcontroller. The Arduino uses a simple integrated development environment (IDE) for quick programming, and is sold on a breakout board that contains a built-in SD card slot and an internal 3.3 V regulator. This reduces the components required in the remainder of the design.

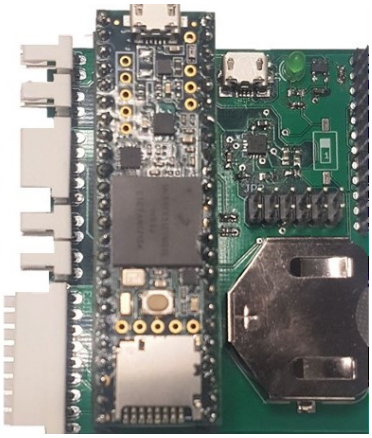

Figure 3.30: Microntroller and power board for the biosignal acquisition sleeve prototype.

The use of the Teensy 3.5 does not compromise the performance of the system. In addition to the built-in line for the SD card, there are three SPI buses available. This is sufficient to accommodate the chosen peripheral devices. The processor is capable of storing the data acquisition program and operates at a rate quick enough to collect data from the sleeve's sensors at their appropriate acquisition rates.

The board also contained a rechargeable 3.7 V lithium ion battery was used to provide power to the microcontroller and its peripherals while untethered from a PC. The battery was charged using the MAX1555 IC, which received 5 V from a microUSB when connected to a PC. The MAX1555 output was then attached to the Texas Instruments' TPS65135 split rail voltage converter, which provided a $\pm$ 5 V voltage rail. The positive voltage was used as a voltage source to power the microcontroller.

A schematic of the printed circuit board can be seen below in Figure 3.31 below, and the board layout is shown in Figure 3.32.

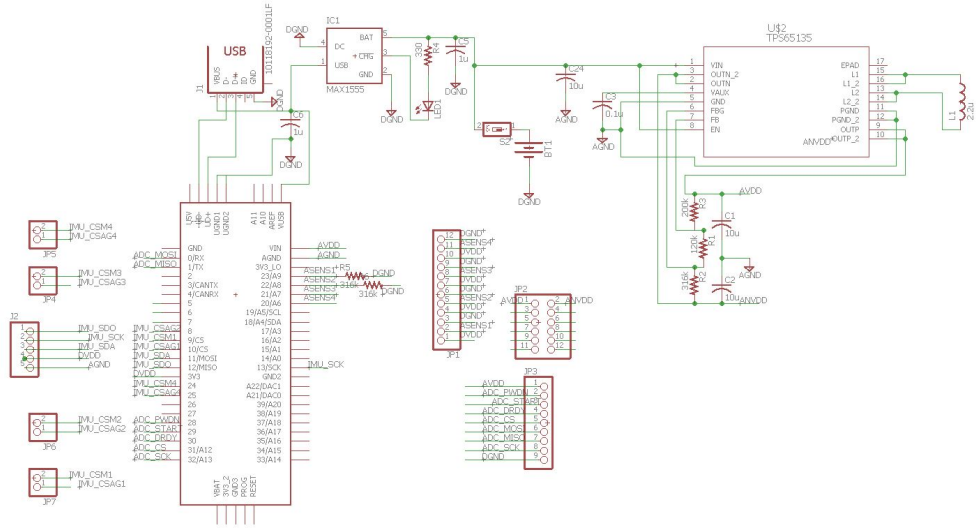


Figure 3.31: Schematic of the microcontroller and power circuitry for the biosignal acquisition sleeve prototype.

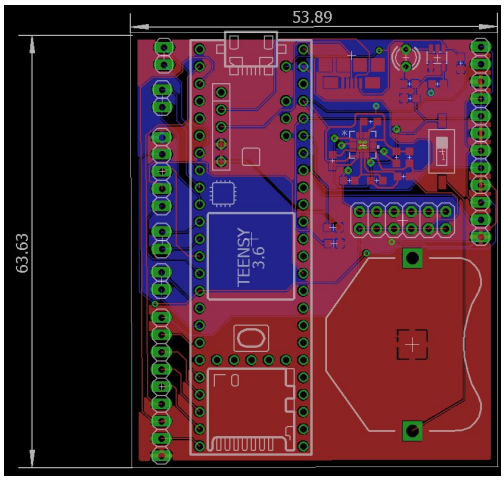


Figure 3.32: EAGLE board layout for the microcontroller and power circuitry for the biosignal acquisition sleeve prototype.

### 3.6.2 Physical sleeve design

The sleeve's physical structure has been chosen to best meet the design criteria and effectively house the electronic components. It was based on the modification of an existing compression sleeve, the "Elixir Scorpion UV Sun Protective Compression Sleeve" purchased via Amazon.ca. This sleeve extends from the base of the palm, wrapping around the thumb, to the upper arm,

just distal of the elbow. It is comprised of a blend of nylon (85 %) and spandex (15 % ), which is fabricated to wick moisture and maintain a comfortable temperature. The sleeve itself is shown in Figure 3.33.


Figure 3.33: Physical structure of the biosignal acquisition sleeve. (A) Sleeve not on user, laid flat with velcro and elastic exposed (B) Sleeve not on user, view of external sensor pockets.

While the base purchased was a "one size fits all" product, it was found to run on the larger side. In order to make the fit adjustable the sleeve was cut along the humerus and ulna in the coronal plane, stopping at the wrist. This cut was curved around the elbow. Thick Velcro strips were sewn onto the sleeve on both sides, allowing the user to attach the two edges at a comfortable point. The Velcro was placed in this location because it would not interfere with the anticipated sensor sites.

The compression sleeve's fit was intended to reduce muscle vibration, minimizing fatigue and soreness; additionally, the structure ensured that the sensors were held firmly in place. Non-stick elastic was sewn on the perimeter of the sensor sites, on the side of the sleeve in contact with the user's skin. This mechanically stabilized the skin, limited uncoupled motion and reduced motion artefacts. Similarly, this elastic was attached around the extremities of the sleeve and near the uncovered portion of the elbow, where the common reference electrode was placed.

The microcontroller, power sources, and inertial measurement units were placed along the exterior of the sleeve. In order to conceal their appearance and secure them in place, pockets were created using the same base material. These pockets were partially sewn onto the modified

sleeve along two adjacent sides and attached to the other two via Velcro. This allowed for the components to easily be removed in the following situations: the component was not in use, the component was swapped for another sensor, or the sleeve needed to be reprocessed.

The IMU pocket sites were informed by the partial prototype set-up described earlier in this chapter, in Section 3.3.2. The sensors themselves were attached to small PCBs, shown below in Figure 3.35. The use of the board-to-wire connection system allowed for the detachment of sensors to maintain modularity, without sacrificing ease of use due to the organization of the wires. The board-to-wire connectors create a signal chain between the microcontroller and each of the sensors, which can be seen in Figure 3.34.

Figure 3.34: Biosignal acquisition sleeve prototype with a signal chain between the microntroller and IMUs using detachable board-to-wire connectors.

The five-signal connectors passed through the power, ground, serial data in, serial data out, and clock pins; specifically, one connector was used to receive the signal from the previous sensor in the chain, and the other connector was used to pass these signals to the next module. The boards' use enabled the creation of these shared signal nodes. The final two-signal connector attached the two chip select pins of the sensor to the microcontroller.

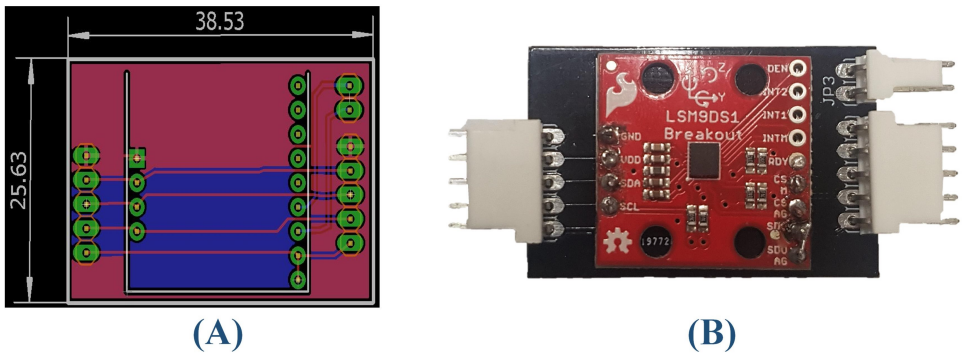


Figure 3.35: PCBs containing the LSM9DS1 IMUs and SPI connection nodes. (A) Board layout in EAGLE 7.6.0 (B) View of the assembled PCB with connectors.

Two piezoresistive sensors were incorporated within the sleeve design to provide an additional representation of the wearer's bending motion. Both sensors were placed on the interior layer of the sleeve, in the anatomical coronal plane. One was placed across the interior of the elbow joint (medial epicondyle) from just proximal of the elbow to just distal of the elbow. The other sensor was place across the wrist on the lateral side of the arm. The leads on these sensors were soldered to thin-gauged wire and attached to the MCU board with standard header pins. Each of these sensors were fastened to the sleeve through the use of four loops of non-stick elastic, as shown in Figure 3.36. This allows for the sensor to be easily added or removed from the structure, to secure the base of the sensor, and to prevent the sensor from being bent in a manner that will damage it. The piezoresistive sensors were calibrated prior to being incorporated within the sleeve, as the sensor acts as a variable voltage divider, the output resistance was recorded while the sensor was flat, at zero degrees, and at a right angle, 90 degrees. These values were then used to proportionately map out resistance values that fall within that range.

Figure 3.36: Piezoresistive sensor secured to the interior of the biosignal accquisition sleeve.

The electrodes and EMG acquisition modules were placed on the interior of the sleeve prototype. This allowed for the electrode sites to be selected based upon the user's anatomy, as there were no fixed locations on the sleeve. The interior sensor sites also allows for the type of electrode to be easily swapped out, as both the MyoWare modules and the ADS1292 used snaps as electrical connectors that were able to facilitate gelled electrodes or custom insulated electrodes. The compression sleeve base holds the electrodes in place, decreasing movement and motion artefacts in the signal. A wire routing pathway was created on the interior of the sleeve alongside the velcro to streamline the sleeve's profile for improved organization, comfort, and appearance. The interior of the sleeve with electrodes and EMG acquisition modules can be seen below in Figure 3.37, showing the sensors placed on a user's arm before the sleeve is fastened. Silicon-based elastic was also sewn around the perimeters of the underside of the pockets that house the IMUs in order to provide mechanical stability to the sensors while the arm was in motion.

Figure 3.37: Biosignal acquisition sleeve prototype shown off-arm and open, providing a view of a possible electrode placement.

#### 3.6.2.1 Reprocessing considerations

In order to be a fully realized device, the designed biosignal acquisition sleeve must be able to be reprocessed, such that it can be sterilized, cleaned, and made safe for repeated use. This procedure must be accessible to those using the device remotely, outside of a lab or healthcare environment; consequently, no specialized tools or equipment should be required. Simple cleaning is made possible due to the modular nature of the device, such that sensitive components can be detached and sterilized separately.

The physical structure of the sleeve allows the user to take the device apart and wash the components individually. The nylon–spandex material allows for the sleeve's base to be washed using simple detergent either by machine or by hand. The velcro, mesh, and elastic materials used in the shell are also washable using conventional measures. The electronic components can be removed from their respective pockets, fasteners, or sites prior to washing.

Although the sensors themselves do not come into contact with neither the human body nor the environment while the sleeve is in use, they can be cleaned separately. Basic alcohol wipes can be used to disinfect the sensors and their respective breakout boards without damaging the circuitry.

### 3.6.3 Data acquisition, evaluation, and display

The prototype was evaluated through the collection and visual verification of data from the four basic gross motions described in the initial design considerations in Section 3.2. The prototype of the biosignal acquisition sleeve was donned by a healthy user and data were collected from the following sensors for each motion type:

- Four IMUS, placed proximal and distal to both the elbow and wrist,
- One piezoresitive flex-bend sensor, along the elbow or wrist,
- EMG signals from two electrode sites, dependent on the motion preformed.

Four repetitions of each gross motion were performed per each gross motion trial.The data were collected through a Arduino Teensy 3.5 microcontroller, which was programmed to detect the type and number of sensors connected to the microcontroller. It was able to determine: the number of LSM9DS1 IMUs used, between zero and four; the presence of the ADS1292R breakout board; the number of flex sensors attached, between zero and two; and the number of other analog sensors, such as the MyoWare modules, used, between zero and four. The script created a data header based on the detected sensors and saved the sensor information as a comma delimited list to an SD card.

A set of sample plots for each gross motion are displayed for elbow flexion–extension in Figure 3.38, forearm pronation–supination in Figure 3.39, wrist flexion–extension in Figure 3.40, and ulnar–radial deviation in Figure 3.41.

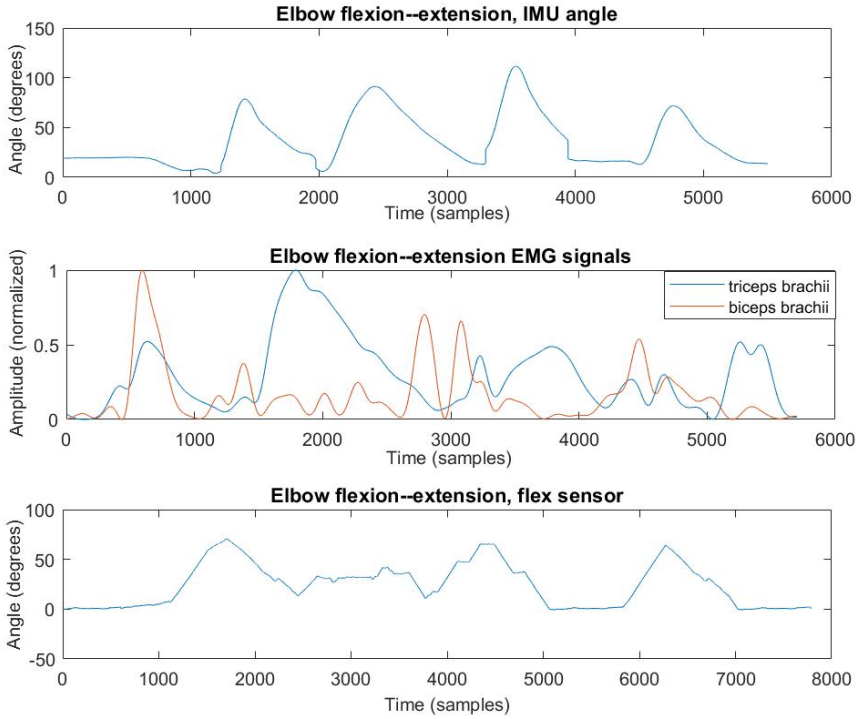


Figure 3.38: Sample data from the biosignal acquisition sleeve for four repetitions of elbow flexion–extension motion. The top plot contains the angular orientation of the elbow from the IMU subsystem, determined using the corresponding ISB JCS. The middle plot contains representative muscle signal information from the *biceps brachii* and *triceps brachii* muscles. The bottom plot contains the elbow angle, collected from the flex–bend sensor.

In addition to the sample data plots in Figures 3.38, 3.39, 3.40, and 3.41, data were displayed using an application developed using MathWorks' MATLAB R2017B. The application's toolbar allows the user to select the datastream from the SD card they wish to input. Upon loading, the diagram panel indicates which sensors are present through the change in colour of the buttons on the sensor sites from gray to: a muted red, for EMG electrodes; to a muted blue, for IMU sites; or to a muted green, for other analog sensors. Clicking on these buttons will select the data streams the user would like to view. These are plotted in the tab "RAW" on the right-hand panel of the page. Additional common processing options are available and can be selected under from the "PROCESS" menu on the tool bar. The EMG data can be normalized, filtered in accordance to standard practices, observed in the frequency domain, or placed through the Teager-Kaiser energy operator. The number of repetitions detected for certain motions can also be tested using the algorithm later described in Chapter 4. The IMU data can be placed through the Madgwick

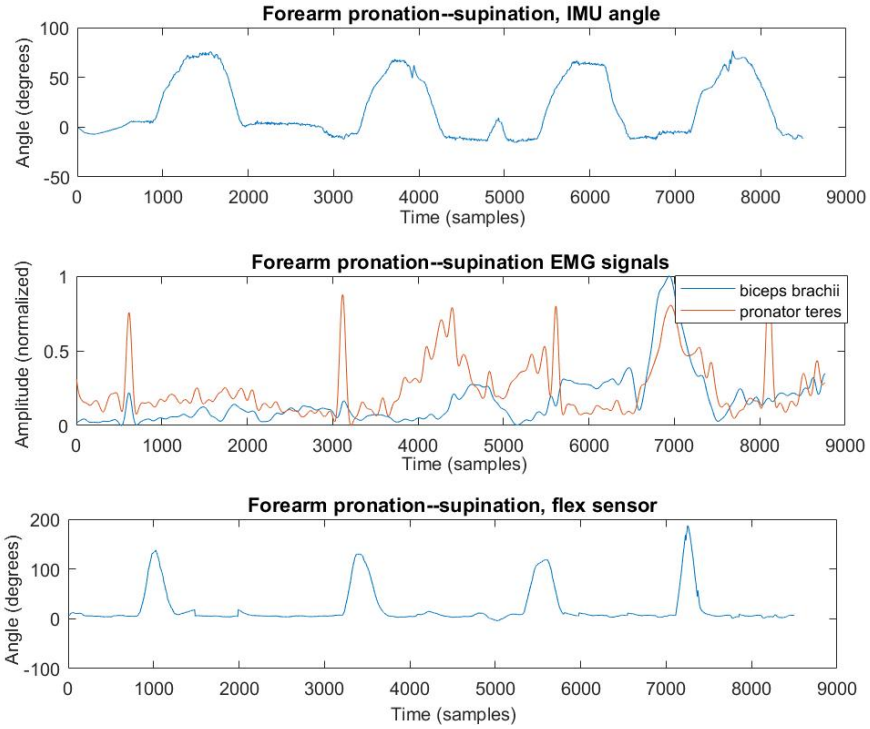


Figure 3.39: Sample data from the biosignal acquisition sleeve for four repetitions of forearm pronation–supination motion. The top plot contains the angular orientation of the forearm from the IMU subsystem, determined using the ISB radioulnar JCS. The middle plot contains representative muscle signal information from the *biceps brachii* and *pronator teres* muscles. The bottom plot contains the elbow angle, collected from the flex–bend sensor.

orientation filter and expressed as quaternions, Euler angles, or Cardan angles in accordance with the ISB JCS. Figure 3.42 displays the appearance of the interface prior to loading in the desired data. Figure 3.43 shows the appearance of the interface once wrist flexion–extension data were loaded in to the application; here, IMU4 is selected from the image in the left panel and thus displaying this sensor's raw accelerometer, gyroscope, and magnetometer data in the visible tab within the right panel. Finally, 3.44 shows the application's appearance after the user had chosen to filter the available EMG data from the *flexor carpi ulnaris* and the *extensor carpi ulnaris*.

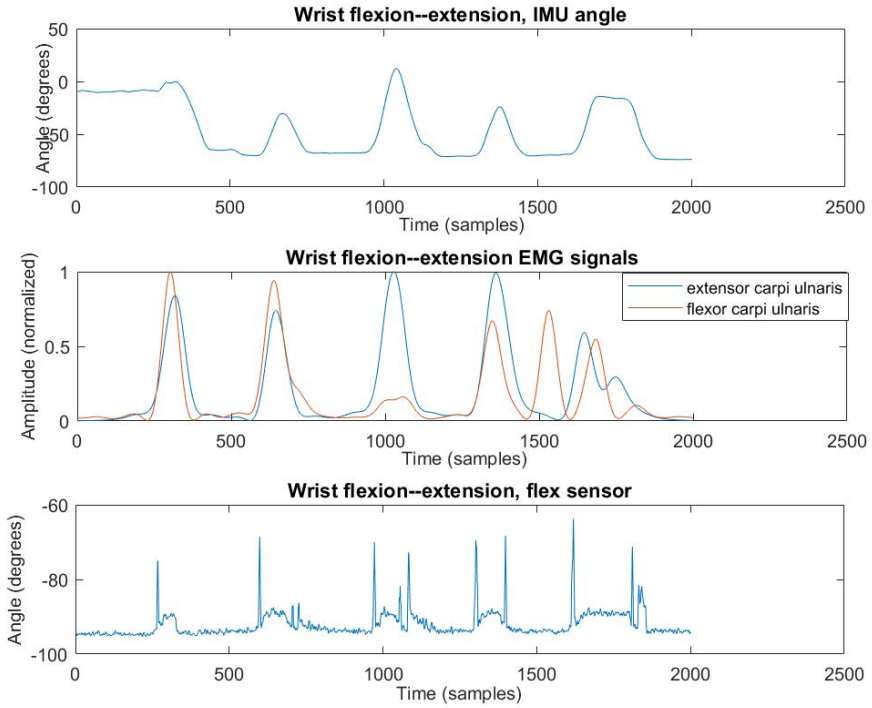


Figure 3.40: Sample data from the biosignal acquisition sleeve for four repetitions of wrist flexion–extension motion. The top plot shows angular orientation of the wrist from the IMU subsystem, determined using the ISB JCS representation of the wrist. The middle plot contains EMG data from the *extensor carpi ulnaris* and *flexor carpi ulnaris* muscle. The bottom plot contains the wrist angle, collected from the flex–bend sensor.

## 3.7 Conclusions

The current first prototype of the biosignal acquisition sleeve accomplishes the goals set out by the initial design considerations outlined in Section 3.2. The sleeve met all of the described functional requirements, and was able to effectively track human elbow flexion–extension, forearm pronation–supination, wrist flexion–extension, and radial–ulnar deviation; furthermore, both biomechanical and physiological sensing methods were used to create these motion profiles. The information collected using the biosignal acquisition sleeve fell within the expected ROM within existing models: specifically, the EMG data could be processed using typical filters and the IMU data could provide angular orientation within the expected anatomical ranges of motion using the Madgwick filter and joint coordinate systems defined by the International Society of Biomechanics. As well, the IMU data's efficacy was further validated through a comparison to data obtained concurrently from a commercial tracking system.

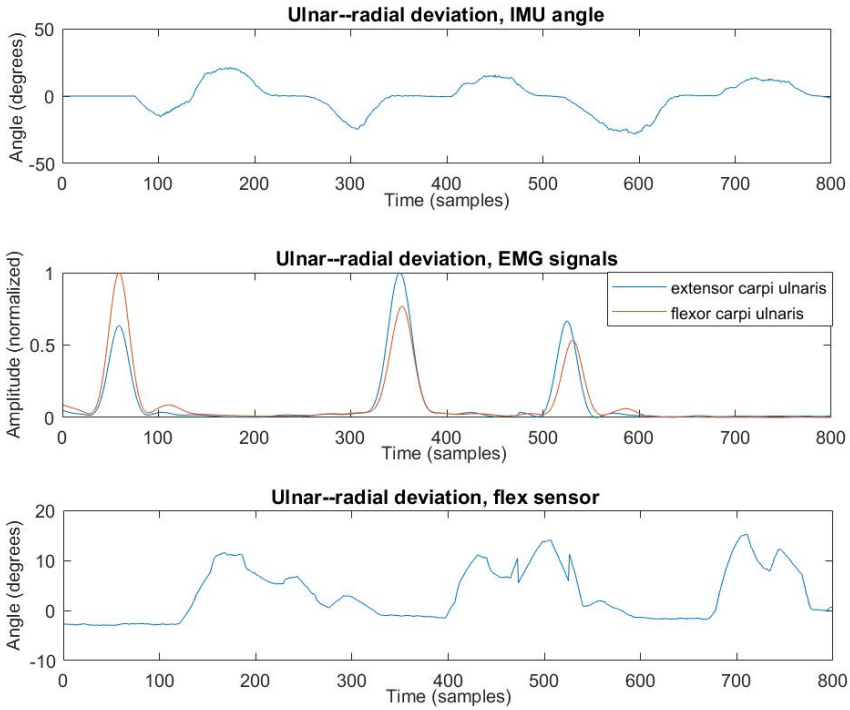


Figure 3.41: Sample data from the biosignal acquisition sleeve for three repetitions of ulnar–radial deviation motion. The top plot shows the angular orientation of the wrist from the IMU subsystem. The middle plot shows EMG data from the *extensor carpi ulnaris* and *flexor carpi ulnaris* muscle. The bottom plot contains the wrist angle, collected from the flex–bend sensor.

While the initial electronics design was not implemented, the prototype allowed for the sensor choice to remain modular. The chaining of IMUs let the user select the number and location of positional sensing; meanwhile, multiple EMG acquisition modalities, the Advancer Technologies MyoWare modules and the ProtoCentral ADS1292R module, were tested to demonstrate the compatibility of different sensor types with the system. The microcontroller's software was designed to recognize the type and number of sensors connected to the system, and adapted the document header and collection sequence correspondingly. The prototype also remained fully self-contained and ambulatory, as this version contained an on-board rechargeable battery, power regulation, and an SD card to record the collected data.

The physical design of the sleeve allowed it to fulfill many of the qualitative aims outlined in Section 3.2. The sleeve did not impede motion, as evidenced by the measurement of the full expected ROM, and could be worn for long periods of time. The design was velcro-adjustable to provide a proper fit for the user, and created from materials that allowed for comfort, proper reprocessing,

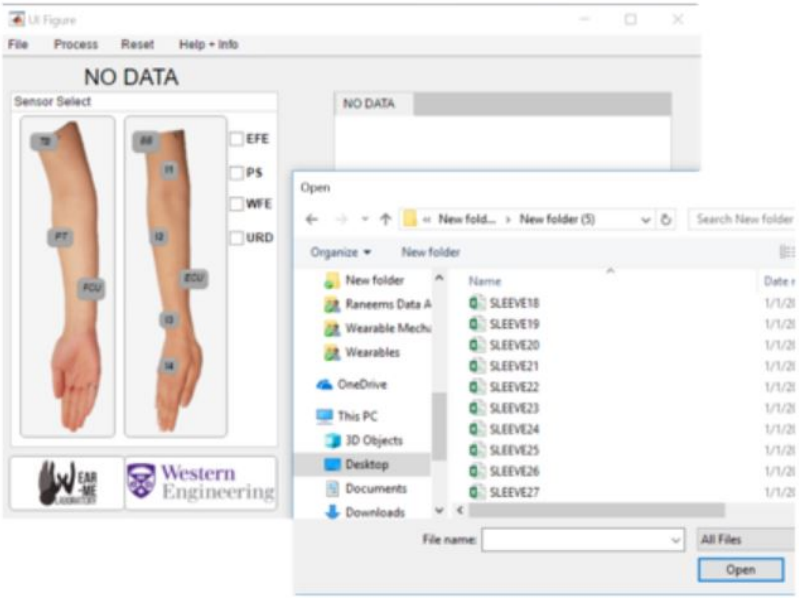


Figure 3.42: Screen-shot of the data visualization application before loading in session information.

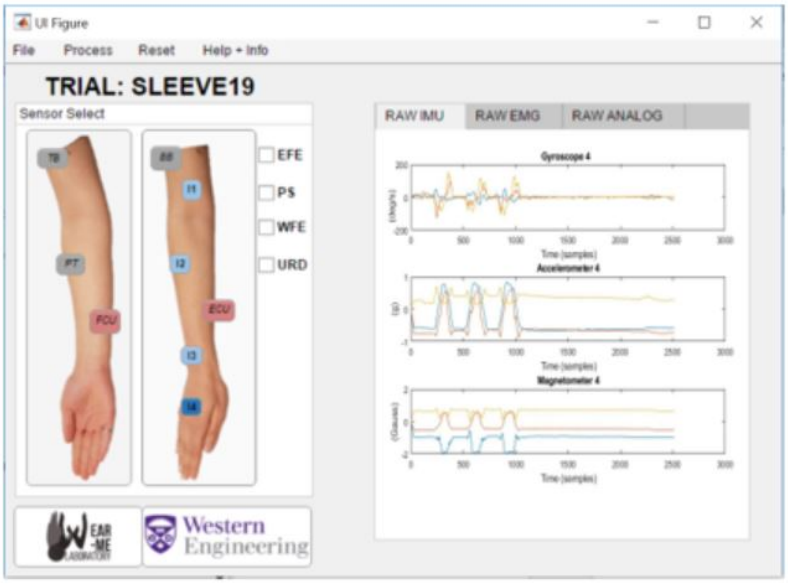


Figure 3.43: Screen-shot of the data visualization application after loading in a WFE session, showing raw IMU data.

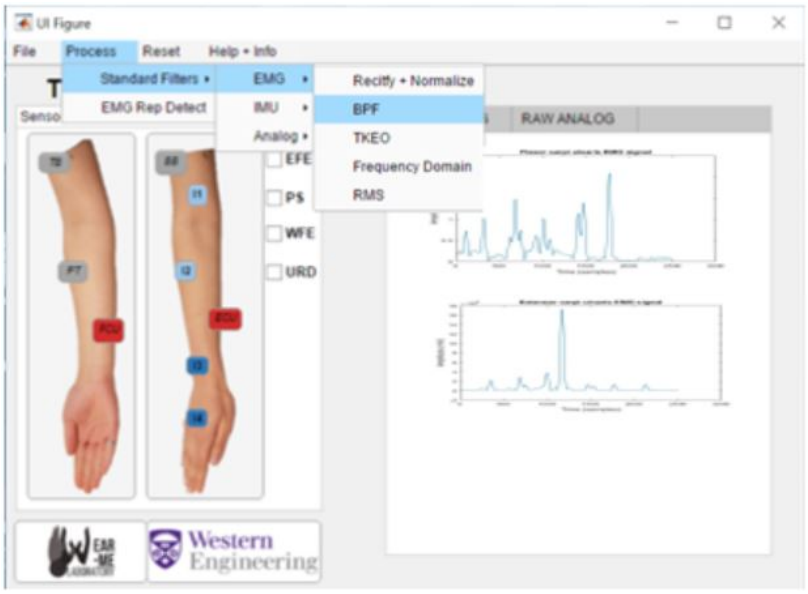


Figure 3.44: Screen-shot of the data visualization application after loading in a WFE session, showing processed EMG data.

and security of the electronics. While the prototype was not obtrusively bulky, the size of the some components would be reduced through the implementation of the more complex electronic design in Section 3.5.3. The combination of the adaptive collection software, plug-and-play sensor input, and MATLAB visualization application make the use of the system straightforward and simple to operate. Overall, this preliminary design of an ambulatory, modular, and multi-modal biosignal acquisition sleeve met its intended goals.

# Chapter 4

# Algorithm for Detecting Motion Repetitions Using EMG Signals

## 4.1 Introduction

This chapter discusses the development and testing of a MATLAB algorithm used to detect repetitions of gross-motions used in physical rehabilitation of upper limb MSDs. Repetition detection within an EMG signal stream is considered to be a challenge in EMG processing, as the inclusion of latent time can impede on proper feature analysis, and thus gesture classification. The algorithm was initially developed, tested, and validated using an existing EMG data-set collected by a previous student.

The same algorithm was modified to input and process data from the biosignal acquisition sleeve described in Chapter 3 to further test and compare its efficacy. As well, the algorithm was updated to include input from the IMU data collected. The proceeding work describes the principles used in alogrithm design, the data collection methods, the testing procedure, and the results obtained.

## 4.2 Repetition Detection

Detecting the onset of the EMG signal can be a considerable challenge due to the erratic nature of the signal stream; however, this is often necessary to characterize motion and extract features within it. Although filtering and pre-processing can help to eliminate some intrinsic noise and

motion artefacts, wandering baselines and poor signal-to-noise ratios can still present difficulties.

### 4.2.1 Existing methods

The problem of repetition detection has been looked at in literature through numerous different angles over the past 25 years. Still, there is not a singular method considered to be the "gold standard". There are three general approaches that each take on many form, as follows:

1. Visual-detection based analysis

   Visual detection-based analysis does not rely on the use of a computational algorithm; instead, this method of burst detection is done manually. Following post-processing, the stream is inspected using the human eye, and requires a person to pick out the onset and offset times. While computational inexpensive, it is time consuming for the individual to select the points for each data stream. As well, there is no quantitative criteria that defines the onset and offset times. With this method, there is no consistency amongst what constitutes a burst and its detection cannot be replicated; however, it gives immediate and visually justifiable results.

2. Threshold-based analysis

   The most commonly used methods of burst detection involve the use of thresholding. The single threshold method is the most simplistic and therefore computationally inexpensive; however, it is also the least accurate. Here, the onset is estimated once the amplitude exceeds a predefined value. Typically, this value is chosen to be the mean value of background noise in a filtered signal stream, without independently accounting for probability of false detections [98].

   This shortcoming is addressed in the double-thresholding methods by adding an additional degree of freedom to the design; here, the second threshold is considered to be a consecutive number of samples at which the amplitude exceeds the first threshold's value. Using this method, the signal is often whitened first to remove dependence on prior samples [94] [97]. A test function is calculated based on the product of the inverted squared variance and the sum of squares of the sample and its preceding sample; then, the first threshold is applied. Afterwards, a particular portion, $n$, of a set of successive samples,$m$, must exceed the threshold to remain active. The whitening and equal variance allow for explicit parameter

specification. Double threshold methods are more computationally expensive than the single threshold; however, they are significantly more accurate.

Both of these methods can be improved upon through the use of finite moving averages (FMAs). Here, a fixed-size sliding window can be used to find the weighted sum of signal amplitudes to redefine the baseline. This way, the muscle activity can be determined as the instant at which the signal exceeds the calculated baseline by a multiple of the standard deviation of baseline noise. This method was first proposed by Hodges and Bui [93], whose preprocessing involved low pass filtering and rectification. Liderith [96] later expanded upon their work by adding a decision rule that required the threshold to be exceeded by a specified number of following samples, $T_1$. As well, the signal was allowed to fall below the threshold within the burst for a specified duration. Abbink's [95] work uses the same pre-processing and algorithm as well, then applies a 30 Hz low pass filter. The onset and offset candidates are selected by looking at the maximum argument of the sum of the number of normalized amplitudes smaller than the threshold preceding the onset candidate and larger than the threshold following the candidate.

3. Statistically optimal decision-making

   This decision making method estimates the time of onsets through the use of statistical tools on existing information. While this group of methods may be very accurate, they are most difficult to implement and are computationally expensive. One method first reconstructs the desired data as a statistically independant Gaussian random process through the use of an adaptive whitening filter; from the resulting data, its chatacteristics are determined using the probability density function. The change in density and consequent variation in variance helps detect the onset and offset points. Then, decision making rules created based on previous knowledge of variance profiles before and after the changes in density are detected. For the optimal estimator, these variance profiles are known and the maximum likelihood estimate of the unknown onsets are computed using the log-likelihood function. The onset point is considered to be the maximum value of the argument of this ratio. Another method of statistically optimal decision making is the approximated generalized likelihood ratio, or AGLR, detectors [99]. Here, the variance profiles are unknown and the variables they are dependant upon are estimated using the AGLR, where a vector of potential parameters

are determined based on previous entries on a sliding-window basis; afterwards, a similar maximum likelihood ratio is used to estimate the onset point. This process has been used in two manners:

(a) **AGLRstep**, where the variance profile is assumed to be step-like in nature, where constant variances exist before and after the onset point.

(b) **AGLRramp**, where previous observations are used to determine the unknown parameters, which are assumed to form a ramp variance profile.

### 4.2.2 Teager-Kaiser energy operator

In conjunction with the existing repetition detection methods, the Teager-Kaiser energy operator (TKEO) can be applied as a pre-processing step to aid in onset detection. Like the moving average, the Teagar-Kaiser Energy Operator (TKEO) relies on the improvement of the signal's SNR in order to accurately detect bursts. Solnik applied this technique to EMG signals to compress the energies of the baseline noise to make the bursts more apparent [102] [101]. The operator is defined as:

$$\phi[x(n)] = x^2(n) - x(n+1)x(n-1) \tag{4.1}$$

where $x$ is the recorded amplitude and $n$ is the sample number across the signal stream. This is applied to the rectified, filtered, and smoothed data. Upon applying this operator, a threshold is detected from the new signal as follows:

$$T = \mu + J\sigma \tag{4.2}$$

Here, $\mu$ is the mean amplitude of the signal during latency, $\sigma$ is the standard deviation of latent signal, and J is a constant, chosen depending on the amount of noise present [100]. The value of J has been chosen as 7 in the literature based on the normal amplitude size distribution of the burst [95]. The values to the left of the proposed threshold are 0.99, implying that amplitudes exceeding this threshold should not exist between bursts of activity.

### 4.2.3 Selected repetition detection algorithm

The repetition detection algorithm employed uses the Teager-Kaiser energy operator in conjunction with a threshold-based analysis and some additional decision-making rules. A summary of the algorithm is presented in Figure 4.1.

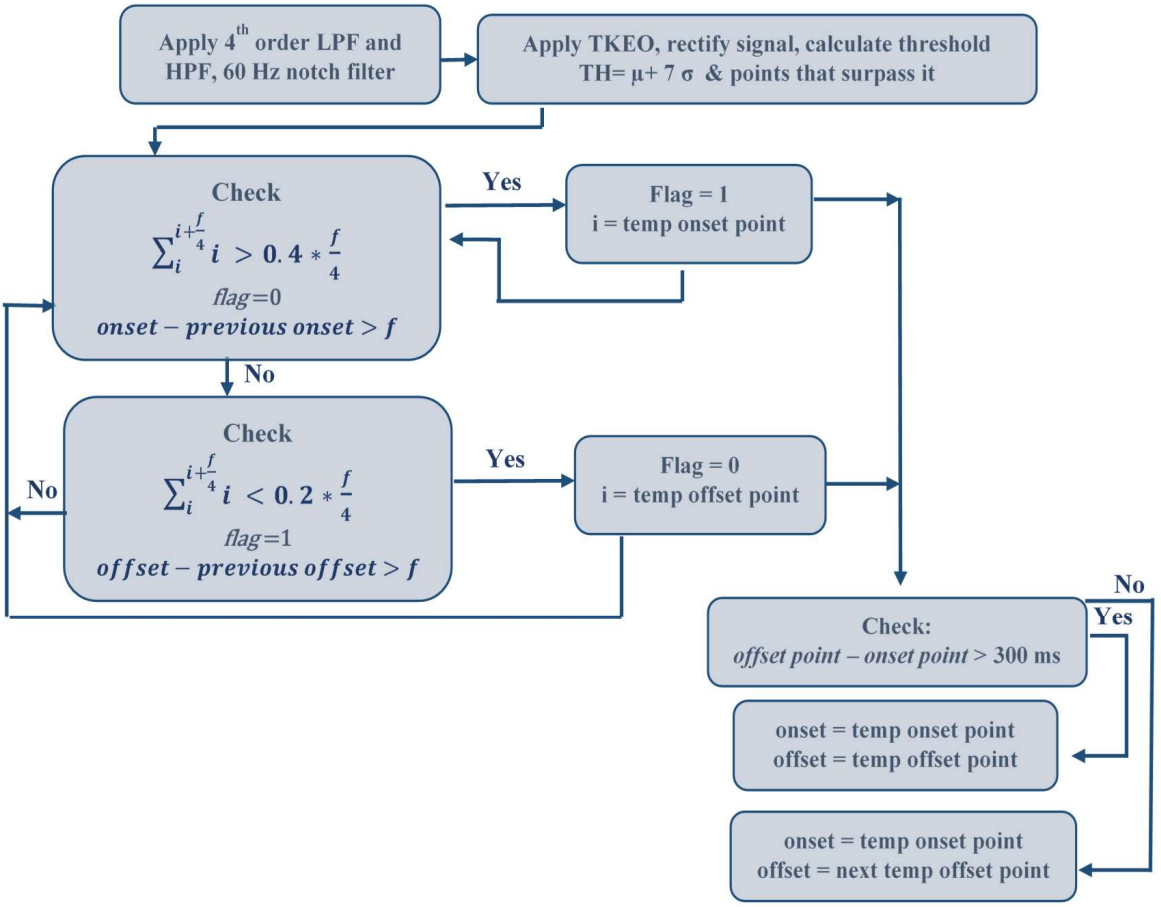


Figure 4.1: Summary of the algorithm used to process signals and detect motion repetitions.

This method first begins with some pre-processing filtering in software; the signal is de-trended, a $4^{th}$ order Butterworth bandpass filter with its lower cut off frequency at 10 Hz and a an upper cut off frequency of 500 Hz is applied to ensure that the signal remains within the expected range of an EMG signal. A notch filter is applied at 60 Hz to remove power line interference and the signal stream is rectified. From here, the Teager-Kaiser energy operator is applied to the filtered signal to improve the SNR. The resultant signal stream is rectified and a linear envelope is applied

through the use of a fifth order low pass Butterworth filter with a cutoff frequency of 3 Hz. A threshold is then calculated using Equation 4.2, where the variables $\mu$ and $\sigma$ are the mean value of the of the signal stream with the TKEO applied and the variance, respectively. A vector is created containing information on whether each data point falls above or below this threshold.

From here, temporary vectors containing onset and offset times are created based on the following decision making rules:

$$\begin{cases} \sum_{i}^{i+\frac{f}{4}} i > 0.4 \cdot \frac{f}{4} \\ flag = 0 \qquad\qquad = onset\ point \\ i - previous\ onset > f \end{cases}$$

$$\begin{cases} \sum_{i}^{i+\frac{f}{4}} i < 0.2 \cdot \frac{f}{4} \\ flag = 1 \qquad\qquad = offset\ point \\ i - previous\ offset > f \end{cases} \tag{4.3}$$

To determine an onset point from the threshold vector, the threshold vector was summed from the given data point, *i*, for the duration of $\frac{1}{4}$ second, which corresponds to the data point $i + \frac{1}{4}$ of the sampling frequency *f*. To be considered 'on', the threshold must be exceeded for 40 percent of those $\frac{f}{4}$ data points; as well, the on/off indicator flag must be set to zero to show that the repetition has yet to begin. Another rule is to check that more than one full second has occurred between the previous onset and the point in question.

Similarly, the offset point is found when the indicator flag has been set to '1', and the following $\frac{1}{4}$ second of data points fall below the threshold 20 percent of the time. Again, it is also checked that the previous offset time is over one full second before the proposed offset point, as it would be unrealistic for a full repetition, and its intention, to occur in less time.

If neither of these criteria sets are met, the data point is considered to be part of the current repetition if *flag = 1* or latent if *flag = 0*.

### 4.2.4 Expected motion profiles

The temporary onset and offset vectors face further scrutiny by ensuring that the duration of the repetition is greater than 300 ms, which is considered to be the amount of time required for the

nerve signal to reach the muscle and the action potential to occur. If this criterion is not met, the offset point is omitted and the following temporary offset point is used. As the onset-offset pairs have changed, the duration between the onsets of the new pairs are checked again such that the $i$-previous onset $>f$ is held true and false bursts can be removed. Based on an understanding of the anatomy of the upper limb, particular motion profiles are expected for each type of gross motion. The motions relevant to this work will be those associated with the four degrees of freedom outlined in Chapter 2. Here, a repetition of the motion is considered to be the profile through both ends of the ROM (for example, elbow flexion and extension). It would be defined as the onset of the primary muscle associated with the first half of the motion until the offset of the primary muscle associated with the second half of the motion. However, if multiple repetitions of the motion are performed without rest in between, repetitions may overlap. The muscle associated with the first half of the motion may activate prior to the full deactivation of the second part of the motion from the previous repetition. This is due to the fact that muscle activity occurs prior to the actual associated biomechanical motion. The motions considered, and their corresponding profiles, are as follows:

1. Elbow flexion–extension: While the elbow is flexing, the *biceps brachii* activates at a high amplitude. When the elbow moves through the neutral into an extension, the long head of the *triceps brachii* becomes active while the *bicep brachii* gradually deactivates. The profile per repetition begins at the *bicep brachii* onset and ends at the *triceps brachii*'s offset. The expected EMG readings from these two muscles, in terms of their normalized amplitudes, are shown below in Figure 4.2.

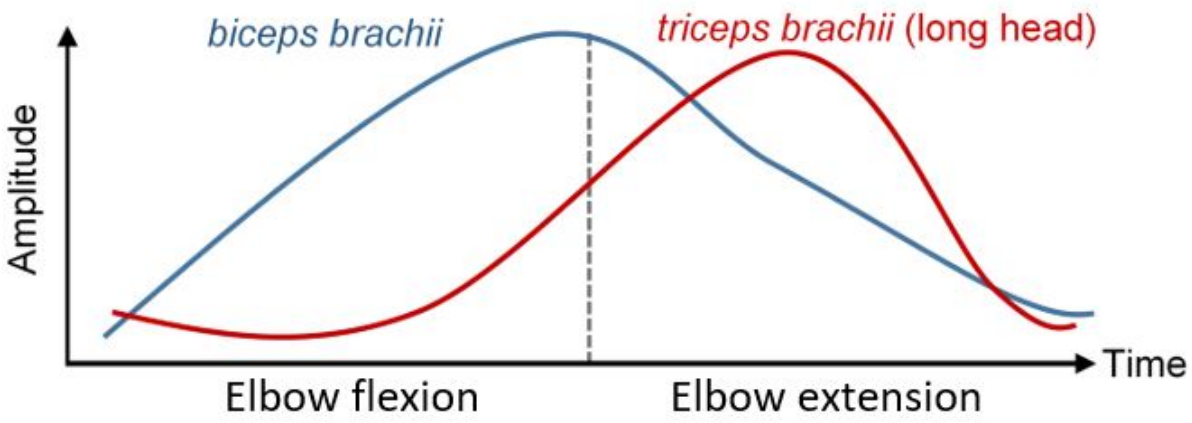


Figure 4.2: Expected motion profile of extending and flexing the elbow, shown in terms of the normalized amplitudes of EMG signals collected from the *biceps brachii* (blue) and the *triceps brachii* (red).

2. Forearm pronation–supination: The motion profile begins with the activation of the *biceps brachii* as the forearm supinates. It gradually deactivates while moving through the neutral position and the *pronator teres* activates throughout the pronation movement. The onset of the *biceps brachii* is the onset of the repetition, while the offset of the *pronator teres* indicates the end of the repetition. The expected EMG readings from these two muscles, in terms of their normalized amplitudes, are shown below in Figure 4.3.

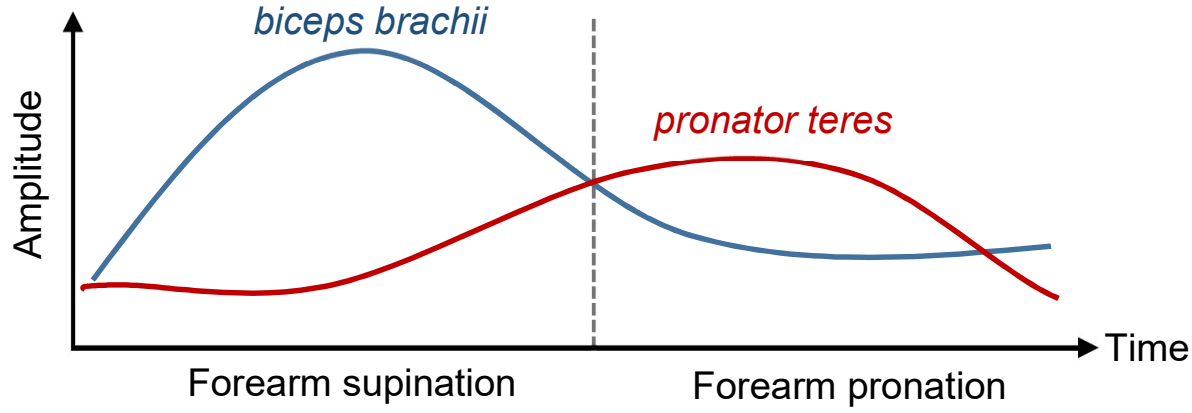


Figure 4.3: Motion profile of pronating and supinating the forearm, shown in terms of the normalized amplitudes of EMG signals collected from the *biceps brachii* (blue) and the *pronator teres* (red).

3. Wrist flexion–extension: The motion profile begins with the activation of the *flexor carpi ulnaris* during the flexion of the wrist. While moving through neutral, this muscle deactivates and the *extensor carpi ulnaris* activates through the wrist's extension. The repetition onset is the onset of the *flexor carpi ulnaris* and the offset is that of the *extensor carpi ulnaris*.The expected EMG readings from these two muscles, in terms of their normalized amplitudes, are shown in Figure 4.4.

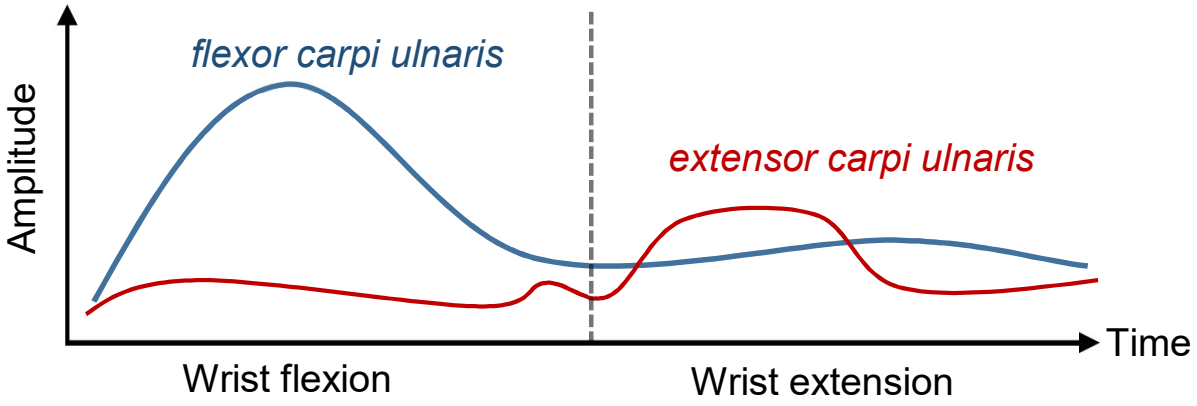


Figure 4.4: Motion profile of extending and flexing the wrist, shown in terms of the normalized amplitudes of EMG signals collected from the *flexor carpi ulnaris* (red) and the *extensor carpi ulnaris* (blue).

4. Radial–ulnar deviation: The expected EMG reading that indicates the occurrence of a radial–ulnar deviation repetition begins with the deactivation of the *extensor carpi ulnaris*, the *pronator teres*, and the *flexor carpi ulnaris* while radial deviation occurs. When moving through the neutral position towards ulnar deviation, the normalized amplitude of all three muscle signals gradually increases. The amplitude falls again when ulnar deviation is reached, marking the offset of the repetition. These expected EMG readings are displayed in Figure 4.5.

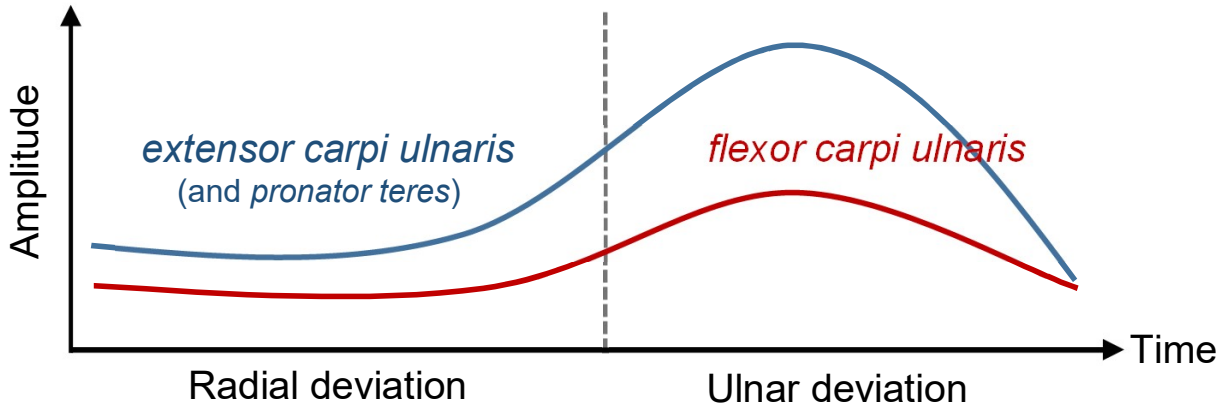


Figure 4.5: Motion profile of ulnar and radial deviation, shown in terms of the normalized amplitudes of EMG signals collected from the *flexor carpi ulnaris* (red), the *extensor carpi ulnaris* , and the *pronator teres* (blue).

These expected motion profiles were established in order to classify gross-motion profiles using the algorithm from Section 4.2.3 with an existing EMG database.

## 4.3 Repetition Detection on an Existing Database

Initially, the algorithm described in the previous section was tested on an existing database created by a previous student in the Wearable Mechatronics Laboratory at the Western University [103]. The purpose was to determine the efficacy of the algorithm and search for areas for improvement.

### 4.3.1 Data collection set-up

The existing database consists of 33 data sets, in all, collected at the Hand and Upper Limb Clinic at Saint Joseph's Hospital in London, Ontario. Eight of these were considered to be "bad" by the student who collected the data. Of the remaining 25 subjects, 11 were healthy and 14 were upper limb MSD patients who had sought physical rehabilitation.

The trial data were collected using a standard electrophysiological amplifier system with signal conditioning, the Intronix Model 2024, which is able to record four channels of EMG data. As it relies on conventional Ag/AgCl electrodes, the system has a low input impedance of 10 ohms. This data were then input to a computer using National Instruments' NI DAQ N19205 data acquisition system. This system is capable of collecting 32 channels of data in the +/- 10 V range

simultaneously at a maximum rate of 250 Kb/s and a precision of 16 bits. Following the DAQ, the data reached a PC, where the data are recorded by a proprietary software suite, the Intronix Model 8008 Myoguide system.

Data were collected from each patient by placing gelled Ag/AgCl electrodes at each of the following six muscle sites:

1. *biceps brachii*
2. *triceps brachii* (proximal head)
3. *triceps brachii* (long head)
4. *pronator teres*
5. *flexor carpi ulnaris*
6. *extensor carpi ulnaris*

The electrodes used were Ambu Blue Sensor NF floating electrodes. Two electrodes were placed 20 cm apart over the muscle belly for a complete bipolar electrode configuration. A reference electrode was also placed over the elbow.

### 4.3.2 Data collection procedure

Prior to collecting data, subjects were seated at a comfortable height, relevant anthropomorphic data were measured, skin was prepared, and electrodes were placed in accordance to SENIAM standards. Data were collected at the six muscle sites for a total of six motions; however, the subject's baseline, EMG burst, and maximum voluntary contraction of the biceps and triceps were verified first.

The subject was asked to preform three repetitions of each of the motions described below:

1. Elbow flexion–extension: The subject sat with the shoulder aligned with the torso. Beginning in a neutral position, the subject was asked to lower the arm, extending it through their maximum range of motion (ROM). Then, the subject bended the elbow, flexing to their maximum ROM.

2. Wrist flexion–extension: The subject sat with the shoulder aligned with the torso, the elbow bent at a 90 angle, and the wrist in a neutral position with the palm facing downwards. The subject was asked to extend their wrist downwards and then flex it upwards through their maximum ROM.

3. Hand open–close: The subject sat with the shoulder aligned with the torso, the elbow bent at a 90 degree angle, the wrist in a neutral position, and the fist open with the fingers spread apart. The subject was asked to close their fist and then release back to the initial position.

4. Ulnar–radial deviation: The subject sat with the shoulder aligned with the torso, the elbow bent at a 90 degree angle, the wrist in a neutral position, and the palm facing medially. The subject was asked to first deviate the hand downwards, to deviate towards the ulna, and then upwards towards the radius through their maximum ROM.

5. Pronation–supination of the forearm: The subject sat with the shoulder aligned with the torso, the elbow bent at a 90 degree angle, and the palm facing downwards in a pronated position. The subject was asked to rotate the forearm until the palm was facing upwards and the forearm was supinated.

6. Pushing on a ball: A ball was placed on a table in front of the seated subject. The subject was asked to push downwards onto the ball, stabilizing it, with the forearm perpendicular to the table.

The data for all six channels for each repetition of each of these motions were saved separately on the PC in an .edf format [103].

### 4.3.3 Data processing and algorithm iteration

In order to isolate the data for the individual repetitions of each motion, a series of MATLAB functions were created. The structure of this software can be seen in the diagram below.

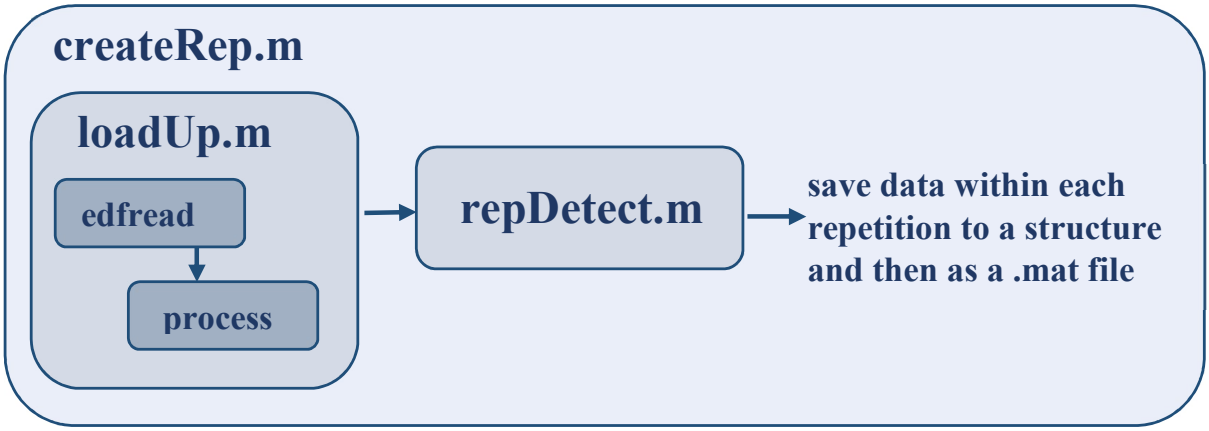


Figure 4.6: Flowchart describing the MATLAB structure for repetition detection.

Here, the createRep.m function was considered to be the main function of the script. It inputs the subject number and the motion type as strings to pass along to the loadUp.m function.

The loadUp.m function inputs the patient number and motion type to determine the location of the file to be analyzed. This file is loaded using the edfread function from Intronix, which allows one to read the data collected with the Intronix Model 8008 Myoguide system. Afterwards, each channel of data were placed through the process function. This took in the desired signal stream and its length. Here, the data were detrended, filtered, rectified, and linear enveloped, as described in Section 4.2.3. The data were returned in two forms: as the final, linear enveloped data set and just filtered. The loadUp.m function returned the fully processed data from each channel, as well as the filtered-only data from the two primary muscle channels for the given motion. The relevant channels were selected via a switch statement based on the input motion string.

Once this information was returned to createRep.m, the relevant data channels were then input to repDetect.m. This function determined the onset and offset points of the input muscle channel using the selected algorithm, described in Section 4.2.3. The TKEO was applied, the threshold calculated, and the onsets and offsets were determined; however, through plotting some of the data collected and using visual analysis, it became evident that not all EMG bursts appeared to have a single peak. In some datasets, there appeared to be two peaks per repetition. In order to counteract that, additional decision-making rules were added, as follows:

- When there were six onset times, it was observed that there were two peaks per repetition;

consequently, the odd-numbered onset times and even-numbered offset times were matched up.

- For five onset times, it could be seen that the first two repetitions were double-peaked and the final repetition's activation was cut-off slightly; to compensate, the odd-numbered onset times were matched up with the even-numbered offsets. Here, the fifth offset also remained as the end of the third repetition.

- In the case of four onset times, there was a false burst that occurred within a repetition. To isolate it, the duration of each onset–offset pair was calculated and the shortest repetition was isolated. The distance between the beginning of this repetition and the end of the previous one was calculated, as well as the end of the isolated repetition and the start of the following one. If the former value was smaller, the isolated repetition's end point becomes the offset point of the previous repetition and its former endpoint was discarded. The inverse was true if the latter value was smaller.

In addition to false EMG bursts, an additional adjustment must be made. The data that this algorithm was run on has not been linear enveloped; however, this is untrue for data used for feature characterization and classification. The envelope changes the shape of the signal stream to make the onsets and offsets more gradual. Visually, it was determined that a safety factor of -/+0.45 s should be applied to the onset and offset points for a more accurate result. This buffer is necessary due to the combined group delay of the band-pass, notch, and linear envelope digital filters. In this work, there should not have been any phase delay due to the use of Matlab's "filtfilt" command, which uses backwards-forwards filtering.

These onset and offset points for each muscle are returned to the createRep.m function. Then, the onset time for the motion profile are assigned as the onsets of the first muscle channel and the offsets as the offsets from the second muscle channel. A structure is created where, for each repetition, a field name is generated and the corresponding data points for all six channels are added. The getfield.m function is used to extract each repetition's data and field name to be saved as a .MAT file.

### 4.3.4 Results and discussion

Of the 23 remaining data sets, the repetition detection algorithm was found to be moderately successful. As the algorithm's rules were determined in order to find the onset and offset points visible to the human eye, the inability of the algorithm to find these points where visual detection failed is to be expected. Table 4.1 presents a summary of the success of the algorithm, where a dash indicates a success, i.e., where the algorithm detected three repetitions at points comparable to visual detection, or an 'x' indicates a failure. Other notes indicate whether parts of repetitions could be detected, such as if the onset and offset times could be detected for one of two primary muscles in the motion profile. In the table, the column "subject type" refers to the muscle health, or the time elapsed since injury. The key is as follows:

- 0: Subject's status unknown
- 1: Healthy subject
- 2: Patient 4+ months following injury
- 3: Patient 3–4 months following injury
- 4: Patient 2–3 months following injury
- 5: Patient 1–2 months following injury
- 6: Patient 0–1 month following injury

As seen in Table 4.1, the ability of the algorithm to detect onset and offset times is effective, providing that these times can be determined through visual detection (V/D). Tables 4.2 and 4.3 breaks down the success of the algorithm for each motion. In Table 4.2, the results are split into five categories; here, V/D error indicates that the repetitions cannot be determined through visual detection and partial success indicates that onset and offset times were only detectable for one of the primary muscles. The values in the table are the quantity of datasets that correspond to each category.

There were a significant number of visual detection errors encountered while testing the repetition detection algorithm. These unclear signal streams may be the result of improper electrode placement, loose and detaching electrodes, unrestrained movement, or poor gain settings applied

Table 4.1: Success of repetition detection algorithm by motion type.

| **Subject ID** | **Subject Type** | **Data Quality** | **Notes** | **EFE** | **PS** | **WFE** | **URD** | **HOC** |
|---|---|---|---|---|---|---|---|---|
| S31-1 | 2 | Good | | x | pt only | - | - | - |
| S31-2 | 2 | Good | | - | pt only | - | - | ecu only |
| S33-3 | 2 | Good | No URD, PS | no V/D | no file | - | no file | - |
| S36-1 | 5 | Good | NO HOC | - | - | - | - | no file |
| S37 | 2 | Good | | - | - | - | no V/D, ecu | - |
| S38 | 5 | Good | | x | - | 2 reps ecu | ecu only | x |
| S39 | 2 | Good | | - | no V/D | - | - | no V/D |
| S40 | 1 | Good | | - | no V/D | ecu only | - | - |
| S41 | 1 | Good | | - | - | - | - | ecu only |
| S42 | 1 | Good | | - | no V/D | - | ecu only | - |
| S43 | 2 | Good | | - | - | - | - | no file |
| S44 | 6 | Good | | - | - | ecu only | no V/D | ecu only |
| S45 | 6 | Partial | | - | no V/D | ecu only | no V/D | no file |
| S46 | 5 | Good | | - | - | - | fcu only | - |
| S47 | 3 | Good | | - | - | - | - | - |
| S48 | 1 | Good | | - | pt only | - | - | - |
| S49 | 1 | Good | | - | - | - | - | ecu only |
| S50 | 1 | Good | | only 2 reps, tb | pt only | - | - | - |
| S51 | 1 | Good | | bb only | - | - | - | - |
| S52 | 1 | Good | | - | - | - | - | - |
| S57 | 1 | Good | | - | - | ecu only | - | no V/D |
| S58 | 1 | Good | | - | - | - | fcu only | - |
| S59 | 1 | Good | | - | - | - | - | - |

Table 4.2: Success of repetition detection algorithm by motion type.

| | **EFE** | **PS** | **WFE** | **URD** | **HOC** |
|---|---|---|---|---|---|
| Success | 18 | 17 | 19 | 17 | 14 |
| Failure | 2 | 0 | 0 | 0 | 0 |
| Partial success | 1 | 0 | 1 | 1 | 2 |
| V/D error | 2 | 5 | 2 | 4 | 4 |
| No file | 0 | 1 | 1 | 1 | 3 |

Table 4.3: Success and failure percentages of repetition detection algorithm by motion type.

| | **EFE** | **PS** | **WFE** | **URD** | **HOC** |
|---|---|---|---|---|---|
| Success (% ) | 90.455 | 100 | 97.5 | 96.7 | 93.75 |
| Failure (%) | 9.455 | 0 | 2.5 | 3.3 | 6.25 |

to the collection channel. As well, the primary muscle of the motion may not be activated as expected if the subject performs the motion in a different manner, compensating with the activation of another muscle instead. The aforementioned sources of error may also rationalize partial successes, where there were errors with only one of the channels. In some cases, extreme drift in the collected signal stream prevented the threshold detection portion of the algorithm from behaving as desired.

Table 4.3 displays the success and failure for each motion, calculated as a percent of the number of datasets that existed without visual detection error. The percentage that would be associated with "Partial Success" is divided evenly among the success and failure rates, as successful use of the detector was used for one of the muscles. It is apparent that the repetition detection of the pronation–supination was most successful; however, the motion also had the greatest number of visual detection errors. Elbow flexion–extension was the least successful, as it was the only motion to have full failures.

The data were further analyzed to determine if the success rate was dependent on the subject's muscle health; ultimately, there is not enough data to make a definitive conclusiom, as seen in Table 4.4. There was only one dataset for Categories 3 and 6, two datasets for Category 5, and none in Category 4. There are no linear trends related to failures and partial success rates; although, there is a vague increasing trend in visual detection errors as the time from injury decreases. Providing that the quality of the data collected is sufficient, the algorithm will remain successful.

To further illustrate the success of the algorithm, the motion profile of the four motions dis-

Table 4.4: Success and failure percentages of repetition detection algorithm by patient classification.

| | **1** | **2** | **3** | **4** | **5** | **6** |
|---|---|---|---|---|---|---|
| Success (% ) | 85.45 | 67.9 | 100 | 0 | 50 | 60 |
| Failure (%) | 0 | 3.6 | 0 | 0 | 10 | 0 |
| Partial success (%) | 5.45 | 7.1 | 0 | 0 | 20 | 0 |
| V/D error (%) | 9.1 | 21.4 | 0 | 0 | 20 | 40 |

cussed in Section 4.2.4 is shown from both a healthy subject, Subject 59, and a Subject 1–2 months into their physical rehabilitation regimen, Subject 36. The two sets of plots are fairly similar to one another and to those in Section 4.2.4, indicating that the algorithm was able to detect motion repetitions that corresponded with the expected motion profiles. The plots are organized by motion type, wherein the healthy subject's plots precede the injured subject's plots.

#### 4.3.4.1 Elbow flexion–extension sample plots

Figures 4.7 and 4.8 display the elbow flexion–extension motion profiles of Subject 59 from the existing database. As indicated in Table 4.1, this subject is healthy and the onset–offset detection algorithm was found to be successful for the elbow flexion–extension motion. The plot shows the recorded EMG signal stream of the *biceps brachii* and *triceps brachii* over time, expressed as the sample number. The amplitude of each EMG signal is normalized with respect to its own maximum value.

The first figure, Figure 4.7, displays the entire signal stream of both muscles of interest. The asterisks indicate the points where the algorithm detects the onset of a repetition, which occur where the *triceps brachii* began to activate; consequently, the dots indicate the detected offset points, when the *biceps brachii* deactivate at the end of the motion.

Figure 4.7: Detection of onsets and offsets across the entire recorded signal stream of three repetitions of EFE in a healthy subject from the existing database.

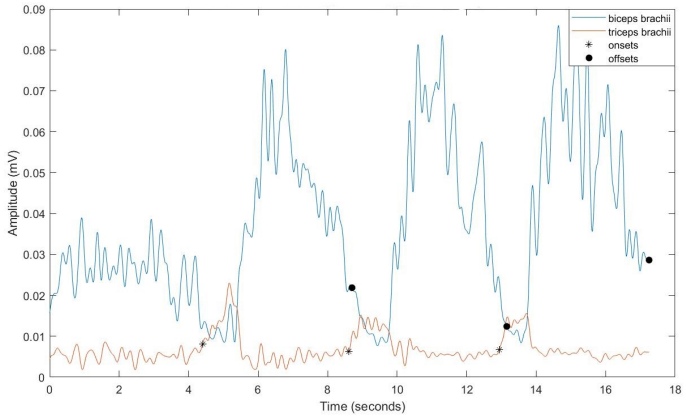


Figure 4.8 shows a single repetition of Subject 59's elbow flexion–extension motion. The normalized amplitude data from the signal stream is extracted from the one of the algorithm's detected onset points until its corresponding offset point. This provides a clear view of motion profile, comparable to that of Figure 4.2.

Figure 4.8: Motion profile of a single repetition of EFE in a healthy subject from the existing database.

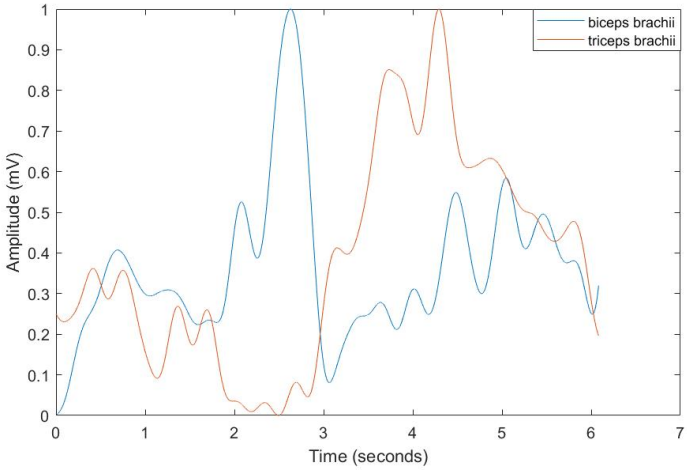


Figures 4.9 and 4.10 are analagous to Figures 4.7 and 4.8, respectively; however, the data used is the EMG recordings of the *biceps brachii* and *triceps brachii* of Subject 46. As stated in Table 4.1, this data were recorded only 1–2 months after seeking treatment for the injury.

Figure 4.9: Detection of onset and offset points across the entire recorded signal stream of three repetitions of EFE in a subject 1–2 months following injury from the existing database.

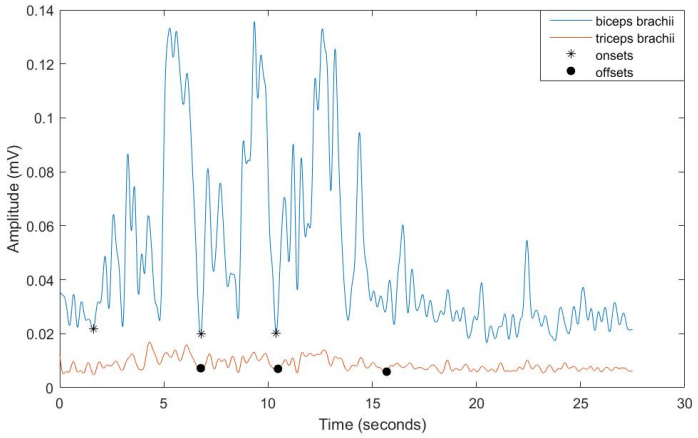


Figure 4.10: Motion profile of a single repetition of EFE in a subject 1–2 months following injury from the existing database.

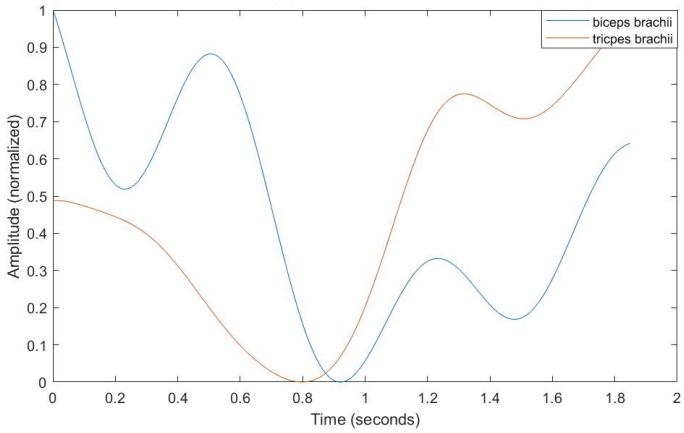


Through Figures 4.9 and 4.10, it appears as though the algorithm was able to determine appropriate onset and offset points for three repetitions, even with slightly different muscle activation patterns or intensities due to injury.

#### 4.3.4.2 Forearm pronation–supination sample plots

Figures 4.11 and 4.12 display the EMG data of interest for the forearm pronation–supination motion collected from Subject 59. Like Figures 4.7 and 4.8, the plots show the filtered and normalized EMG amplitudes of interest with respect to the sample number; here, the muscles of

interest are the *biceps brachii* (red) and the *pronator teres* (blue). Figure 4.11 shows the full signal stream of three repetitions, with the subject's forearm began in the pronated position, moving through neutral, and then into supination. The onset and offset points of each repetition are marked with asterisks at the onset of the *pronator teres* and dots at the offset of the *biceps brachii*. The motion profile of the single repetition in Figure 4.12 appears inverted from Figure 4.3 due to the opposite starting position.

Figure 4.11: Onsets and offsets of three repetitions of PS in a healthy subject.

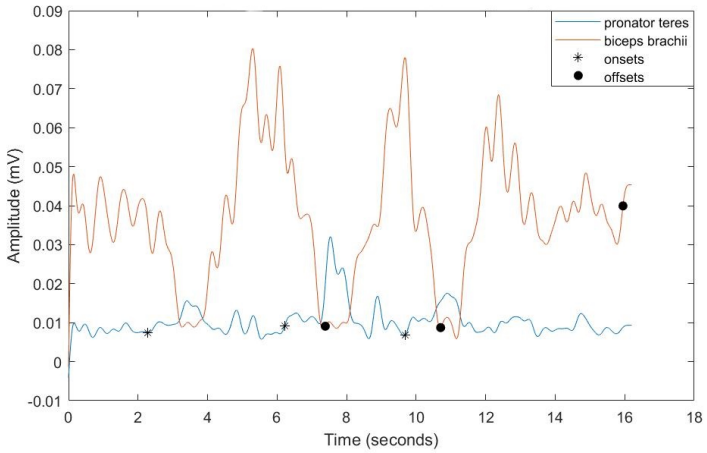


Figure 4.12: Motion profile of a single repetition of PS in a healthy subject from the existing database.

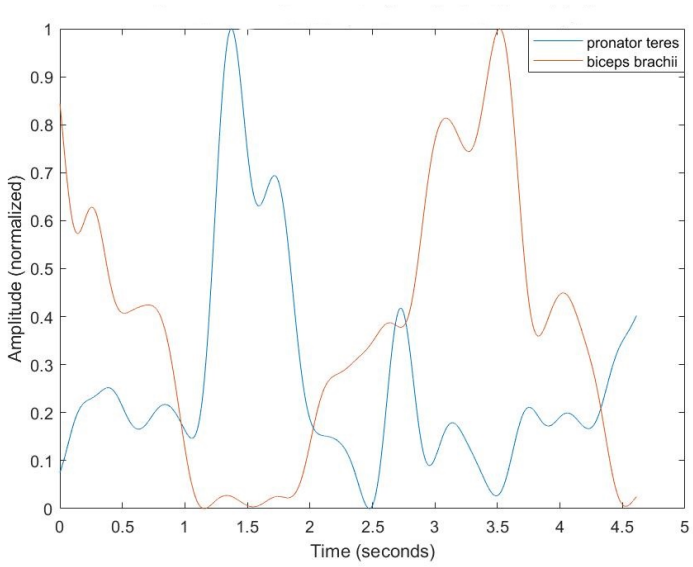

Similarly, Figures 4.13 and 4.14 are display the same information as Figures 4.11 and 4.12 using the data obtained from Subject 46, who was patient receiving care 1–2 months following injury.

Figure 4.13: Detection of onset and offset points across an entire recorded signal stream of three repetitions of PS in a subject 1–2 months following injury from the existing database.

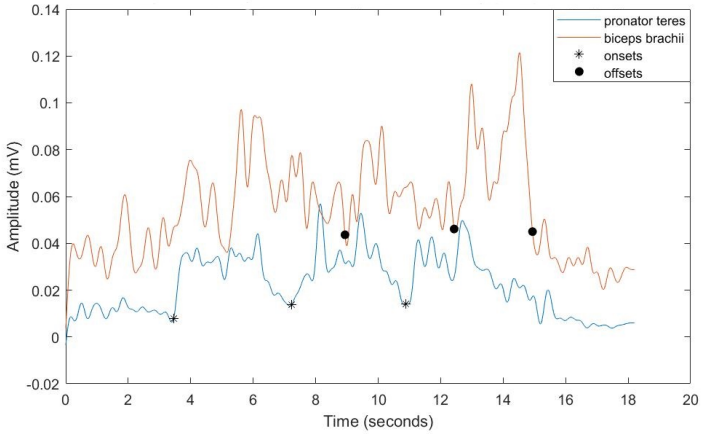


Figure 4.14: Motion profile of a single repetition of PS in a subject 1–2 months following injury from the existing database.

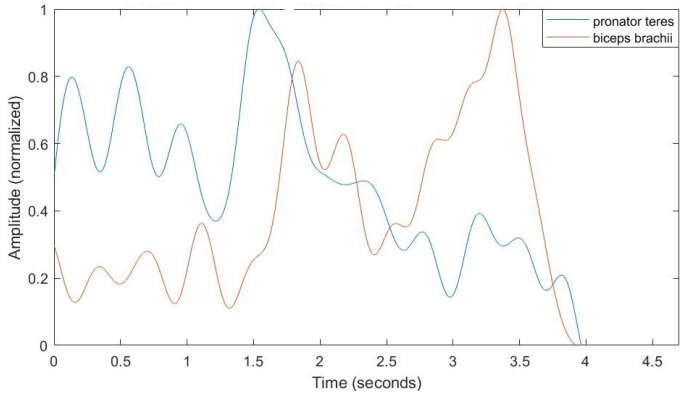


#### 4.3.4.3 Wrist flexion–extension sample plots

Figures 4.15 and 4.16 display the EMG signals of interest for the wrist flexion–extension motion performed by the healthy sample subject, Subject 59. The former shows the entire signal stream of three WFE repetitions, where asterisks along the activation of the *flexor carpi ulnaris* mark the onset, which is the beginning of flexion, and dots along the *extensor carpi ulnaris* (red) signal denote the offset points. Figure 4.16 shows a singular repetition from the signal stream, where the

subject first flexes and then extends the wrist. This plot is comparable to the expected motion profile shown in Figure 4.4.

Figure 4.15: Detection of onsets and offset points across an entire signal stream of three repetitions of WFE in a subject healthy subject from the existing database.

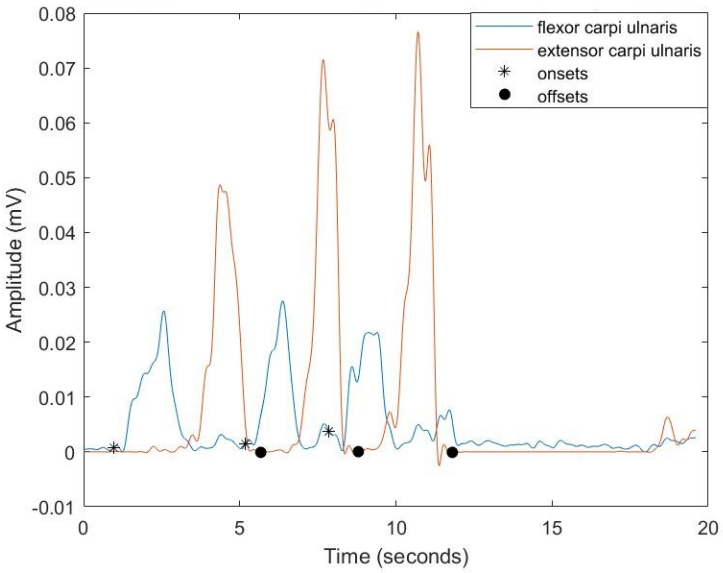


Figure 4.16: Motion profile of a single repetition of WFE in a healthy subject from the existing database.

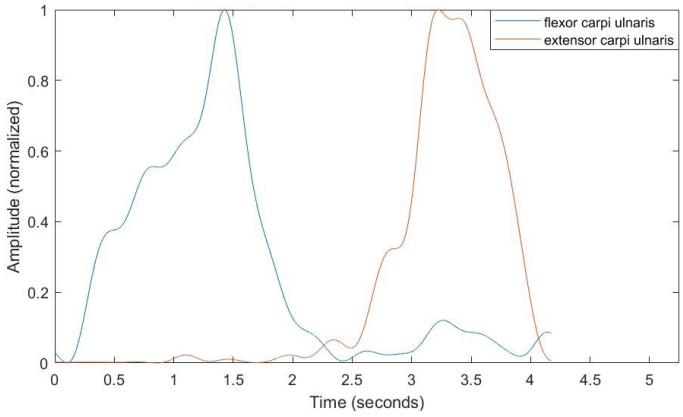


The following two figures, Figures 4.17 and 4.18 show the same motion profiles and muscles of interest as Figures 4.15 and 4.16; however, the data input to the algorithm and displayed below are obtained from Subject 46, a subject 1–2 months post-injury at the time of recording.

Figure 4.17: Detection of onsets and offset points across the entire recorded signal stream of three repetitions of WFE in a subject 1–2 months following injury from the existing database.

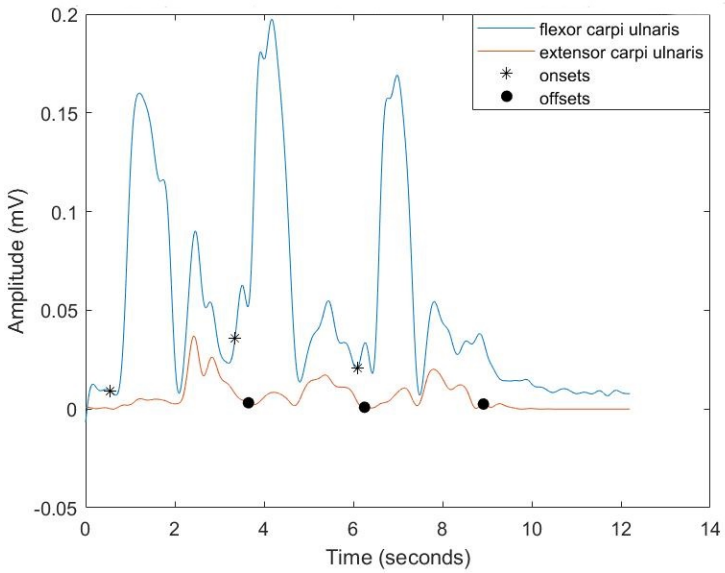


Figure 4.18: Motion profile of a single repetition of WFE in a subject 1–2 months following injury from the existing database.

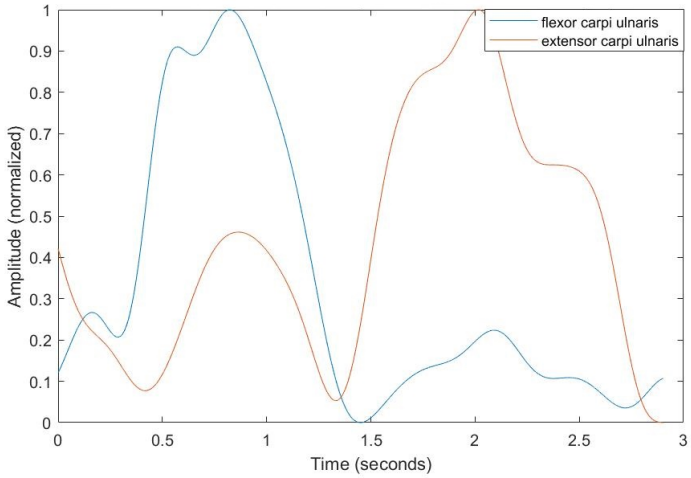


#### 4.3.4.4 Ulnar–radial deviation

Figures 4.19 and 4.20 show the key ulnar–radial deviation muscle activity of Subject 59, a healthy subject. Figure 4.19 shows the three onset and offset points of the EMG activation of the *flexor*

*carpi ulnaris* (red) and *extensor carpi ulnaris* (blue) through the recorded signal stream. During ulnar–radial deviation, the two muscles of interest activate concurrently, but the onset asterisks on the plot are found along the *extensor carpi ulnaris* and the offset dots along the *flexor carpi ulnaris* due to the points determined by the algorithm. Figure 4.20 shows a singular repetition extracted from the signal stream.

Figure 4.19: Detection of onsets and offset points across an entire signal stream of three repetitions of URD in a healthy subject from the existing database.

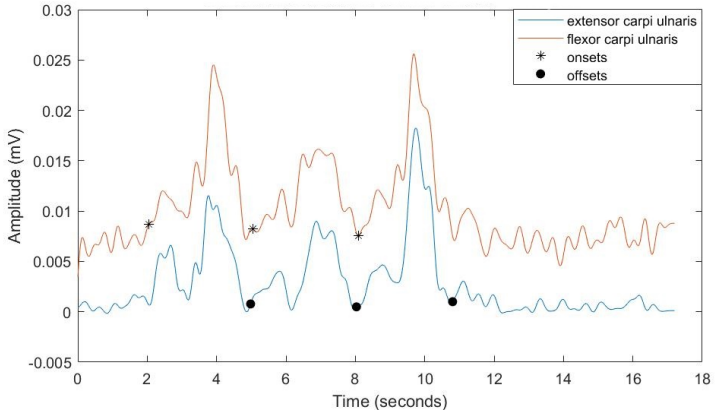


Figure 4.20: Motion profile of a single repetition of URD in a healthy subject from the existing database.

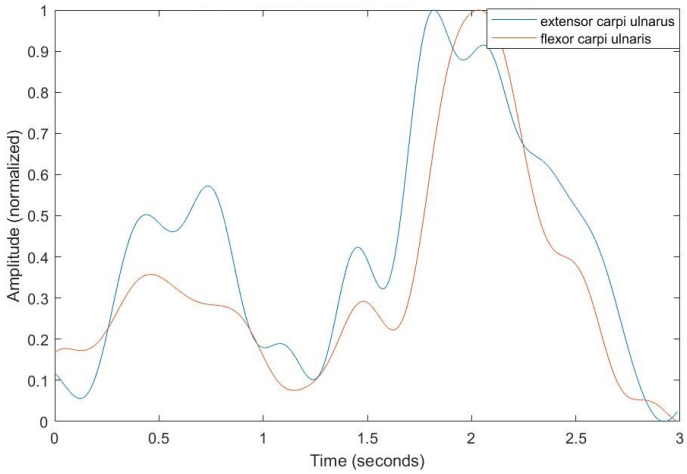


Figures 4.21 and 4.22 are analogous to Figures 4.19 and 4.20, substituting the data obtained from a healthy subject for that recorded from Subject 46, a subject 1–2 months into their reha-

bilitation regimen post-injury.

Figure 4.21: Detection of onset and offset points across the entire recorded signal stream of three repetitions of URD in a subject 1–2 months following injury from the existing database.

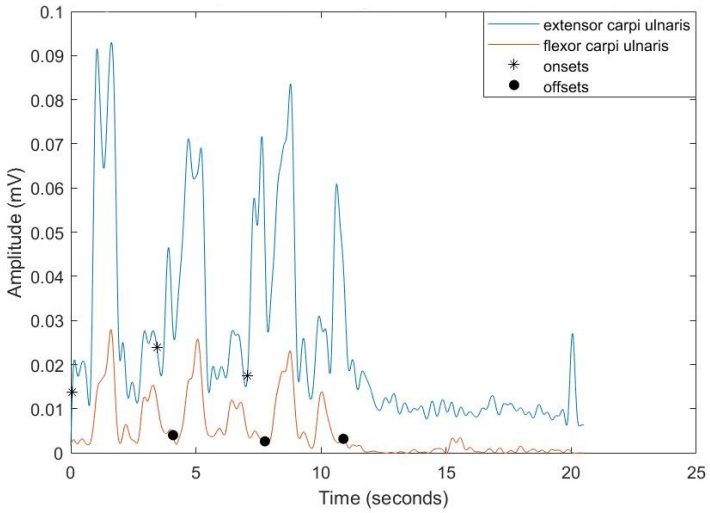


Figure 4.22: Motion profile of a single repetition of URD in a subject 1–2 months following injury from the existing database.

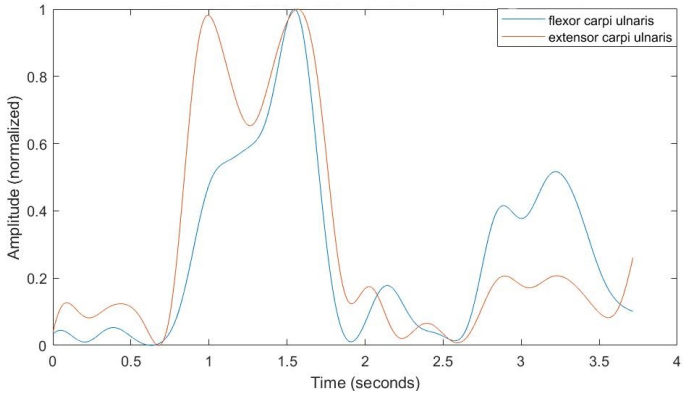


## 4.4 Repetition Detection using the Biosignal Acquisition Sleeve Prototype

Following the repetition detector's validation using the existing EMG data set, the algorithm was tested using data collected from the biosignal acquisition sleeve prototype described in Chapter 3.

This ensured that the detector is adaptable to various EMG acquisition technologies and was not only functional with the set-up used by the previous student. Ambu Blu Ag/AgCl electrodes were placed on the same sensor sites as the existing data and the same motions described in Section 4.3.1.

### 4.4.1 Data collection and processing from the biosignal acquisition sleeve

To demonstrate the efficacy of the repetition detection algorithm on low-cost devices, data were colected using the biosignal acquisition sleeve's ADS1292R module, a two channel 24-bit ADC capable of collecting data from two unipolar muscle sites and a driven right leg signal. Initially, this EMG sensing modality was used to collect data from a single repetition of each of the four gross motions. This served as a visual validation to ensure that the collection and filtering were correctly implemented. As the data from the sleeve was saved as a comma delimited list on a microSD card, an alternative data input process was implemented in the "loadUp.m" function, hereby known as "loadUp2.m". This version also uses the trial number and motion type as inputs to the function; however, the module type is also required, as use of the ADS1292R module requires conversion of the data from a signed long to a representative voltage. The module chosen also informed the data's sampling rate, which was required to correctly implement the filters and later determined the factor by which the data were interpolated to avoid editing the "repDetect.m" function. Following the validation of the single repetition profiles, adjustments were made to limit the search window for onset and offset detection points. This modified version of the algorithm was then used on a series of test data to determine the efficacy of the algorithm.

#### 4.4.1.1 Motion profile validation of single repetitions

As described in Section 4.4.1, single repetitions of each gross motion were recorded from the biosignal acquisition sleeve and processed using the MATLAB script. These preliminary results are shown in Figure 4.23.

Figure 4.23: Single repetition test of the four gross motions performed using the biosignal acquisition sleeve. Each pair of plots consists of: the top plot, showing the orientation of the limb segment with respect to time; and the bottom plot, showing the normalized activity of the motion's two dominant muscles with respect to time.

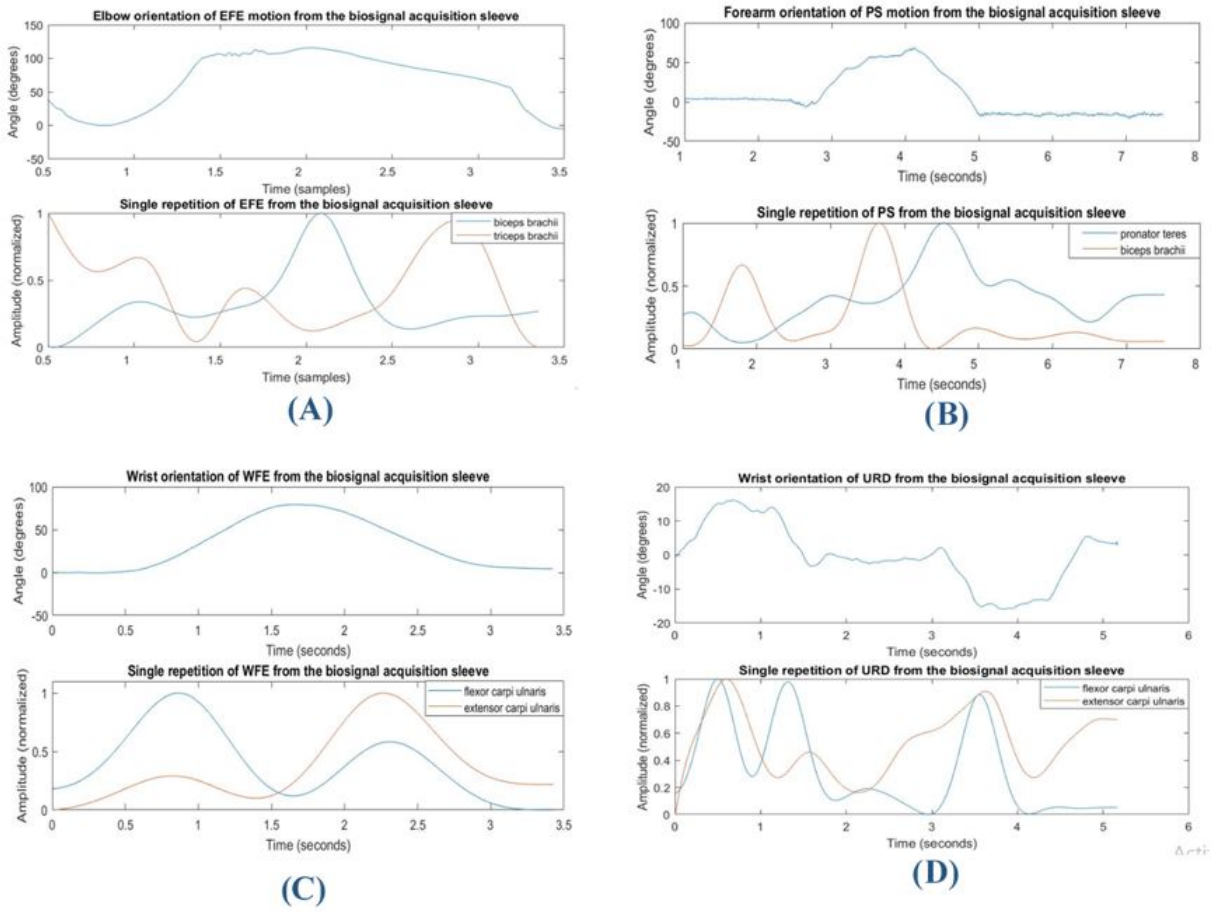


Figure 4.23 shows single repetitions of (A) elbow flexion–extension, (B) forearm pronation–supination, (C) wrist flexion–extension, and (D) ulnar–radial deviation. The results were comparable to the isolated repetitions found using the repetition detection algorithm on the existing EMG signal database in Section 4.3.4. As well, the apparent onset and offsets of the EMG signals coincided with the apparent onset and offset of the change in orientation. This is sufficient to proceed onto attempting detection of multiple motion repetitions.

#### 4.4.1.2 Time window search adjustment of repetition detection

After collecting a series of data from the biosignal acquisition sleeve where the motion repetitions were performed three times, it was apparent that other disturbances dominated portions of the signal stream where the inertial sensors showed no activity. This is largely due to the fact that the motions were performed in an unconstrained manner, allowing for imperfect motion or movement to occur before or after the repetitions were completed. In order to counteract these shortcomings and accurately determine onset and offset points, the search window was reduced; to do so, the region of activity was found based on the IMU data zero-velocity crossings. The region between the first zero-crossing to the penultimate zero-crossing was the basis for the window. A safety factor of one eight of the window length was added to either side of the window, as EMG activity often occurs prior to the start of mechanical motion.

Figure 4.24: Demonstration of the effects of reducing the search time window in which repetition onsets and offsets are performed.

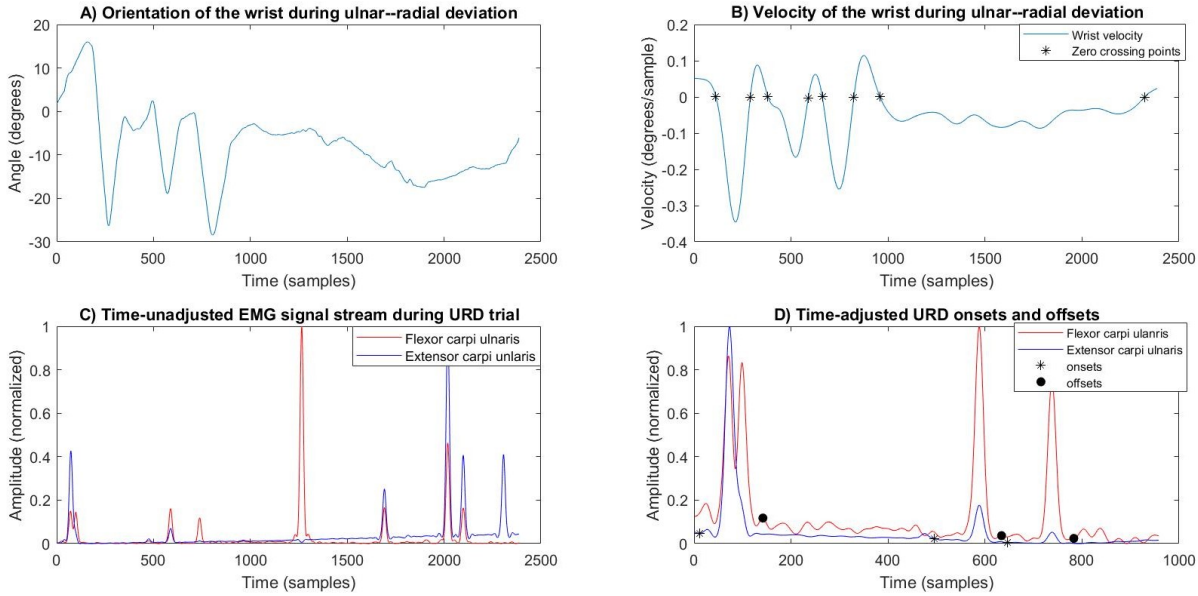


This newly-determined window was then used to inform the input index range of the raw EMG data processed within the "loadUp2" function. The results of the reduced search window for repetition detection is shown in Figure 4.24. Here, the onset and offset points found through reducing the search window corresponded to those of the biomechanical motion.

### 4.4.2 Results of the adjusted algorithm using the biosignal acquisition sleeve

Three repetitions of elbow flexion–extension, forearm pronation–supination, wrist flexion–extension, and ulnar radial–ulnar deviation motions were each performed multiple times by three healthy subjects using the biosignal acquisition sleeve. Ultimately, five datasets of each motion performed by each subject were used to test the adjusted algorithm. For data to be included in the test, it was required that visual detection was possible for the onset–offset points of at least one of the muscle's signal streams. As well, an equal number of datasets were to be used for each subject and motion. Similarly to Section 4.3.4, Figures 4.25, 4.26, 4.27, and 4.28 display the signal streams of both muscles of interest, with asterisks indicating onset points and filled dots to indicate offset points of motion.

Figure 4.25: Detection of onsets and offsets across the entire recorded signal stream of three repetitions of EFE using the biosignal acquisition sleeve.

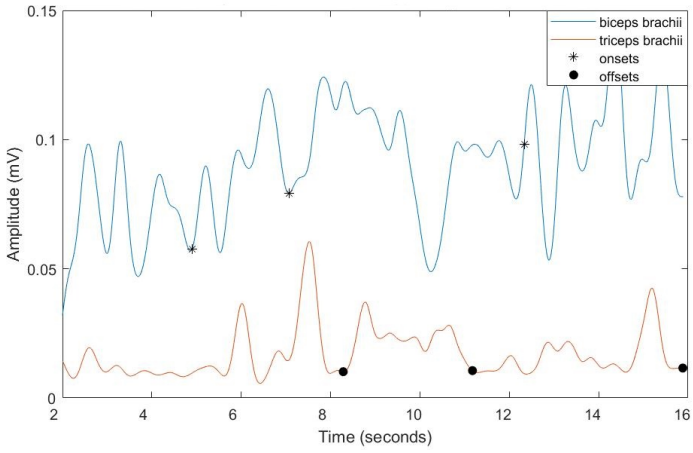

Figure 4.26: Detection of onsets and offsets across the entire recorded signal stream of three repetitions of PS using the biosignal acquisition sleeve.

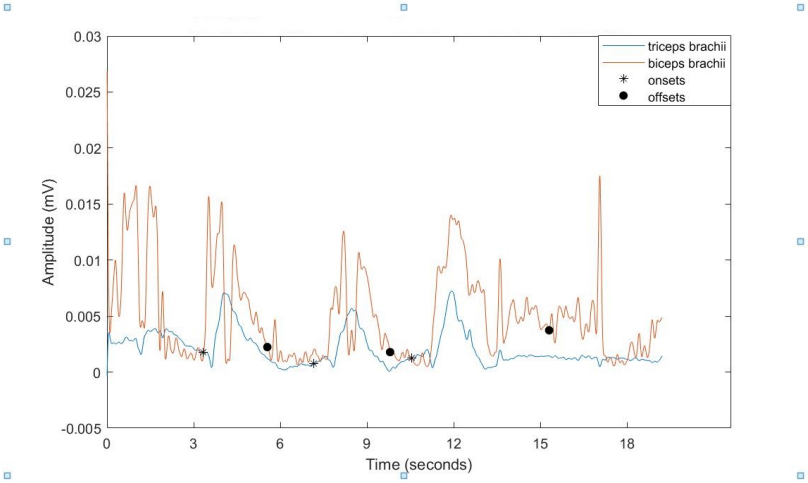


Figure 4.27: Detection of onsets and offsets across the entire recorded signal stream of three repetitions of WFE using the biosignal acquisition sleeve.

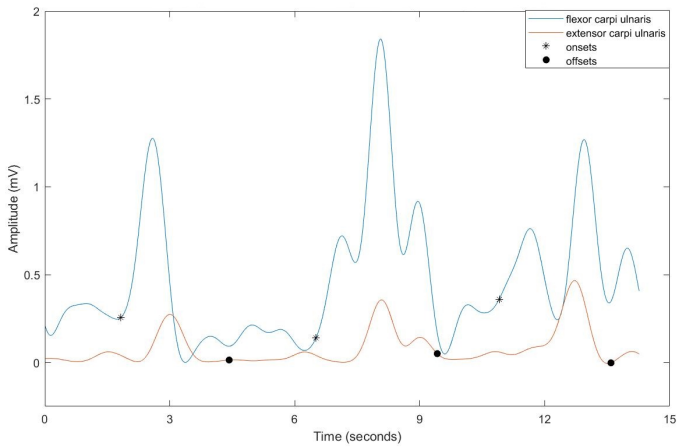

Figure 4.28: Detection of onsets and offsets across the entire recorded signal stream of three repetitions of URD using the biosignal acquisition sleeve.

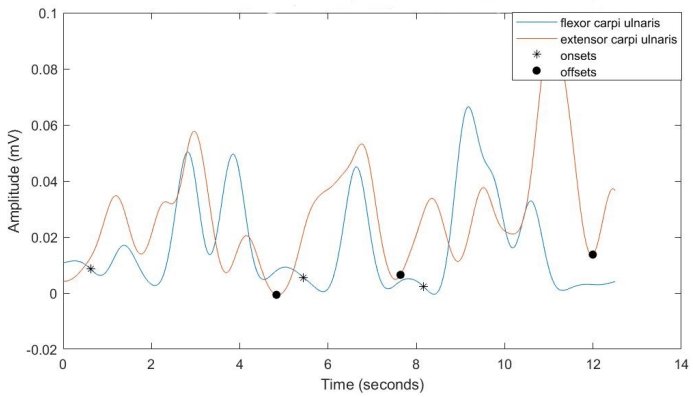


The modified algorithm with the limited search window allowed onset and offset points to be detected for:

- 15 /15 (100%) of elbow flexion–extension trials,
- 15/15 (100%) of pronation–supination trials,
- 13/15 (87.7%) of wrist flexion–extension trials, with the remaining two trials (13.3%) resulting in detection of two out of three repetitions, and
- 14/15 (93.3%) of radial–ulnar deviation trials, with the remaining trial (7.7%) resulting n detection of two out of three repetitions

Overall, the search window-adjusted repetition detector algorithm performed reasonably when compared to visual detection.

## 4.5 Conclusions

In this chapter, an algorithm for detecting motion repetitions using EMG signals was developed. The algorithm was developed based on: the Teager-Kaiser energy operator, the windowed single threshold method, and additional design rules based on the shape of expected motion profiles observed through visual detection. This repetition detector was designed and validated using an existing EMG database consisting of both healthy subjects and those recovering from upper limb

musculoskeletal disorders. The detector was successful for 90.455% of elbow flexion–extension motions, 100% of forearm pronation–supination motions, 97.5% of wrist flexion–extension motions, and 93.75% of ulnar–radial deviation motions. The algorithm was adapted for use with the biosignal acquisition sleeve prototype, described in Chapter 3, to use inertial sensor data to find a search window in which the repetitions occur. With the modification, the detector was found to be: 100% successful for 15 elbow flexion–extension and forearm pronation–supination trials; 87.7% successful and 13.3% partially successful for 15 wrist flexion–extension trials; and, 93.3% successful and 7.7% partially successful for 15 radial–ulnar deviation trials. In conclusion, the developed repetition detection algorithm proved to be suitable for both high efficacy, "gold standard" stationary EMG acquisition systems and low-cost ambulatory EMG acquisitions system.

# Chapter 5

# Development and non-contact electrode for EMG measurement

## 5.1 Introduction

This chapter discusses the development and testing of a non-contact EMG electrode and signal acquisition IC. Currently, discomfort associated with gelled contact electrodes is a major cause of lack of compliance for regimens involving EMG monitoring; to mitigate this, there are many who have developed both dry and non-contact EMG front end modules. This chapter aims to develop a custom EMG front-end module to replace the gelled electrodes used within the biosignal acquisition in Chapters 3 and 4.

Sections 5.2 and 5.3 present a literature review that informs the requirements of the sensor described in Section 5.4. The iterative design and testing process required to create the analog front end of the collection system is described in Section 5.5 and the final design is presented in 5.6.

## 5.2 SENIAM Standards

The Surface Electromyography for the Non-Invasive Assessment of Muscles (SENIAM) project is a concerted action in the Biomedical Health and Research Program of the European Union. The results of this project are often considered to be the gold standard for basic electromyography protocol and processing [65].

### 5.2.1 sEMG sensors

SENIAM's recommendations include criteria that describe the physical sensors used in obtaining electromyographic data. Only bipolar electrodes have been incorporated into the SENIAM study, as the bipolar configuration offers a clear advantage in signal clarity over the monopolar configuration. The introduction of the second electrode placed on the muscle belly allows for differential amplification and thus a higher common mode rejection, eliminating a significant amount of noise from the system.

SENIAM's additional sensor recommendations include: the electrode shape and size of the conductive area, inter-electrode distance, material, and sensor construction. It is recommended that the electrode should not exceed 10 mm in size in the direction of the muscle fibers and that the bipolar electrodes should be located within 20 mm of their respective conductive centers. Small muscles should have an inter-electrode distance less than one quarter of the muscle fiber length to reduce instability in recordings. SENIAM suggests the use of gelled Ag/AgCl electrodes with a fixed inter-electrode distance and fixed cables to avoid motion artefacts.

#### 5.2.1.1 sEMG placement.

The SENIAM project has also made recommendations regarding the placement of the sensors and the procedure to be followed while doing so. First, the skin should be prepared by shaving off hair from the electrode placement site. Then, the skin should be cleaned with alcohol, which should vaporize prior to the sensor placement. SENIAM recommends starting postures specific to the individual muscle measured, as well as the orientation of that body segment; for instance, it is suggested that measurement of the biceps brachii are conducted with the subject seated on a chair with the elbow flexed at a right angle and the dorsal side of the forearm in a horizontal downwards position.

SENIAM recommends that the electrodes be located as a point on a line between two anatomical landmarks, dependent on the specified muscle. Generally, the longitudinal location of the sensor on the muscle is placed halfway between the distal motor endplate zone and the distal tendon. As well, the transversal location of the sensor should be such that the geometric distance of the desired muscle and other muscles is maximized.

## 5.3 EMG noise

### 5.3.1 Electrode–skin interface

The electrode–skin interface is the junction at which the muscle signal is transduced into the differential amplifier as an ohmic potential. For typical gelled contact electrodes, this can be described as an electrochemical process, where typically an oxidation–reduction reaction will result in the charge distribution at the interface. This is known as a half-cell potential, for which the muscle activity's representative voltage is measured with respect to the standard hydrogen electrode. These oxidation–reduction reactions are caused by the dissolution of metallic ions in hydrogel; however, for noncontact electrodes, this half-cell potential is instead replaced by a capacitance characterized by the size of the gap between the electrode and the skin. The remainder of the electrode–skin interface is represented similarly in its circuit model analogue for all types of electrodes (see Section 5.5.2). The electrode–skin interfaces are modeled as layered conductive and capacitive structures, where parallel RC blocks representing different surfaces are connected with one another in series. Generally, one RC block will dominate the response of the junction.

For the gelled contact electrode, there is an RC block for the gel and another for the *stratum corneum*, the outermost layer of the skin, as it acts like a semi-permeable membrane in the presence of an electrolyte. The electrolyte is represented by a series resistor and the parallel layers are ultimately followed by a series resistor as well. This "double time constant model" representation of the interface is essentially a non-linear, inactive second-order filter and is displayed in Figure 5.1. Its behaviour was validated through simulation and testing by Kaczmarek and Webster [66] and Assambo *et al.* [67].

#### 5.3.1.1 Interface noise

Motion artefacts are one way in which EMG data are obscured upon recording. Typically, they occur at the electrode–skin interface when either the muscle moves underneath the skin or a force impulse travels through the muscle and skin beneath the sensor, causing motion at the interface. This results in a voltage recorded of a much higher amplitude than the EMG signal, making it challenging to pick out the desired content. As motion artefacts present as low frequencies in the power spectrum, a high pass filter can be applied in post processing. A corner frequency of 20 Hz is suitable for natural ADLs; however, this may need to be increased for vigorous motions associated

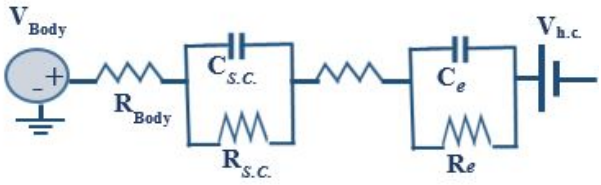


Figure 5.1: Double time constant model of the gelled electrode–skin interface impedance. Here, $V_{Body}$ is the physiological signal voltage, $R_{Body}$ is the resistance within the subcutaneous layers of the skin, $R_{S.C.}$ and $C_{S.C.}$ make up the impedance of the *stratum corneum* layer of the skin, $R_{sweat}$ is resistance resulting from sweat, $R_e$ and $C_e$ make up the impedance of the electrode, and $V_{h.c.}$ is half-cell voltage produced by the redox reaction of the electrode and skin.

with athletics or movement disorders. These artefacts can be mitigated by proper affixation of electrode leads to lateral muscles and avoiding rapid movements.

Cross-talk is another problem inherent in EMG measurements. Visually, this appears as additional content at approximately the same frequencies as the desired signal. This occurs when the electrodes pick up other physiological signals through skin conduction. These signals may be from the heart (ECG) or other muscles. For the former, the amplitude of the cross-talk is expected to be significantly higher and can be resolved by moving electrodes further from the heart. The latter is the result of action potentials from nearby muscles and can be determined via cross-correlation. This can be mitigated by repositioning electrodes (according to the aforementioned SENIAM standards), using double differential amplification to remove the common elements of the signals, and adjusting skin prep, resistance, and ground electrode placement.

### 5.3.2 Intrinsic low-frequency noise

Low frequency noise can be divided into two categories based on their source: intrinsic and extrinsic. Intrinsic noise is from sources within the electrode–skin interface and the circuit components within the signal acquisition electronics; cumulatively, these sources form the baseline noise inherent within the system. These noise sources are more challenging to eliminate than extrinsic sources and are often assumed to exist within the signal during analysis. This baseline noise is problematic where the signal to noise ratio (SNR) is low and the EMGs characteristics are obscured.

Noise developed at the electrode–skin interface, described in Section 5.3.1 is electrochemical in nature. It cannot be defined to fit within a certain frequency range. At the electrode–electrolyte

interface, the noise level varies proportionally to $f_{-n}$, where 0.5<n<1.5, such that the overall effects of noise decrease at higher frequency signal content. This noise presents itself as fluctuations in electrical potential at the interfaces. In gelled contact electrodes, this can be partially attributed to instability in the fluid film under constant current. Generally, this may also be caused by some small ionic discharges at the electrode surface as a result of material impurities. The other baseline noise component is the instrumentation noise and is inherently developed in the electrodes, wire leads, and all resistive circuit components required for amplification. This noise is the result of random electron fluctuation and cannot be eliminated; however, the severity of its effects on the signal quality can be controlled through careful circuit design and components selection. In the observed frequency range, the power spectrum representation of this noise is given as the product of Boltzmann′s constant, the operating temperature, and the component's resistance value. Its behaviour resembles white noise and is cumulative throughout the system [68].

### 5.3.3 Extrinsic low-frequency noise.

Conversely, extrinsic electrical noise is created by sources associated with the environment and experimental setup. The most common extrinsic noise source is power line interference, which exists in the presence of AC power sources at 60 Hz based on North American standards. This may be removed through the implementation of a notch filter at that frequency. Similarly, the system may be affected by nearby motors, phone lines, ethernet cables, and radio waves; however, the power spectrum characteristics of these sources are known and can be accounted for in the design. Another significant extrinsic noise source is the cable motion artefact. Cables between the electrode and the acquisition system that are not well secured may cause additional noise, typically under 10 Hz, caused by swinging motion and poor shielding. DC offsets can also be caused by telemetry and removed through the use of a high pass filter at 5–10 Hz.

Many of these problems can be mitigated by using the system away from fluorescent light bulbs, rooms lined with conductive materials, and large electrical machinery; keeping cables short and braided; properly shielding cables; using pre-amplified electrodes; and ensuring that electrodes are grounded to an electrically neutral location [69].

## 5.4 Existing types of electrodes

Electrodes used for EMG acquisition can be described in terms of their configuration, arrangement, and their construction. As described above in Section 5.2, electrodes may have a monopolar or bipolar configuration, such that either one or two electrodes, respectively, are placed over the muscle belly. The bipolar configuration removes the component common to both electrodes before comparing it to the reference electrode while the monopolar configuration has no such mechanism.

Although SENIAM recommended the use of gelled contact-based electrodes in 1999, technologies have since emerged that provide reliable alternatives to these sensors in physiological recording. Though mainly used in applications where the expected power spectrum occurs at lower frequencies, dry contact and non-contact electrodes have become more commonplace as further research has been conducted. The next section acts as a literature review on the subject, drawing from publications found via Google Scholar and Western University's library services between February and June 2016.

### 5.4.1 Gelled contact electrodes

Contact gelled electrodes are considered to be the gold standard for EMG signal recording due to their electro-mechanical stability and the quality of the signal obtained. They consist of a metal electrode, typically Ag/AgCl, acting as the conductor and a hydrogel used as an interface between the conductor and the skin. The hydrogel provides an explicit ohmic dielectric where oxidative and reductive chemical reactions occur. This allows current to easily pass from the muscle to the conductor by lowering the interface impedance; thus, reducing the amount of noise observed in the signal. Sometimes, additional abrasion of the *stratum corneum* is required to further reduce the skin's impedance to obtain a better signal.

The hydrogel also ensures that the electrode properly adheres to the arm, preventing sensor movement and motion artefacts. This makes them suitable for long term measurements from a signal quality perspective; however, the use of gel requires significant preparation time and may cause some discomfort or irritation. They may feel somewhat obtrusive to the user and cannot easily be incorporated into a wearable device.

These contact gelled electrodes are low costs, come in a variety of shapes and sizes, and can be either reusable or disposable. Their noise and impedance characteristics have been widely studied;

subsequently, the processing required to obtain meaningful data is well understood [71].

### 5.4.2 Dry contact electrodes.

Although the skin provides significant resistance between the electrode and the action potential signals, conventional electrode gel is not the only way to introduce conduction into the system. Dry electrodes do not have an explicit electrolyte; however, the same results are achieved through the conductive qualities of the skin's natural moisture or by penetrating the *stratum corneum* to bypass this resistance. Often, these are used in locations where using gel would be a challenge, such as EEG application, decreasing the subject's preparation time and discomfort.

Dry contact electrodes that preform comparably to gelled electrodes can be fabricated from conductive materials, an active electrode circuit, and an on-site instrumentation amplifier. This has been demonstrated in studies such as Valchinov's that obtains signals from flat metal discs in contact with the skin. Flexible conductive materials can also act as electrodes, such as rubber, fabric, and foam. These materials conform more easily to the skin, increasing the comfort and contact area of the sensor, reducing problems with stability observed within similar metal electrodes. Still, all of these electrodes may not be reliable for long term use due to the increased impedance within the skin–electrode interface and motion artefacts due to lack of adhesion [71] .

In order to mitigate the issues surrounding adhesion without relying on any sort of hydration, small fabricated needles may be used to slightly pierce the outer layer of the *stratum corneum*. These needles can be on the nanometer, micrometer, or millimeter scale and are made from materials such as silicon or carbon and are typically coated with an inert metal.

Ruffini's research involves the use of fabricated silicon microneedles arranged in $3\times3$ $mm^2$ arrays to record EEG signals. That person used multi-walled carbon nanotubes, each with a diameter of 50 nanometers and a length of 15 micrometers. The needles were arranged in $4\times4$ microtip arrays on silicon substrates with an indium oxide coating, which allows the electrodes to maintain a high charge delivery capacity and low constant impedance over the desired frequency range.

Ghafar-Zadeh created 20-$\times$20 MEMS microprobe arrays coated with Ti/Pt that improved the observed signal intensity and electrode–skin impedance. These dry electrodes are considered to be somewhat invasive; subsequently, their comfort, safety, and hygiene should be further studied. The small needles were also fragile and longer spikes are susceptible to breakage. This results in

an impedance mismatch between the differential measurements, which decreases the signal quality and stability. [73]. Forvi has mitigated this concern and has developed sensors with low electrode impedance, fewer artefacts, and a quick set up to be used for long term recording; however, these are expensive to produce and still invasive [74].

To reduce the intrusiveness of dry contact electrodes, other researchers have developed sensors with 'tips' or finger-like structures. These are often fabricated on a centimeter scale and are around the size of a five cent coin. In 2008, Matthews *et al.* designed an EEG sensor with a 10 MΩ contact impedance between the scalp and tips, which are arranged in two concentric rings to improve common mode rejection [85]. A new design was released in a 2011 publication, in which a flexible, low-cost electrode was made from polymer silver-coated bristles. Both of these designs required the tips to be re-coated to avoid impedance mismatches. In comparison to the needle fabrications, the implementation of fingers reduced invasiveness and risk of infection; however, the impedance was dependent on the amount of pressure they applied making them uncomfortable for long-term use.

In order to facilitate attachment without the force or pain, Liao developed a dry EEG sensor with 17 spring contact probes. This ensured high geometric conformity between the sensor and surfaces, and the maintenance of low electrode impedance [75]. It was later improved upon by changing the geometry of the probes and using a more flexible silicone-based material [76]. Similarly, Salvo designed a non-invasive millimeter scale design with 80 conical 3-D printed needles coated with titanium and gold. These designs still risk prevalence of motion artefacts due to lack of abrasion or secured attachment at the interface [77].

### 5.4.3 Non-contact and fabric electrodes

Alternatively, dry electrodes can be fabricated where there is no ohmic contact with the skin; instead, the sensor can be embedded within material. Here, the capacitance developed at the gap between the insulating layer, the skin, and the electrode forms the interface. The simplified model of the electrode–skin interface described in Section 5.3.1 can be extended to include a parallel R-C block representing the resistive and capacitive properties of the skin and the intermediate materials. This type of fabrication is advantageous in user compliance, as it can be incorporated directly into the wearable device, does not cause discomfort, requires minimum preparation time, and is impervious to the skin's condition.

Though they are ultimately more user-friendly, there are numerous challenges in the design of non-contact capacitive electrodes that ultimately have limited their commercial availability. Firstly, there is often much more noise at the electrode interface and low electromechanical stability. This is because there is no explicit electrolyte; instead, there is another layer of material that will not act as a perfect dielectric but instead will add additional impedances, typically dominated by the resistive component, which can significantly reduce signal quality. The various layers of materials add increased complexity to modeling the coupling between the electrode and the skin due to the relationship between the resulting conductances and capacitances. Also, the lack of contact makes these electrodes much more prone to displacement and thus motion artefacts.

These challenges can be somewhat mitigated through careful design of the electrode module. The criteria used here to characterize the design of a non-contact electrode are as follows:

1. **Electrode type:** Describes the type of electrode used.
2. **Analog front end (AFE):** The amplification method used to collect signals.
3. **DC bias path:** Circuitry used, if any, to bias the signal for input to the AFE.
4. **Guarding:** Method used, if any, to provide shielding from external noise.
5. **Active reference:** Type, if any, of active reference used within the acquisition module.
6. **Purpose:** Type of physiological signal the module is intended to collect.

Tables 5.1 and 5.2 compares these criteria amongst existing EMG acquisition module design.

Through the examination of the characteristics of existing electrodes, commonalities and well-tested methods can be determined. This provides insights into proven factors that are incorporated into the design presented later in this chapter. As well, it is notable that the majority of existing works are directed towards collecting physiological signals from the heart and brain, EKG and EEG respectively; thus, it appears as though non-contact electrodes tailored towards EMG is a less explored field facing different challenges.

## 5.5 EMG Module Specifications

With knowledge of existing non-contact EMG signal collection modules as well as an understanding of the goals at hand, specifications and requirements for the development of a custom module can

Table 5.1: Comparison of existing non-contact and fabric electrode module designs

| Module Design | Type | AFE | DC Bias Path | Guarding | Active Reference | Purpose |
|---|---|---|---|---|---|---|
| Chi [80] | EEG/ECG | Two LMP7702 op-amps | None (floating signal point to avoid amplifier saturation, resultant DC offset removed with HPF) | Active shielding via inner PCB plane, driving negative input | Electrode near base unit provides common voltage via daisy chain, buffered through distributed sensor network | — |
| Chi [80] | EEG/ECG | INA116 (Brown-Burr) | None (floating signal point to avoid amplifier saturation) | Active shielding via inner PCB plane, driving negative input | Electrode near base unit provides common voltage via daisy chain, buffered through distributed sensor network | – |
| Chi [70] | EEG/ECG | LMP2207 op-amps | Reverse current diodes | One op amp used as buffer to drive active shield | Common reference created through difference between amplified | filtered signal and average across network |
| Hazrati [81] | EEG | LTC6079 op-amp | Unspecified bias circuit between non-inverting input and guard | Active shielding via PCB driven by signal from biased sensor signal | Driven right leg electrode | Design of a BCI to directly connect to external device without a PC |
| Lee [82] | EEG | OPA124 op-amp sensing electrodes, amplified by INA118 in-amp | 5 GΩ resistor combined with textile impedance | Guarding feedback from OPA124 drives conductive fabric shield | Driven right leg electrode with stabilizing foam surface | Wearable band for mobile ECG measurement |
| Gourmelon [83] | EMG | Unspecified op-amp | Not stated | Shielding via guard ring driven by unity gain buffer amplifier | Uses bipolar configuration, differential signal obtained digitally | Collects EMG signals from *biceps brachii* through cotton t-shirt |
| Sullivan [84] | EEG/ECG | INA116 (Brown-Burr) | Reset circuit consisting of two transistors and two resistors | Guard ring and shielding metal plate driven by positive input pin following reset | None | Use of non-contact physiological sensor reading n lab environment (scalp and chest) |
| Matthews [85] | EEG/ECG | Not stated; assumed to be INA116 based on noise characteristics | Matched resistor bias path | Active shield via PCB design | None, referenced to other sensors in study | QUASAR project; ECG signals obtained via elastic inside cotton t-shirt |
| Sun [86] | EMG | INA116 (Brown-Burr) | 1014 Ω bias path, based on calculation | Active guard ring | None | Driver health and fatigue monitoring |

Table 5.2: Comparison of existing non-contact and fabric electrode module designs – 2

| | | | | | | |
|---|---|---|---|---|---|---|
| Svard [87] | EEG/ECG | INA116 (Brown-Burr) | 10 GΩ resistor bias path | Active shielding via a metal layer within the PCB design | None | Unspecified |
| Yang [89] | ECG | INA116 (Brown-Burr) | Reverse current diodes | Active shield via PCB design | Driven right leg reference electrode | Development of a capacitively coupled wearable ECG system to be used in conjunction with a SSA recovery algorithm |
| Lin [90] | ECG | Unspecified op-amp | Reverse current diodes and resistor network | Active shield via PCB design | Unspecified | Development of non-contact electrodes for real-time, mobile ECG monitor |
| Prance [91] | General | Reverse current diodes | - | - | - | Unspecified |
| Kim, Lim, and Kwang [90] | EEG | None | None | Passive shielding through layered copper, urethane, and conductive fabric | Unspecified | Long-term EEG measurement |
| Linz [92] | EMG | Unspecified | Unspecified | Guard cap created from layering capacative embroidery and PCB design | None | EMG integrated within garments for wearable health monitoring |
| Komensky [88] | ECG | Ultra-high impedance op-amp | two anti-parallel diodes | Active shield via PCB design | None | Long-term at-home cardiac monitoring |

be outlined, as follows:.

- In accordance to SENIAM standards, each channel must have a bipolar configuration.
- As human muscle active potential signals range between 5 and 500 Hz, each channel must be able to sample at least at a rate fulfilling the Nyquist criteria (1 kHz).
- There must be very low noise in the acquisition system, to ensure this:

  the AFE amplifier must have a very large input impedance,

  the AFE components should have a CMRR larger than 90,

  the AFE minimizes the input current noise per root Hz at 1 Hz; ideally, this would be less than 1 fA.

After reviewing the literature, it was decided that signals would not be processed in real time, as the biosignal acquisition sleeve it is intended to be incorporated within does not display data in real time. This also allows for a great reduction in the cost, size, and complexity of the module. The filtration of the EMG signal can be performed digitally, as speed is no longer a concern. At minimum, four analog filtering stages can be omitted from the hardware design. The risk of aliasing the desired signal content is also minimized, providing the selected parts minimize noise and are recorded at a high resolution.

As this module is intended to fit within the biosignal acquisition sleeve described in the previous chapter, considerations must be taken to ensure compatibility. The analog signal output from the module must be able to be input into the sleeve's ADS1292 IC in order to become digitized and travel along the SPI bus. To do so, there should be output pins from the analog front end circuitry with male-type connectors. The use of the existing ADC set up negates the need for each module to have an active reference, as the sleeve's ADC is able to create a single reference to eliminate common mode noise created at the interface. To keep the sleeve's circuitry viable for modularity, this EMG module should not require additional connections to either the ADC or other power sources that do not already exist within the system, or they must be easily amendable from a user′s perspective. The module must be able to operate on a 3.3 V or +/- 5 V power supply, like the other devices to be used in the SPI bus within the sleeve, or incorporate another logic level shifter.

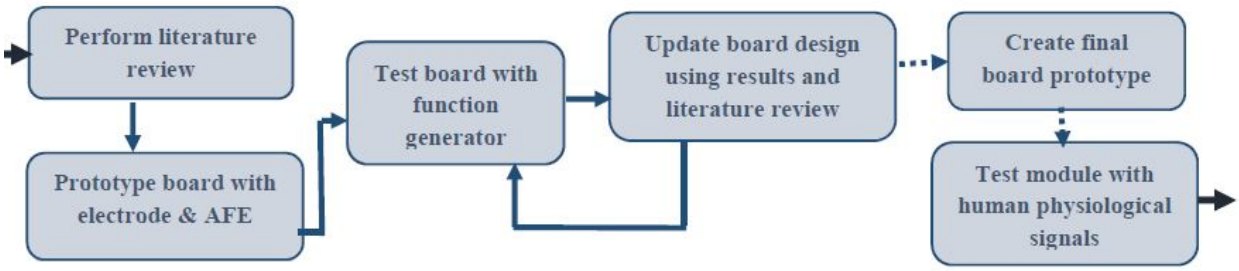


Figure 5.2: Flow chart describing the design process of the EMG acquisition module.

One of the main goals of this chapter is to develop a method for acquiring EMG signals in a manner that is comfortable for the user, likely increasing adherence. The module is intended to be non-contact in order to mitigate discomfort associated with the use of a hydrogel. Removing contact with the skin will prevent possible irritation during long-term use. As well, set-up time and artefacts caused by poor sensor placement will be reduced. The pressure placed upon the skin by the module will be even and the module should be operable when enveloped by soft textiles when integrated into the sleeve.

### 5.5.1 Design process of the non-contact EMG module

The design of the EMG collection module became an iterative process after acknowledging the fickle nature of both the desired signal and the sensitivity of some of the electronic components; as well, some key characteristics of the design, such as guarding, cannot be simulated. As a result, many partial prototypes were constructed in order to inform the subsequent iterations. The design's shortcomings and their possible solutions were addressed using aspects of existing designs, as outlined in 5.2. Initially, a board was fabricated with just the layers making up the electrode and a place to surface mount the basis of the AFE. The signal produced through this board was tested with a microcontroller's ADC, the results were analyzed, and the appropriate additional guarding or biasing techniques were compared and used to inform the design of the next board. This process was repeated.

The foundation of a non-contact electrode design has been described similarly by Matthews [85], Hazrati [81], and Prance [91]. An adaptation of this description cis shown in Figure 5.3. The structure consists of a dielectric interface between the biopotential signal and an adjacent sensing plate for collection. This plate is connected to amplification circuitry via the analog front end. A

bias circuit may be introduced if necessary to prevent amplifier saturation, and connected to the non-inverting terminal of the AFE. All of this should be encapsulated by a guard. Neutralization circuitry may be added between the output and non-inverting input if necessary, to accommodate for changes in capacitance due to varying distances between the dielectric and the electrode.

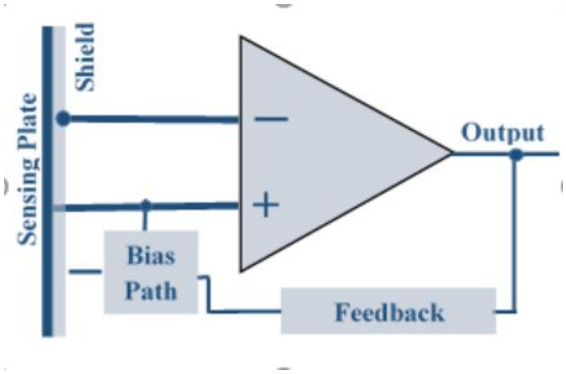


Figure 5.3: Generalized non-contact biopotential electrode structure.

### 5.5.2 Interface of the non-contact electrode.

In addition to the basis of the analog front end of the non-contact electrode, a basic model of the electrode interface is also known. Typically, this is modeled as layered conductive and capacitive structures, where parallel RC blocks representing different surfaces are connected with one another in series. The R—C blocks within the model is as follows:

1. the *stratum corneum*, encompassing the signal deterioration between the action potential of the muscle and the outermost layer of the skin, which acts as a semi-permeable membrane,
2. the intermediate insulating material, and
3. the gap between the skin and the bioamplifier, encompassing the capacitance characterized by the thickness of the electrode.

The analogous circuit model is displayed in Figure 5.4:

Mathematically, the impedance of the electrode–skin interface is represented as follows:

$$Z = R_{body} + \frac{1}{\frac{1}{R_{S.C.}} + j\omega C_{S.C.}} + \frac{1}{\frac{1}{R_{insulator}} + j\omega C_{insulator}} + \frac{1}{j\omega C_d} \tag{5.1}$$

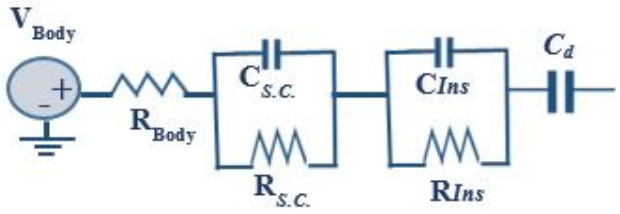


Figure 5.4: Circuit model of the body–non-contact electrode–skin interface. Here, $V_{Body}$ is the physiological signal voltage, $R_{Body}$ is the resistance within the subcutaneous layers of the skin, $R_{S.C.}$ and $C_{S.C.}$ make up the impedance of the *stratum corneum* layer of the skin, $R_{S.C.}$ and $C_{S.C.}$ make up the impedance of the insulator, and $C_d$ is the capacitance of the electrode.

Figure 5.5 (A) displays a representative schematic of the impedance from the skin–electrode–AFE model. It is to note that the term $C_d$ is the capacitance generated at the electrode. The value of $C_d$ is dictated by the following equation:

$$C_{electrode} = \frac{\epsilon_0 \epsilon_R A}{d}. \tag{5.2}$$

In this equation, $\epsilon_0$ is the value of permittivity in a vacuum, roughly $8.854187 \cdot 10^{-12} F \cdot m^{-1}$, $\epsilon_r$ is the relative permittivity of the insulator, A is the area of the electrode, and d is the insulator's thickness. Taheri *et al.* [106] determined that the capacitive component of skin impedance was 15 nF at 10 kHz, and that the capacitive electrodes function optimally where their capacitance is two orders of magnitude smaller.

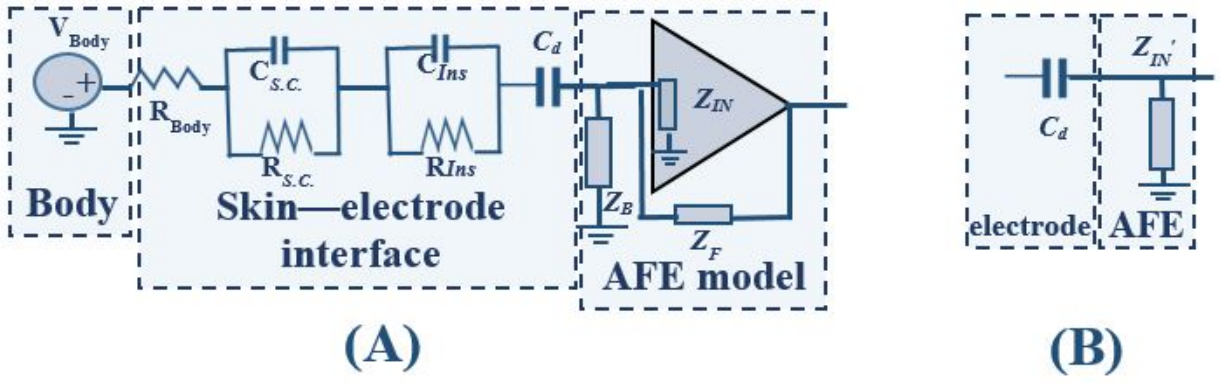


Figure 5.5: Circuit model of the dielectric–skin interface and AFE impedance. (A) Representative model of the impedance of the body, skin–electrode interface, and AFE. (B) Simplified model of the electrode–AFE interface, indicating behaviour of a high-pass filter.

The electrode–AFE interface impedance model can be further simplified as a high pass filter, as shown in Figure 5.5 (B). The pseudo-filter's behaviour is determined by the value of $C_d$ and the effective impedance of the AFE, $Z'_{IN}$ or $R'_{IN}$. The electrode and AFE should be designed such that the cut-off frequency of the filter, $f = 1/2\pi R'_{IN} C_d$ , does not eliminate frequencies of interest; here, the value of $f$ should not exceed 1 Hz.

## 5.6 First iteration of the partial prototype of the EMG module

The first iteration of the electrode design can be constructed once the two major components have been established. The first component is the electrode itself, which is a multi-layer PCB design consisting of various materials in order to create a dielectric interface and isolate the desired signal. This design is informed by basic properties of materials, understanding of capacitive sensing, and existing works in this field. The second component is the selection of suitable analog front end circuitry. Following the design and AFE selection, CAD software was used to design a PCB, which was later fabricated and tested.

### 5.6.1 Electrode design

As discussed above, the electrode itself transduces the body ionic current into a standard electrical current. Any conductor can be used to fabricate a sensing plate of a dry electrode; however, simply using a metallic plate neglects the imperfections of the system. Due to the need for high-precision instrumentation to obtain the EMG signals, the electrode must also be designed, with the AFE in mind, to mitigate distortion. Figure 5.6 illustrates a profile view of the non-contact electrode design.

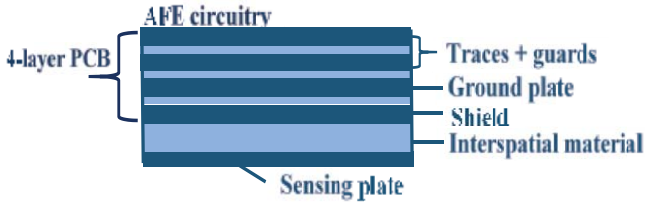


Figure 5.6: Profile view of the non-contact electrode design.

In published works, the entire prototype, including the AFE, was directly printed using copper

and solder mask as the conductive and insulating materials respectively. Here, this is not feasible due to the guarding required for the selected components, as most manufacturers will not support boards with more than four layers. The selected AFE requires copper-filled guards incorporated onto both the top and bottom layer of the circuit board to prevent current leakage and noise better; thus, the ground plane needs to be a separate layer.

As well, a shield layer is incorporated, which is driven by the feedback of the AFE to ensure that the same voltage potential exists at the shield and at the positive input. Through this technique, the capacitance between the shield and the core is effectively minimized; resultantly, the noise due to environmental interferences, parasitics, temperature effects, and motion artifacts are reduced. Input impedance into the AFE will also be increased, resulting in improved signal quality.

The materials selected must not be susceptible to triboelectric effects nor should they have high susceptibility to noise. Copper and solder mask fulfill this criteria and can be incorporated into a printed PCB structure design; however, as mentioned above, other materials must also be used due to manufacturing limitations. The interspatial material must be an insulator that provides a fixed distance between the sensing and the shielding plates. Ideally, it would not change in thickness, as that would alter the capacitance, but still be able to maintain constant contact with both plates. Lee *et al.*'s work experimentally indicates that urethane rubber proved to be a suitable option [82]. In order to eliminate free space between the plates, the rubber was molded and adhered to both plates. This, along with the low dielectric constant reduces the unwanted capacitances developed within the sensor.

To fulfill this criteria, a customizable rubber-like substance was selected. Using the Objet260 Connex 3-D printer, a composite of Objet's Tango and Vero materials was created with a Shore hardness of 50 A, which is approximately the hardness of a pencil's eraser. It allows for the module to be somewhat flexible and form to the garment instead of contributing to a motion artifact. As well, the concern regarding stray capacitance due to free space is eliminated due to negligible shrinking. The sensing plate must be made of a conductor. For simplicity and consistency, copper has been chosen; however, unlike the printed PCB layers, milled copper plates were not be used. In order to reduce costs and ease the process of manual fabrication, 3M's copper tape was used.

#### 5.6.1.1 Analog front end selection

The type of AFE selected within this design is the instrumentation amplifier. Amongst physiological signal acquisition modules, this is a popular choice due to the nature of these ICs. A three op-amp instrumentation amplifier topology contains two general stages: first, two signals are input into two separate buffer amplifiers; afterwards, the two signals are fed into another op-amp for differentiation. The buffers reduce the impedance of the acquired signals, matching it to the next stage.

The AFE selected here is Brown-Burr's INA116. This medical-grade device is typically used for biopotential amplification due to its ultra-low input bias current and noise design. The IC has a 3 op-amp topology, in which the first two amplifiers collect signals before they are differentiated by the third. A schematic of the INA116 is shown in Figure 5.7.

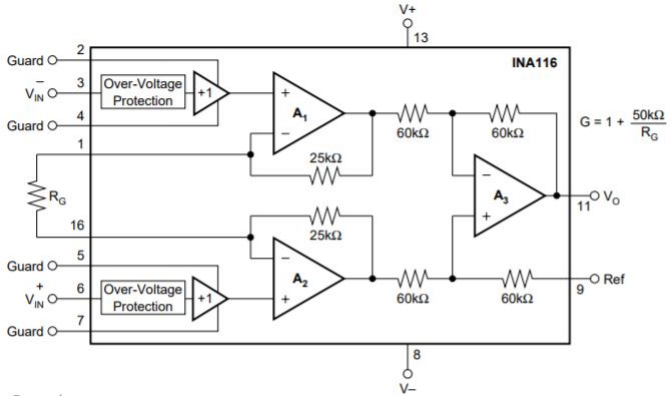


Figure 5.7: Schematic of Brown-Burr's INA116 instrumentation amplifier, from Texas Instruments

The inverting inputs of both first stage amplifiers are tied together, such that a single resistor can be used to control the in-amp's gain. The non-inverting inputs of both first stage amplifiers are designed to minimize noise associated with the bias current. To do so, guard pins are placed around both inputs to eliminate bias currents from coupling with the signal, thus distorting it. As well, these inputs also contain unity gain buffers, which functions as a voltage follower; since this ensures that little current is drawn, it also reduces the associated current noise. As indicated in Section 5.4.3 above, this technique is commonly used in existing designs. Having it included within the AFE IC reduces the need for more complex designs and reduces the required circuitry.

In addition to providing some of the necessary guarding for a low-noise biopotential acquisition module, the INA116 also fulfills the AFE criteria described in Section 5.5. Table 5.3 uses this

Table 5.3: Specifications of the non-contact electrode's AFE.

| Criteria | INA116 | Requirement |
|---|---|---|
| CMR | 84 dB at G=10 | $> 90$ dB |
| Input impedance | $10^{15}$ Ω | $10^9$ |
| Input current noise | 0.1 fA/$\sqrt{A}$ | 1 fA/$\sqrt{A}$ |

knowledge and compares the specifications of the chosen in-amp to the desired values to ensure sufficiency.

#### 5.6.1.2 First prototype board design

The first board constructed and tested incorporates the non-contact electrode design and interface, as well as the INA116. CadSoft's EAGLE 7.6.0 Professional CAD software was used to design the printed circuit board, which was then fabricated.

The acquisition circuitry is designed using the generalized diagram from 5.5.1 and the INA116. The positive input pin is connected to the sensing plate and receives feedback from the unguarded output of the instrumentation amplifier. A pair of header pins are placed within the feedback loop to allow for testing of neutralization circuitry, which would stabilize the amplifier gain across coupling distances, and between the positive input and guard pins, to examine the effects of bias circuitry. The guard pins of the positive input are connected to the shield layer of the electrode. The negative input receives feedback from the guarded output, and its guard pins are also connected to the shield layer. The schematic is displayed in Figure 5.8.

The board consists of alternating layers of copper and solder mask, with the former acting as the sensing plate, grounding plate, and shield, while the latter provides isolation. The board dimensions are 0.93 inches by 1.25 inches. Table 5.9 describes the various layers of the board, their purposes, and thickness. The board was fabricated by OshPark Ltd, in Lake Oswego, Oregon, USA.

In Figure 5.9, the leftmost image is the top layer, Layer 1, which will lie furthest away from the skin. It contains the electronic components, some traces, and copper-filled guards surrounding the input pins of the INA116. The layer adjacent is Layer 2, the bottom of the first layer. It contains additional traces and copper guards surrounding the input pins and the non-neutralizing feedback, connecting to the shield layer. To the right, Layer 15 is a copper-filled ground plate and

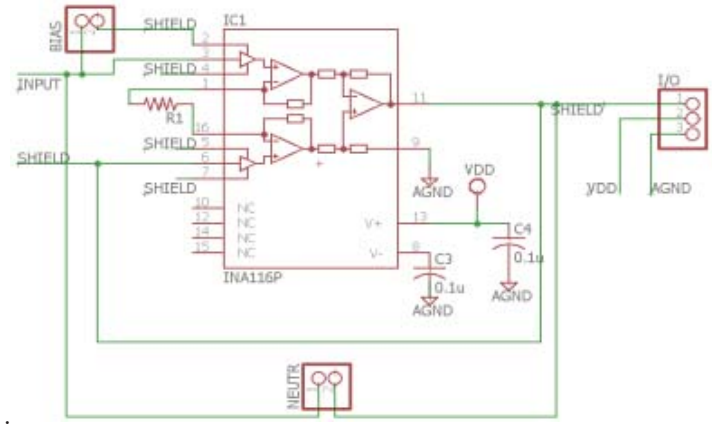


Figure 5.8: Schematic of the first electrode prototype.

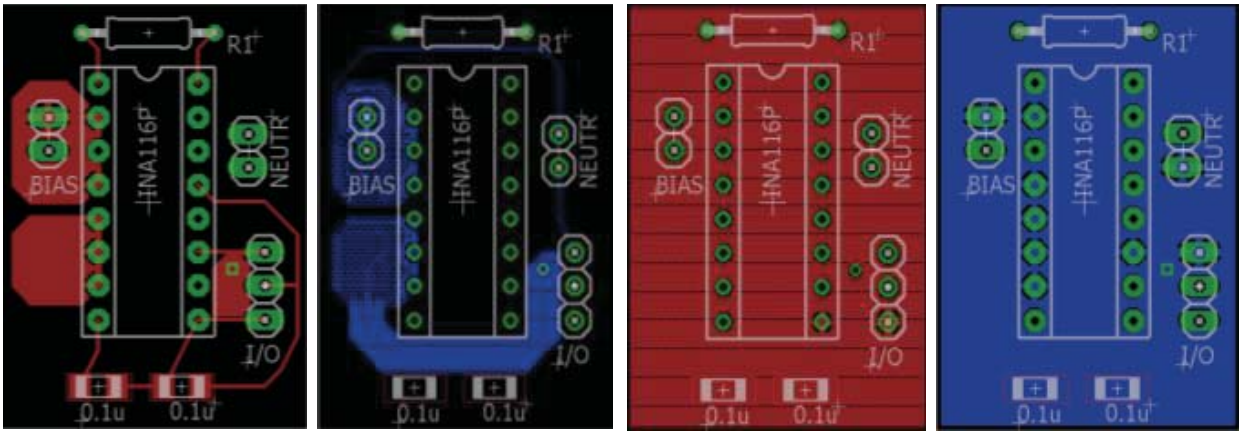


Figure 5.9: Four layer printed circuit board of the initial sensor prototype. From left: Layer 1, AFE electronics, traces, input guards; Layer 2, traces, input and feedback guards; Layer 15, filled ground plate; Layer 16, internal shield plate.

Layer 16 is a solid copper shield plate.

#### 5.6.1.3 First prototype fabrication

Of the initial prototype, the printed component accounts for all but the sensing plate and the interspatial material between the former and the shield plate. This part of the fabrication process was completed manually using the additional materials described earlier.

Given the dimensions of the electrode PCB, a rectangle with the same surface area as the board, 1.1625 $in^2$, and a thickness of 1 cm was designed in SolidWorks. The structure was printed using the Objet260 Connex 3-D printer with a combination of Tango (rubber-like) and Vero (rigid)

materials. By 3-D printing the interspatial plate instead of molding it, consistency and accuracy of the desired shape, size, and finish can be ensured. The rubber-like layer is adhered directly to the PCB using Gorilla Glue, eliminating variable space in which stray capacitance may vary.


**(A)** **(B)** **(C)**

Figure 5.10: Fabrication of the electrode test module. (A) Soldering of the in-amp, bypass capacitors, and headers to the PCB. (B) Adhering the printed rubber composite to the PCB. (C) Adhering the 3M copper tape and snap to the module.

Afterwards, the sensing plate was attached on top of the interspatial material. Copper tape by 3M was used, as it is a solution that is inexpensive, simple to implement, and results in the desired properties. The tape iwas negligibly thick and can be placed flush onto the printed rubber-like layer without any additional adhesive. As well, the snap used to connect to the physical structure of the sleeve, is incorporated without interfering with the contact between the sensing plate and the fabric dielectric interface.

### 5.6.2 Electrode iteration 2

Through basic bench-top testing, it was determined that the described electrode module did not function as desired: the amplifier would attenuate an input signal due to improper power supplies and a short circuit was created through the board layout. In order to test the proof-of-concept design, another test module was fabricated. This version has a number of key differences from the printed module:

1. The negative feedback between the shield and the output was omitted.

2. The materials used were different and more connections were made manually.

3. The module is powered by a dual power supply with a +/- 5 V rail.

To fabricate this module, the bottom two layers remained the same: the sensing plate was a piece of 3M copper tape and the interspatial layer was the 3-D printed Tango rectangle. As the inner shield plate, another piece of copper tape was used. A tab was left such that it was accessible to other connections. A single layer of copper-fill from an existing layer was glued on top of the structure as a ground plate. The top-most layer was created using a piece of vector board. This contained the INA116 amplifier, the bypass capacitors, a jumper for neutralization circuitry, and the other electrical connections.

The connection between the positive input terminal and the sensing plate was created by soldering a wire from the vector board to the bottom-most layer of the copper tape. Similarly, the shielded components were all connected together at a node on the vector board and a wire was soldered between the node and the copper tape tab of the shield layer. For the bias circuitry connection location, wires were soldered to both pieces of copper tape without other connections.

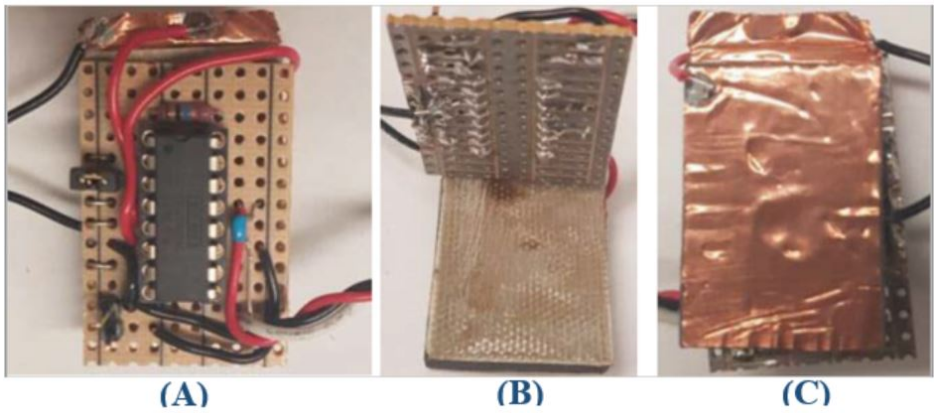


Figure 5.11: Electrode module re-design. (A) Top layer with electronics, INA116, and visible shield. (B) Ground plate and interspatial material. (C) Sensing plate and its connections, shielding plate.

Figures 5.11 and 5.12 show the fabricated module's structure and connections. The left-most image shows the vector-board with the instrumentation amplifier and other electronic components and connections. The shield layer tape tab can be seen, as can the connection between it and the negative input. The middle image contains the lifted vector-board, under which the soldered

connections can be seen, and the single layer circuit board that acts as a ground plate. The Tango interspatial material below the ground plate is also visible. Finally, the right-most image displays the copper tape sensing plate, the wire connecting this to the positive input and bias, and the shield tape tab. When connected to a +/- 5 V power supply, the effects of the capacitive contact could be observed through an oscilloscope, verifying some initial success of the module.

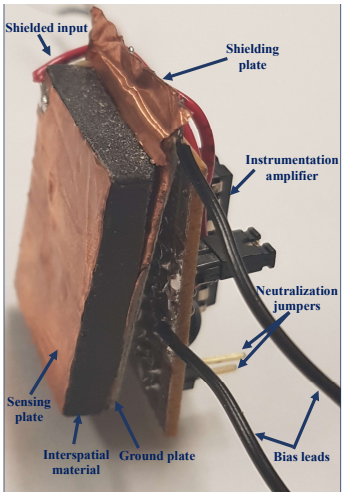


Figure 5.12: Opened up profile view of the electrode module and all of its materials, features, and components..

### 5.6.3 Bench-top testing of the prototype

Following the construction of the electrode test module, twelve basic configurations underwent bench-top testing. The objective of the bench testing is to validate the functionality of the AFE and the ability of the electrode to pick up signals administered via a conductive fabric test pad. This allows for the comparison of accuracy and drift among different circuit configurations with a known applied signal. The bench-top tests were run as a repeated measurement study with two factor, bias and feedback, with four and three levels, respectively. It was expected that the results would indicate that a particular circuitry combination would result in more accurate, less noisy readings of a fixed, known voltage signal.

The test pad used for the bench-top testing setup is fabricated with the conductive fabric incorporated into the final design of the biosignal acquisition sleeve. A male snap was attached through the center of the fabric patch to receive the electrode module. A piece of wire was soldered to the edge of the conductive fabric such that the intended signal exists within it for observation.

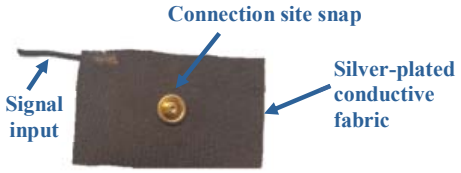


Figure 5.13: Test-pad used to transmit a known signal to the electrode module.

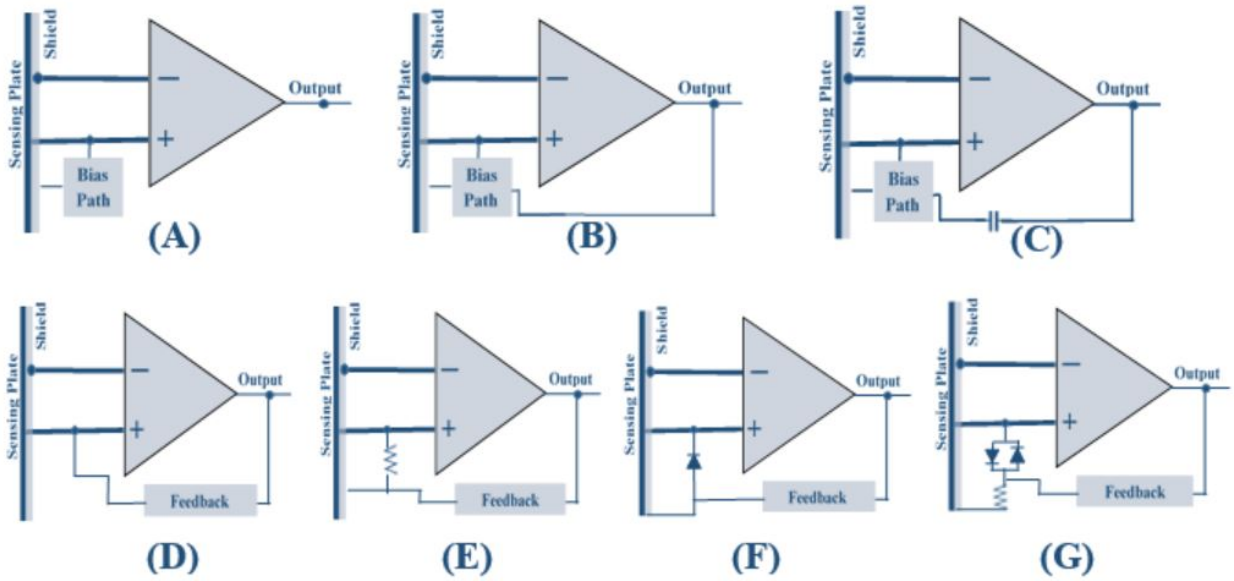


Figure 5.14: Schematic representation of non-contact electrode configurations used in the test-bench analysis.

The nine basic test-configurations are displayed in Figure 5.14. There are three different feedback configurations and four bias path configurations of the electrode module, with the top row displaying the former and the bottom row displaying the latter. (A) shows a set-up without any positive feedback. (B) shows basic positive feedback used to bootstrap the biasing element, increasing the effective input impedance and thus the signal stability. (C) introduces some capacitance into the positive feedback, used to match the anticipated changes due to mechanical movement of the module. The feedback is still expected to increase the effective input impedance.

Figures (D), (E), (F), and (G) reflect four different biasing techniques that are tested. The first configuration uses no biasing whatsoever; instead it relies on a floating input. (E) uses a grounded bias resistor in the giga-ohm level of magnitude, (F) uses a reverse-current diode, and (G) uses a back-to-back diode pair and a load resistor to keep the voltage input levels within the device-

specified range. For the test-bench series, each feedback technique was tested in combination with each bias technique; thus, there are twelve unique configurations to be assessed.

#### 5.6.3.1 Experimental set-up

The experimental set-up of the bench-top testing is shown in Figures 5.15 and 5.16. The fabricated electrode module had a gain resistor of 1 GΩ such that the gain of the amplifier was approximately unity. The module was connected to the conductive fabric test-pad through the snap, which received a signal through an alligator clip from the signal generator.

The electrode module received its +/- 5 V power from the BK Precision 1871A DC regulated power supply. Jumper wires were used to attach the feedback and bias headers to the breadboard, allowing for the circuit configurations to be easily changed.

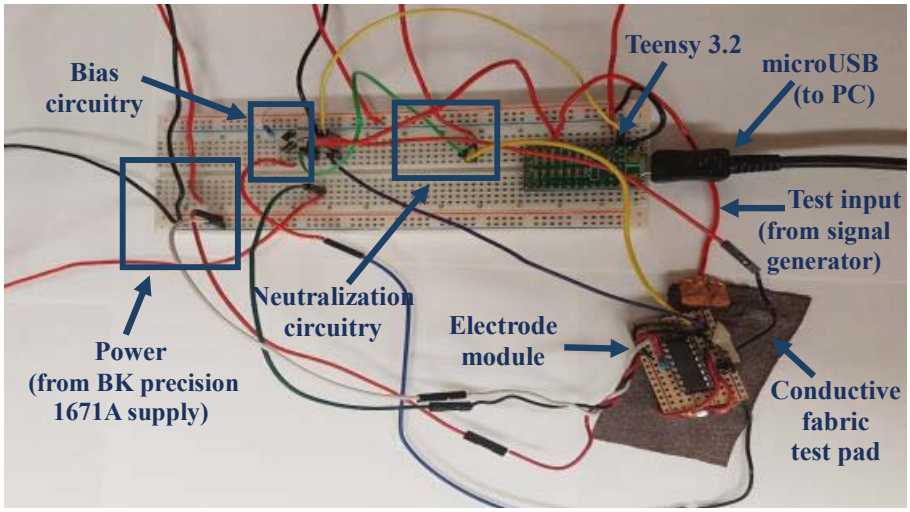


Figure 5.15: Experimental setup of the bench top testing for the non-contact electrode module.

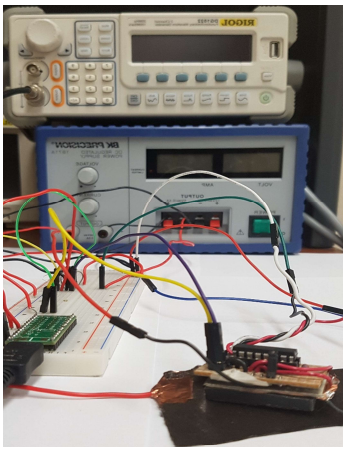

Figure 5.16: Experimental setup of the bench top testing for the non-contact electrode module, showing the signal generator and power source.

The output signal from the electrode bias was read by the Teensy 3.2 through one of the analog-compatible pins. The other Teensy 16-bit analog channel read the value from the signal generator such that the two readings could be compared later. A program was run on the Teensy that sampled these two channels at 1 kHz for 30 seconds and read them to the serial monitor on the PC. This data were then saved as a .csv file for further processing.

Trials were conducted using each of the twelve configuration using both an input of a DC signal of 3.3 V and a 1 V peak-to-peak sine wave, centered around 1 V with a frequency of 500 Hz. Both the AC and DC trials for each configuration were conducted 10 times.

#### 5.6.3.2 Results

The data collected as .csv files were processed and analyzed using MathWorks' MATLAB. Each data set contained a channel of data directly reflecting the applied signal, as a reference, and the signal picked up by the electrode.

In order to track the signal's accuracy, the distance was calculated between the electrode module and the measured voltages from the signal generator. As the module was expected to output unity gain, any deviation away from the generated value was considered to be an error. For the DC signal, the Euclidean distance between the input and output point was calculated and the mean value of the difference was considered to be the error.

Similarly, the expected baseline of the AC input trials was known. The amount of noise

measured within the breadboard itself was removed from the signal stream. Then, dynamic time warping (DTW) was applied to the input-—output signal pair prior to calculating the Euclidean distance between the pairs. Due to the inexact manner in which the signal was input to the electrode, it was likely that the signal reaching it became slightly out of phase and needed to be corrected. Finally, the mean of the Euclidean distance between each point was calculated to find the error. As each test was conducted ten times, the mean and standard deviation of each test was noted in Table 5.4.

Table 5.4: Descriptive statistics of the bench top testing results.

| **Configuration** | **DC Results (mV)** | | **AC Results (mV)** | |
|---|---|---|---|---|
| | **Mean Tracking Error** | **Standard Deviation** | **Mean Tracking Error** | **Standard Deviation** |
| No bias, no feedback | 0.19996 | 0.10256 | 0.19746 | 0.10614 |
| No bias, basic feedback | 0.00228 | 0.00623 | 0.21069 | 0.10011 |
| No bias, capacitive feedback | 0.10272 | 0.09044 | 0.14961 | 0.06765 |
| Resistor bias, no feedback | 0.31508 | 0.04123 | 0.37295 | 0.06072 |
| Resistor bias, basic feedback | 0.00010 | 4.43459E-05 | 0.08784 | 0.00207 |
| Resistor bias, capacitive feedback | 0.02410 | 0.01794 | 0.14416 | 0.10403 |
| Reverse diode bias, no feedback | 0.32840 | 0.03625 | 0.34165 | 0.07373 |
| Reverse diode bias, basic feedback | 0.0008 | 0.00206 | 0.16695 | 0.12859 |
| Reverse diode bias, capacitive feedback | 0.10919 | 0.11442 | 0.19713 | 0.14122 |
| Dual diode + resistor bias, no feedback | 0.29681 | 0.03386 | 0.29495 | 0.09024 |
| Dual diode + resistor bias, basic feedback | 0.00098 | 0.00134 | 0.20585 | 0.14478 |
| Dual diode + resistor bias, capacitive feedback | 0.019997 | 0.02743 | 0.15730 | 0.11905 |

It was determined that most of the configurations did not track the signal as accurately as desired. This is likely due to issues receiving the input through the conductive material, the surrounding air, and other disturbances (i.e., power line interference). While the electrode itself contains shielding, the wires that administer the signal and output it to the microcontroller are unshielded; this likely results in the presence of radio frequency interference (RFI) and electromagnetic interference (EMI) surrounding noise from the power supply, PC, cellular phones, and AC power lines.

Two different types of diode-based biasing configurations were tested: a single reverse-current diode and two back-to-back diodes with a resistor load. Chi *et al.* selected the theoretically more noisy configuration although the other one had been used earlier [80] [91]. The two were tested

and directly compared to determine which would provide better signal tracking.

The data reported from the repeated measure study with two factors was input into The Statistical Package for the Social Sciences, IBM. Here, the main effects and the interaction between the factors were analyzed using the Bonferroni adjustment. It was determined that the effects of changing the feedback type were significant, which yielded a $p$ value of 1.9 e-7 ($<<$ 0.001); conversely, the $p$ value of the bias was 0.8 and thus insignificant. These values were identical for tests of both the AC and DC datasets. Tables 5.6 and 5.5 show the isolated descriptive statistics for both the bias (Table 5.5) and the feedback (Table 5.6). As well, it was found that there is clear interaction between the bias and feedback levels; however, they do not appear to be significant due to the variations between trials.

Table 5.5: Descriptive statistics of the bias effects on bench-top testing

| **Bias** | **Mean** | **Std. Error** | **95% Confidence Interval** | |
|---|---|---|---|---|
| | | | **Lower Bound** | **Upper Bound** |
| No bias | 0.102 | 0.015 | 0.068 | 0.135 |
| Matched resistor bias | 0.113 | 0.005 | 0.101 | 0.125 |
| Reverse diode bias | 0.146 | 0.012 | 0.119 | 0.174 |
| Dual diode + resistor | 0.106 | 0.005 | 0.096 | 0.116 |

Table 5.6: Descriptive statistics of the feedback effects on bench-top testing

| **Bias** | **Mean** | **Std. Error** | **95% Confidence Interval** | |
|---|---|---|---|---|
| | | | **Lower Bound** | **Upper Bound** |
| No feedback | 0.285 | 0.014 | 0.254 | 0.316 |
| Basic feedback | 0.001 | 0.000 | -5.356E-5 | 0.002 |
| Capacitive feedback | 0.064 | 0.012 | 0.037 | 0.091 |

From the feedback results shown in Table 5.6, it is evident that the use of basic bootstrapping with all types of bias configurations preformed best; conversely, capacitive feedback of all bias configurations performed poorly. It can be determined from the interaction results that the matched resistor bias and basic feedback configuration preformed best, followed by the dual-diode bias and basic feedback. The worst preforming combinations were the matched resistor bias with no feedback and the reverse diode bias with no feedback. Still, there is little statistical significance to these specifics. While some information was gained through the bench top testing, its efficacy

is limited due to the unknown and inconsistent nature of the signal in real applications.

### 5.6.4 An attempt at on-arm testing

Though the bench-top test allowed one to observe the effects of various circuit configurations on the AFE in a known environment, further testing was conducted to understand the module's operation in more realistic conditions. Prior to conducting a proper experimental protocol, an attempt was made at observing a signal through the module while on-arm.

In order to evaluate the efficacy of the electrode and perform the desired signal processing, a reference electrode was required. An Ambu Blu gelled contact electrode was placed only the bony portion of the elbow. In order to allow the signal to be read without the use of an additional EMG collection system, a wire was soldered to the electrode's snap. The wire was then wrapped with 3M copper tape to shield the signal from RFI noise in the surrounding area.

Unlike the bench top testing, the signal applied to the electrode cannot be controlled. For the bench top test, the AC sine wave was centered around 1 V since the ADC on the Teensy 3.2 is unable to measure negative voltages; here, negative voltages were unavoidable and a new system was required. Data was collected using National Instrument's NI DAQ N19205 connected to a PC through a microUSB cable. The data was recorded through a basic visual interface using NI's LabView 2017. A DAQ assistant block was used to collect data from two channels each set at a sampling rate of 1 kHz, which is the Nyquist frequency of EMG signals. One channel is set to read from the electrode's output and the other from the gelled reference electrode. The representative voltages and the timestamps are saved as an excel file for further processing.

Through a quick trial, it was determined that the electrode module with a unity gain was unable to detect changes in muscle activities with this set up; however, the elbow flexion—extension activity was observable through the a Rigol DS1052E digital oscilloscope. In order to complete testing, a Bourns W202 potentiometer was added in parallel to the 10 MΩ resistor between pins 1 and 16 on the INA116. The potentiometer's resistance ranges from 0 to 2000 Ω; so, assuming the average EMG signal has an amplitude of 10 mV, this would allow the minimum voltage output to be 260 mV. Ideally, the rheostat was set to 500 Ω to center the voltage between 100 mV and 1 V. The gain was made to be approximately 100, which should have allowed the signal to be observed on the scope of the LabView program; however, no signal could be seen as it was overtaken by noise.

The assumption was made that the environmental noise was too large and that the shielding techniques were not executed correctly. This iteration of the module was set aside and a new one was designed.

## 5.7 A Proposed Module Design

Based upon the results of the benchtop testing and failures of the previous iterations, a final design was proposed. The remainder of this chapter will describe the design process of these modules, including the electrode structure, amplifier topology, the bias network, and the bootstrapped feedback. The final design, shown in Figure 5.17 is expected to be implemented in future works.

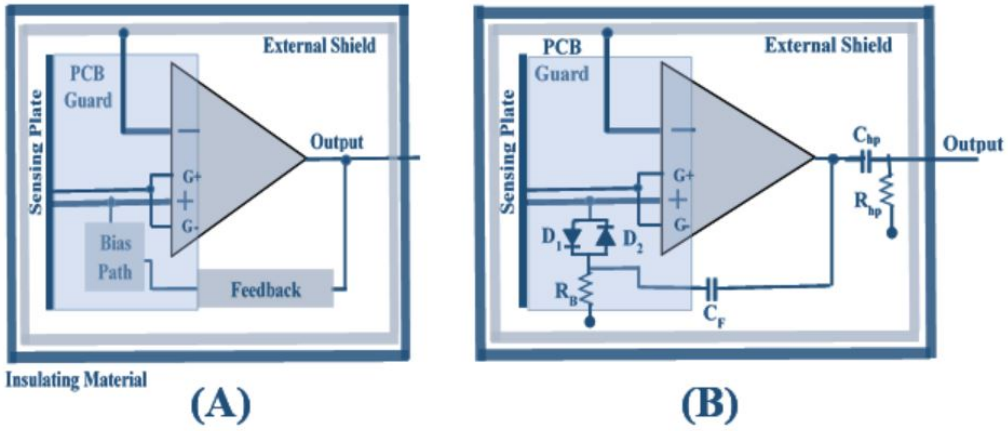


Figure 5.17: Schematic of the proposed electrode and AFE module design. (A) High-level schematic (B) Schematic including the selected bias–feedback network and high pass filter.

In Figure 5.17, image (A) shows a simplified version of the proposed design, described in Section 5.7.1. The circuit components in image (B) are described in Section 5.7.2, including the component descriptions in Table 5.7.

### 5.7.1 Topology and physical characteristic

The design is based upon the differential input topology of the INA116 instrumentation amplifier, where the sensing plate acts as the positive input terminal and the external shield acts as the negative input terminal. The internal guards on the IC for each input are tied together; as well, the

positive input's guards would be attached to the shield of a coaxial cable to provide an additional on-board guarding mechanism for the biosignal before entering the amplifier. The signal wire of the coaxial cable would be soldered to a hole through the signal layer of the PCB through to the sensing plate underneath the module. A thin insulating substrate would separate the signal and ground layers from the sensing plate, formed from 3M's copper tape.

One of the major sources of error of the previous iterations is the lack of proper insulation surrounding the electrode and analog front end structure, to rectify this, a casing would be printed from Stratysys' Tango material using the Objet Innovator 3-D printer. This material is rubber-like in texture, such that the electrode casing could form to the curvature of human body and limit mechanical disturbances due to its ability to grip to the skin. As the relative permittivity of the Tango material is approximately 2.8161 [107] and the expected size of the electrode is approximately 6.5 $cm^2$, the resultant capacitance at the interface would be dictated by Equation 5.2 and should be at minimum 150 pf, in accordance with Taheri *et al.* [106]. In order to meet this criterion, the thickness of bottom of the insulating case should be at least 0.54469 mm thick.

The interior of the insulating case, with exception of the floor, is covered with Bare Conductive's Conductive Paint to act as an external shield. The inverting input of the amplifier would be wired to an external shield surrounding the module to create an active shielded differential input. The amplifier's output is wired through a hole in the lid of the case and attached to a snap for simple use with existing EMG acquisition technologies.

### 5.7.2 Bias and feedback selection

The bias an feedback networks chosen for the proposed designs were shown visually in Figure 5.17 (B) and the corresponding components are listed in Table 5.7. The remainder of this section provides rationale for these part selections.

As the impact of introducing positive feedback to the amplifier was found to be significant through the statistical analysis of the bench-top testing in Table 5.6, it was incorporated into the proposed design. However, the type of feedback included, a capacitive bootstrap, was shown to perform most poorly. This is likely attributed to improperly chosen components, resulting in the wrong ratio in the network, and the lack of insulation surrounding Iteration 2 of the electrode module. As well, this type of bootstrap feedback has been successfully used in high-impedance bio-amplifiers for nearly forty years; in fact, many of the selected components have been modeled

| Component in Fig. 5.17 | Value / Part |
|---|---|
| D1, D2 | CMDD6001CT |
| $R_B$ | 1 MΩ |
| $C_f$ | 1 $\mu$F |
| $C_{hp}$ | 10 $\mu$F |
| $R_{hp}$ | 160 kΩ |
| Amplifier | INA116 |

Table 5.7: Circuit components of the proposed electrode design

based on the feedback network presented by Pallas-Areny [104] and Thakor and Webster [105].

The anti-parallel bias configuration was chosen for the proposed bioamplifier based on the data in Table 5.5, the descriptive statistics found from the bench-top testing of the second AFE iteration. It was found to result in the smallest error value when taking into account both the mean and standard deviation of error. During the bench-top test, standard signal diodes were used. The use of carefully selected components would further improve the impact on the bias network; in the proposed design, two CMDD6001CT diodes were placed in the anti-parallel configuration. As these diodes are intended to operate in their reverse region for this application, their low reverse-leakage current of 500 pA at 75 V would result in the desired high impedance value. As well, the selected diode has a quick switching time of 3 $\mu$s, preventing a slow operation and recovery time in EMG signal artefacts. The diode noise contribution is smaller than the proposed resistor value, 4.02259 $\mu V_{RMS}$ for 1 MΩ.

A first order passive high pass filter with a cut off frequency of 1 Hz was placed at the amplifier's output, eliminating noise content below the expected range for EMG signals.

## 5.8 Conclusion and future works

The goals of this chapter were not met; however, progress was made towards the design and development of a capacitive electrode to be used in conjunction with the biosignal acquisition sleeve. The over-arching conclusion of this chapter would be the impact of environmental noises on an amplifier's output, particularly with respect to the much smaller amplitudes of physiological signals. The partial literature review addressed these noise sources, the review of existing works described methods to mitigate such noises, and the electrode design process was largely focused on the noise arising at the dielectric interface. Techniques required for high-precision sensing

were studied, but not necessarily applied correctly, leading to the ultimate lack of success for this component of the project. The study of the impact of AFE topologies, bias, and feedback networks, such as the bench-top testing performed on Iteration 2 of the module, are a step towards better understanding of high-precision and low noise circuit applications. A final design was proposed in Section 5.7 that focused more heavily on the characteristics of the dielectric interface, on-board guarding, external shielding, additional literature, and the results of the bench-top testing. Future work includes its characterization, which can be tested through use of modules within the biosignal acquisition sleeve, including the ADS2192R and its driven right leg functionality to create a common mode reference signal.

# Chapter 6

# Conclusions and Future Works

## 6.1 Conclusions

The work presented in this thesis aimed to progress towards the development of a system to address lack of adherence to at-home physical therapy regimens for upper limb MSD patients. Initially, a literature review was conducted to examine exoskeletons and monitoring systems that tracked at least two of the following gross motions associated with the upper limb: elbow flexion–extension, forearm pronation–supination, wrist flexion–extension, and ulnar–radial deviation. Through this search, it was determined that few systems were suitable for use outside of a laboratory environment. The systems were typically tethered, cumbersome and not self-contained. As well, existing work has mostly relied on unimodal sensor input, which would limit the ability to fully characterize the motion profile data obtained from the system.

In order to address the underlying need for a more accessible way for medical professionals and patients to track MSD therapy regimens, the following system components were proposed and designed:

- a biosignal acquisition sleeve,
- an algorithm that uses EMG data to determine upper limb gross motion repetitions, and
- a proposed compatible non-geled EMG acquisition module.

The biosignal acquisition sleeve was designed as a self-contained platform to acquire both physiological and biomechanical sensor data from either a healthy subject or a patient suffering

from an upper limb MSD. It is adjustable to users of various sizes, unobtrusive, and simple to don and operate. The sensor peripherals incorporated in the sleeve are modular, such that they can be removed, adjusted, or replaced as needed. The piloted sleeve has been configured to collect biomechanical data using four inertial measurement units located proximal and distal to the elbow and wrist, two flex-bend piezo-resistive sensors located across the elbow and wrist, and two channels of EMG acquisition sensors and a driven right leg reference. A visualized tool was developed using Mathworks' MATLAB to visualize and process the data in a simple, intuitive manner to the user.

To track basic adherence to physical therapy regimens, existing algorithms were modified to count repetitions of EFE, FPS, WFE, and URD motions. The algorithm was implemented using MathWorks' MATLAB and validated using an existing database of 23 patients, which collected six channels of EMG data from each subject. The subjects ranged from healthy individuals to those who began treatment for an MSD 1–2 months prior to data collection. The repetition algorithm was then modified for use with the biosignal acquisition sleeve, capable of identifying onset–offset points of the same gross patients. This version was piloted on fifteen datasets collected amongst three healthy users.

Finally, a non-contact EMG acquisition module design was proposed to be embedded within the sleeve to be used in conjunction with the other two components. This would allow the system to collect the necessary data for the complete motion profile and the repetition detection algorithm in a modular and less obtrusive fashion than through the use of standard gelled electrodes. Another literature review was completed to inform the basis of the module's design; here, the following topics were analyzed: the nature of EMG signals, the electrode–skin interface, potential noise sources, and existing gelled, dry, and non-contact EMG acquisition methods. While three iterations of the module were designed, assembled, and tested unsuccessfully on-arm, a two-pronged approach to the design of a bioamplifier and a layered electrode structure was proposed to optimize the sensor, such that it would be capable of obtaining low-noise biosignals from the upper limb.

These three components of the work presented further the goal of developing a wearable device to monitor biosignals relating to the physical therapy regimen of an upper limb MSD. The components present the system's overarching framework through the sleeve hub, EMG sensor, and basic processing; however, significant groundwork has been laid for more elaborate sleeve electronics, extension of the EMG acquisition module to incorporate more nodes, and additional processing to provide further characterization of data collected from the biosignal acquisition sleeve.

## 6.2 Contributions

This work aimed to fill the gaps in existing systems in order to reduce barriers to adherence to upper limb MSD physical therapy regimens. The following contributions in this thesis towards this goal were:

1. Design of the electronic system to be used within the biosignal acquisition sleeve. Board schematics and PCB layouts for the proposed circuitry were completed using OrCad's EAGLE software following the selection of components. The designs proposed were as follows:

   (a) A microprocessor board, acting as a central hub for the peripherals;

   (b) An ADC board, containing a medical-grade IC to digitize acquired EMG signals with patient protection and ESD circuitry, provide a driven right-leg reference and sense temperature; and,

   (c) A power management board, containing a battery charging IC with battery protection circuitry, a rechargeable Li-ion battery, a regulator to provide a 3.3 V digital power supply, and a regulator to provide a split-rail +/- 5 V analog power supply.

2. Design and implementation of the first prototype of the ambulatory biosignal acquisition sleeve. The sleeve design allows the size and sensor site placement to be adjusted to the individual. The peripherals are incorporated in a modular fashion, such that they can be removed or interchanged within the system. In the pilot, data were collected and validated from four inertial measurement units, one flex-bend sensor, and two channels of EMG signal acquisition. The multi-modal sensor data were presented in an intuitive, visually pleasing manner and were able to provide meaningful metrics to MSD recovery, such as range of motion and muscle activity.

3. An EMG onset–offset detection algorithm was adapted for the purpose of detecting repetitions of the following gross motions of the upper limb: elbow flexion–extension, forearm pronation–supination, wrist flexion–extension, and radial–ulnar deviation. The onset and offset points were determined through each motion's muscles of interest and consequent adaptive sensitivity in threshold detection. The algorithm was tested and validated using an existing database consisting of 23 subjects, ranging from healthy to 1–2 months after

seeking treatment for MSD of the upper limb. The overall success rate was 95.43%. With modifications to limit the activity's search window, the algorithm was able to perform with a 93.33% success rate with data collected using the low-cost, ambulatory biosignal acquisition sleeve.

4. Proposal of a non-obtrusive EMG sensing module to be embedded within the biosignal acquisition sleeve. The design was based on principles existing within the literature; however, most papers focused on the ECG or EEG measurement where the signal is less erratic and contained within a smaller frequency range. The work within this thesis adapts the filtration and amplification parameters for the desired signal type. The proposed electrode's physical structure uses a unique set of available materials to re-create layers for sensing, guarding, insulation, and creating a driven shield that attaches to the analog front end PCB.

## 6.3 Future Work

While this work focuses on initial prototypes and proofs of concepts to illustrate the structure of the overall system, many of the individual components were proposed but not implemented due to lack of time, resources, and expertise. Implementation of these designs and further development would improve the system's ease-of-use, size, and comfort. Some of these modifications are as follows:

- The proposed biosignal acquisition sleeve's integrative board designs, shown in Section **??**, should be verified and fabricated. The microcontroller and peripheral ADC and power management boards should be programmed to acquire and save data from the sleeve in a manner similar to the existing prototype. As these board designs are smaller and less bulky than the current versions' components, the sleeve will be less bulky, more visually appealing, and more robust. Collection code for additional common sensing modules could be included to eliminate the need for the user to manually make these changes when taking advantage of the design's modularity.

- The data visualization application could be improved upon to increase functionality. The application should include the ability to allow the user to input custom functions, such that the user would be able to process the data to their specification. As well, the application

could be extended to include: regimen instruction information, the user's fulfillment of the regimen, the ability to track motion metrics over time, and the ability to export or share session information with a third party.

- The proposed dry electrode design presented in Section 5.7 should be fabricated, assembled, and tested. A comparative study, similar to the bench top testing performed on the earlier module iteration in Section 5.6.3, should be performed on-arm to determine the optimal low-noise, high input-impedance front end design. The electrode should be characterized and integrated into the biosignal acquisition sleeve through either the MyoWare or ADS1292R modules. This would provide an alternative solution to the gelled electrodes used in the initial prototype, improving comfort and ease of use.

- The EMG based repetition detection algorithm should be tested using data collected from the biosignal acquisition sleeve with the non-contact electrode and analog front end design, once implemented. This would further validate its efficacy with data from a variety of systems.

- A future prototype of the sleeve should be piloted on subjects in recovery from upper-limb MSDs. These individuals would be asked to provide feedback to gage the qualitative requirements of the acquisition sleeve, outlined in Section 3.2. This would allow the researcher to determine if the system is appealing to patients and if it successfully addresses some of the barriers associated with adherence to a prescribed physiotherapy regimen. Their input could be used to inform further requirements for a future version.

Though there is a significant amount of work involved in the implementation of the next prototype, the initial aims of this thesis, described in Section 1.2.1, were met. A prototype was presented of an effective, resource-conscious tool for multi-modality tracking of human upper limb motion. The biosignal acquisition sleeve was able to provide quantitative motion feedback to the user and detect the onset–offset points of motion repetitions. Continued work based upon the foundations laid in this thesis could produce a system that is more stream-lined, comfortable, and with increased feedback capabilities. With this further direction, the system could aim to be incorporated into remote physical rehabilitation regimens for upper limb MSDs.

# References


[1] O. M. of Labour. (2009) Why are pains and strains / musculoskeletal disorders (msds) a problem? [Online]. Available: http://www.labour.gov.on.ca/english/hs/pubs/pains/problem.php

[2] ——. (2009) Prevent workplace pains & strains! it's time to take action! [Online]. Available: http://www.labour.gov.on.ca/english/hs/pubs/ergonomics/is_ergonomics.php

[3] ——. (2009) Background: Recommendations on strategies to reduce work-related musculoskeletal disorders in ontario. [Online]. Available: https://www.labour.gov.on.ca/english/hs/pubs/ergonomics/erg_background.php#fn2

[4] P. H. A. of Canada, "Economic burden of illness in canada, 1993," 1997.

[5] ——, "Economic burden of illness in canada, 1997," 2002.

[6] ——, "Economic burden of illness in canada, 2005-2008," 2014.

[7] R. Campbell, M. Evans, M. Tucker, B. Quilty, P. Dieppe, and J. L. Donovan, "Why don't patients do their exercises? understanding non-compliance with physiotherapy in patients with osteoarthritis of the knee," *J. Epidemiol. Community Health*, vol. 55, no. 2, pp. 132–138, Feb 2001.

[8] E. Papi, G. M. Murtagh, and A. H. McGregor, "Wearable technologies in osteoarthritis: a qualitative study of clinicians' preferences," *BMJ Open*, vol. 6, no. 1, Jan 2016.

[9] G. Appelboom, E. Camacho, M. E. Abraham, S. S. Bruce, E. L. Dumont, B. E. Zacharia, R. D'Amico, J. Slomian, J. Y. Reginster, O. Bruyère, and J. E Sander Connolly, "Smart wearable body sensors for patient self-assessment and monitoring," *Arch Public Health*, vol. 72, no. 28, 2014.

[10] K. Jack, S. M. McLean, J. K. Moffett, and E. Gardiner, "Barriers to treatment adherence in physiotherapy outpatient clinics: A systematic review," *JMan Ther*, vol. 15, no. 3-2, pp. 220–228, Jun 2010.

[11] D. A. Neumann, *Kinesiology of the musculoskeletal system: foundations for rehabilitation*, 2nd ed. Mosby, Inc., 2010.

[12] E. S. Grood and W. J. Suntay, "A joint coordinate system for the clinical description of three-dimensional motions: application to the knee," *Journal of biomechanical engineering*, vol. 105, no. 2, pp. 136–144, 1983.

[13] G. Wu, F. C. van der Helm, H. D. Veeger, M. Makhsous, P. V. Roy, C. Anglin, J. Nagels, A. R. Karduna, K. McQuade, X. Wang, F. W. Werner, and B. Buchholz, "Isb recommendation on definitions of joint coordinate systems of various joints for the reporting of human joint motion—part ii: shoulder, elbow, wrist and hand," *Journal of Biomechanics*, vol. 38, no. 5, pp. 981 – 992, 2005. [Online]. Available: http://www.sciencedirect.com/science/article/pii/S002192900400301X

[14] P. Maciejasz, J. Eschweiler, K. Gerlach-Hahn, A. Jansen-Troy, and S. Leonhardt, "A survey on robotic devices for upper limb rehabilitation," *Journal of NeuroEngineering and Rehabilitation*, vol. 11, no. 1, p. 3, Jan 2014. [Online]. Available: https://doi.org/10.1186/1743-0003-11-3

[15] N. Jarrassé and G. Morel, "Connecting a human limb to an exoskeleton," *IEEE Transactions on Robotics*, vol. 28, pp. 697–709, 2012.

[16] T. G. Sugar, J. He, E. J. Koeneman, J. B. Koeneman, R. Herman, H. Huang, R. S. Schultz, D. E. Herring, J. Wanberg, S. Balasubramanian, P. Swenson, and J. a. Ward, "Design and control of RUPERT: a device for robotic upper extremity repetitive therapy." *IEEE Transaction on Neural Systems and Rehabilitation*, vol. 15, no. 3, pp. 336–346, sep 2007. [Online]. Available: http://www.ncbi.nlm.nih.gov/pubmed/17894266

[17] J. Ueda, D. Ming, V. Krishnamoorthy, M. Shinohara, and T. Ogasawara, "Individual muscle control using an exoskeleton robot for muscle function testing," *IEEE Transactions on Neural Systems and Rehabilitation Engineering*, vol. 18, no. 4, pp. 339–350, 2010.

[18] Z. G. Xiao, A. M. Elnady, J. Webb, and C. Menon, "Towards a brain computer interface driven exoskeleton for upper extremity rehabilitation," in *5th IEEE RAS/EMBS International Conference on Biomedical Robotics and Biomechatronics*, Aug 2014, pp. 432–437.

[19] T. Desplenter, A. Kyrylova, T. Stanbury, A. Escoto, S. Chinchalkar, and A. Trejos, "A wearable mechatronic brace for arm rehabilitation," in *IEEE RAS & EMBS International Conference on Biomedial Robotics and Biomechatronics*, Sao Paulo, Brazil, 2014, pp. 491–496.

[20] A. Kyrylova, "Development of a Wearable Mechatronic Elbow Brace for Postoperative Motion Rehabilitation," Ph.D. dissertation, The University of Western Ontario, aug 2015.

[21] L. M. Vaca Benitez, M. Tabie, N. Will, S. Schmidt, M. Jordan, and E. A. Kirchner, "Exoskeleton technology in rehabilitation: Towards an EMG-based orthosis system for upper limb neuromotor rehabilitation," *Journal of Robotics*, vol. 2013, 2013.

[22] K. Kim, K.-J. Hong, N.-G. Kim, and T.-K. Kwon, "Assistance of the elbow flexion motion on the active elbow orthosis using muscular stiffness force feedback," *Journal of Mechanical Science and Technology*, vol. 25, no. 12, pp. 3195–3203, Dec 2011. [Online]. Available: https://doi.org/10.1007/s12206-011-0923-9

[23] R.-J. Wang and H.-P. Huang, "AVSER — Active variable stiffness exoskeleton robot system: Design and application for safe active-passive elbow rehabilitation," in *IEEE/ASME International Conference on Advanced Intelligent Mechatronics*. Kaohsiung, Taiwan:

Ieee, jul 2012, pp. 220–225. [Online]. Available: http://ieeexplore.ieee.org/lpdocs/epic03/wrapper.htm?arnumber=6266034

[24] T. Ando, M. Watanabe, K. Nishimoto, Y. Matsumoto, M. Seki, and M. G. Fujie, "Myoelectric-controlled exoskeletal elbow robot to suppress essential tremor: Extraction of elbow flexion movement using STFTs and TDNN," *Journal of Robotics and Mechatronics*, vol. 24, no. 1, pp. 141–149, 2012.

[25] G. Andrikopoulos, G. Nikolakopoulos, and S. Manesis, "Design and development of an exoskeletal wrist prototype via pneumatic artificial muscles," *Meccanica*, vol. 50, no. 11, pp. 2709–2730, 2015.

[26] Z. G. Xiao and C. Menon, "Towards the development of a portable wrist exoskeleton," in *IEEE International Conference on Robotics and Biomimetics*, Phukey, Thailand, 2011, pp. 1884–1889.

[27] Z. Tang, K. Zhang, S. Sun, Z. Gao, L. Zhang, and Z. Yang, "An upper-limb power-assist exoskeleton using proportional myoelectric control." *Sensors*, vol. 14, no. 4, pp. 6677–6694, jan 2014. [Online]. Available: http://www.pubmedcentral.nih.gov/articlerender.fcgi?artid=4029719{\&}tool=pmcentrez{\&}rendertype=abstract

[28] N. Tsagarakis and D. G. Caldwell, "Development and control of a 'soft-actuated' exoskeleton for use in physiotherapy and training," *Autonomous Robots*, vol. 15, no. 1, pp. 21–33, Jul 2003.

[29] C. Carignan, J. Tang, and S. Roderick, "Development of an exoskeleton haptic interface for virtual task training," in *Proceedings of the 2009 IEEE/RSJ International Conference on Intelligent Robots and Systems*, ser. IROS'09. Piscataway, NJ, USA: IEEE Press, 2009, pp. 3697–3702.

[30] E. Rocon, A. F. Ruiz, J. L. Pons, J. M. Belda-Lois, and J. J. Sanchez-Lacuesta, "Rehabilitation robotics: a wearable exo-skeleton for tremor assessment and suppression," in *Proceedings of the 2005 IEEE International Conference on Robotics and Automation*, April 2005, pp. 2271–2276.

[31] R. A. R. C. Gopura, K. Kiguchi, and Y. Li, "Sueful-7: A 7dof upper-limb exoskeleton robot with muscle-model-oriented emg-based control," in *2009 IEEE/RSJ International Conference on Intelligent Robots and Systems*, Oct 2009, pp. 1126–1131.

[32] R. A. R. C. Gopura and K. Kiguchi, "A human forearm and wrist motion assist exoskeleton robot with emg-based fuzzy-neuro control," in *2008 2nd IEEE RAS EMBS International Conference on Biomedical Robotics and Biomechatronics*, Oct 2008, pp. 550–555.

[33] J. C. Perry, J. Rosen, and S. Burns, "Upper-limb powered exoskeleton design," *IEEE/ASME Transactions on Mechatronics*, vol. 12, no. 4, pp. 408–417, Aug 2007.

[34] A. Gupta and M. K. O'Malley, "Design of a haptic arm exoskeleton for training and rehabilitation," *IEEE/ASME Transactions on Mechatronics*, vol. 11, no. 3, pp. 280–289, June 2006.

[35] M. H. Rahman, M. Saad, J. P. Kenné, and P. S. Archambault, "Exoskeleton robot for rehabilitation of elbow and forearm movements," in *Control Automation (MED), 2010 18th Mediterranean Conference on*, June 2010, pp. 1567–1572.

[36] M. H. Rahman, M. J. Rahman, O. L. Cristobal, M. Saad, J. P. Kenné, and P. S. Archambault, "Development of a whole arm wearable robotic exoskeleton for rehabilitation and to assist upper limb movements," *Robotica*, vol. 33, no. 1, p. 19–39, 2015.

[37] F. Ozkul and D. E. Barkana, "Upper-extremity rehabilitation robot rehabroby: Methodology, design, usability and validation," *International Journal of Advanced Robotic Systems*, vol. 10, no. 12, p. 401, 2013. [Online]. Available: https://doi.org/10.5772/57261

[38] H. Zhou and H. Hu, "Human motion tracking for rehabilitation—a survey," *Biomedical Signal Processing and Control*, vol. 3, no. 1, pp. 1 – 18, 2008. [Online]. Available: http://www.sciencedirect.com/science/article/pii/S1746809407000778

[39] R. Pérez, Úrsula Costa, M. Torrent, J. Solana, E. Opisso, C. Cáceres, J. M. Tormos, J. Medina, and E. J. Gómez, "Upper limb portable motion analysis system based on inertial technology for neurorehabilitation purposes," *Sensors (Basel, Switzerland)*, vol. 10, p. 10733–10751, 2010.

[40] Z. Q. Zhang, L. Y. Ji, Z. P. Huang, and J. K. Wu, "Adaptive information fusion for human upper limb movement estimation," *IEEE Transactions on Systems, Man, and Cybernetics - Part A: Systems and Humans*, vol. 42, no. 5, pp. 1100–1108, Sept 2012.

[41] A. Alhajjar, S. Gobee, and V. Durairajah, "3d gui system for upper limb rehabilitation using electromyography and inertia measurement unit sensor feedback," in *2014 IEEE Conference on Biomedical Engineering and Sciences*, 12 2014, pp. 954–959.

[42] A. Balbinot, J. C. R. de Freitas, and D. S. Côrrea, "Use of inertial sensors as devices for upper limb motor monitoring exercises for motor rehabilitation," *"Health and Technology*, vol. 5, no. 2, pp. 91–102, Jul 2015. [Online]. Available: https://doi.org/10.1007/s12553-015-0110-6

[43] R. A. Hyde, L. P. Ketteringham, S. A. Neild, and R. J. S. Jones, "Estimation of upper-limb orientation based on accelerometer and gyroscope measurements," *IEEE Transactions on Biomedical Engineering*, vol. 55, no. 2, pp. 746–754, Feb 2008.

[44] D. Roetenberg, H. Luinge, and P. Slycke, "Xsens mvn: full 6dof human motion tracking using miniature inertial sensors. xsens motion technologies bv," XSens Inc., Tech. Rep., 2009.

[45] Y. Tian, X. Meng, D. Tao, D. Liu, and C. Feng, "Upper limb motion tracking with the integration of imu and kinect," *Neurocomputing*, vol. 159, no. Supplement C, pp. 207 – 218, 2015. [Online]. Available: http://www.sciencedirect.com/science/article/pii/S0925231215001472

[46] L. Bai, M. G. Pepper, Y. Yan, S. K. Spurgeon, M. Sakel, and M. Phillips, "Quantitative assessment of upper limb motion in neurorehabilitation utilizing inertial sensors," *IEEE Transactions on Neural Systems and Rehabilitation Engineering*, vol. 23, no. 2, pp. 232–243, March 2015.

[47] D. Vlasic, R. Adelsberger, G. Vannucci, J. Barnwell, M. Gross, W. Matusik, and J. Popović, "Practical motion capture in everyday surroundings," *ACM Trans. Graph.*, vol. 26, no. 3, Jul 2007. [Online]. Available: http://doi.acm.org/10.1145/1276377.1276421

[48] O. M. Inc. Markerless mocap for the life sciences. 2016, April. [Online]. Available: http://www.organicmotion.com/life-sciences/

[49] S. S. Corperation. (2007) Softkinetic - a sony group company - products. [Online]. Available: https://www.softkinetic.com/Products

[50] Z. Zhang, "Microsoft kinect sensor and its effect," Tech. Rep., April 2012. [Online]. Available: https://www.microsoft.com/en-us/research/publication/microsoft-kinect-sensor-and-its-effect/

[51] J. Rocha, "Skeltrak," https://github.com/joaquimrocha/Skeltrack, 2012.

[52] V. R. K. Rehabilitation. Softkinetic - a sony group company - products. [Online]. Available: http://www.virtual-reality-rehabilitation.com/products/seeme/what-is-seeme

[53] V. Group. Virtualrehab. [Online]. Available: http://www.virtualrehab.info/

[54] J. Inc. (2012) Jintronix. [Online]. Available: http://www.jintronix.com/

[55] C. D. Metcalf, S. V. Notley, P. H. Chappell, J. H. Burridge, and V. T. Yule, "Validation and application of a computational model for wrist and hand movements using surface markers," *IEEE Transactions on Biomedical Engineering*, vol. 55, no. 3, pp. 1199–1210, March 2008.

[56] P. Otten, J. Kim, and S. Son, "A framework to automate assessment of upper-limb motor function impairment: A feasibility study," *Sensors*, vol. 15, no. 8, p. 20097–20114, 2015. [Online]. Available: https://www.ncbi.nlm.nih.gov/pmc/articles/PMC4570412/

[57] N. Li, Y. Dai, R. Wang, and Y. Shao, "Study on action recognition based on kinect and its application in rehabilitation training," in *2015 IEEE Fifth International Conference on Big Data and Cloud Computing*, Aug 2015, pp. 265–269.

[58] A. Scano, M. Caimmi, A. Chiavenna, M. Malosio, and L. M. Tosatti, "Kinect one-based biomechanical assessment of upper-limb performance compared to clinical scales in post-stroke patients," in *2015 37th Annual International Conference of the IEEE Engineering in Medicine and Biology Society (EMBC)*, Aug 2015, pp. 5720–5723.

[59] J. H. M. Bergmann and A. H. Mcgregor, "Body-worn sensor design: What do patients and clinicians want?" *Annals of Biomedical Engineering*, vol. 39, no. 9, p. 2299–2312, Sep 2011. [Online]. Available: https://www.ncbi.nlm.nih.gov/pubmed/21674260

[60] A. Belsi, E. Papi, and A. H. McGregor, "Impact of wearable technology on psychosocial factors of osteoarthritis management: a qualitative study," *BMJ Open*, vol. 6, no. 2, 2016. [Online]. Available: http://bmjopen.bmj.com/content/6/2/e010064

[61] E. Papi, A. Belsi, and A. H. McGregor, "A knee monitoring device and the preferences of patients living with osteoarthritis: a qualitative study," *BMJ Open*, vol. 5, no. 9, 2015. [Online]. Available: http://bmjopen.bmj.com/content/5/9/e007980

[62] J. M. G. Merayo, P. Brauer, F. Primdahl, J. R. Petersen, and O. V. Nielsen, "Scalar calibration of vector magnetometers," *Measurement Science and Technology*, vol. 11, no. 2, p. 120, 2000. [Online]. Available: http://stacks.iop.org/0957-0233/11/i=2/a=304

[63] M. Shuster and S. Oh, "Three-axis attitude determination from vector observations," vol. 4, no. 1, pp. 70–77, 02 1981.

[64] S. O. H. Madgwick, A. J. L. Harrison, and R. Vaidyanathan, "Estimation of imu and marg orientation using a gradient descent algorithm," in *2011 IEEE International Conference on Rehabilitation Robotics*, June 2011, pp. 1–7.

[65] D. F. Stegeman and H. J. Hermens, "Standards for surface electromyography: the european project (seniam," pp. 108–112, 1998.

[66] K. A. Kaczmarek and J. G. Webster, "Voltage-current characteristics of the electrotactile skin-electrode interface," in *IEEE Engineering in Medicine & Biology Society 11th Annual International Conference*, vol. 5, Nov 1989, pp. 1526–1527.

[67] C. Assambo and M. J. Burke, "Amplifier input impedance in dry electrode ecg recording," in *2009 Annual International Conference of the IEEE Engineering in Medicine and Biology Society*, Sept 2009, pp. 1774–1777.

[68] C. J. D. Luca, L. D. Gilmore, M. Kuznetsov, and S. H. Roy, "Filtering the surface emg signal: Movement artifact and baseline noise contamination," *Journal of Biomechanics*, vol. 43, no. 8, pp. 1573 – 1579, May 2010. [Online]. Available: http://www.sciencedirect.com/science/article/pii/S0021929010000631

[69] M. B. I. Reaz, M. S. Hussain, and F. Mohd-Yasin, "Techniques of emg signal analysis: detection, processing, classification and applications," *Biological Procedures Online*, vol. 8, no. 1, Dec 2006. [Online]. Available: https://doi.org/10.1251/bpo115

[70] M. Y. Chi, "Non-contact biopotential sensing," Ph.D. dissertation, University of California, San Diego, 2011.

[71] M. A. Lopez-Gordo, D. Sanchez-Morillo, and F. P. Valle, "Dry eeg electrodes," *Sensors*, vol. 14, no. 7, pp. 12 847–12 870, 2014. [Online]. Available: http://www.mdpi.com/1424-8220/14/7/12847

[72] G. Ruffini, S. Dunne, L. Fuentemilla, C. Grau, E. Farrés, J. Marco-Pallarés, P. Watts, and S. Silva, "First human trials of a dry electrophysiology sensor using a carbon nanotube array interface," *Sensors and Actuators A: Physical*, vol. 144, no. 2, pp. 275 – 279, 2008. [Online]. Available: http://www.sciencedirect.com/science/article/pii/S0924424708001325

[73] E. Ghafar-Zadeh and M. Sawan, "Cmos capacitive sensors for lab-on-chip applications: A multidisciplinary approach (google ebook)," p. 146, 2010. [Online]. Available: http://books.google.com/books?hl=en{\&}lr={\&}id=LK6DUQJYttwC{\&}pgis=1

[74] E. Forvi, M. Bedoni, R. Carabalona, M. Soncini, P. Mazzoleni, F. Rizzo, C. O'Mahony, C. Morasso, D. G. Cassarà, and F. Gramatica, "Preliminary technological assessment of microneedles-based dry electrodes for biopotential monitoring in clinical examinations,"

*Sensors and Actuators A: Physical*, vol. 180, no. Supplement C, pp. 177 – 186, 2012. [Online]. Available: http://www.sciencedirect.com/science/article/pii/S0924424712002440

[75] L.-D. Liao, I.-J. Wang, S.-F. Chen, J.-Y. Chang, and C.-T. Lin, "Design, fabrication and experimental validation of a novel dry-contact sensor for measuring electroencephalography signals without skin preparation," *Sensors*, vol. 11, no. 6, pp. 5819–5834, 2011. [Online]. Available: http://www.mdpi.com/1424-8220/11/6/5819

[76] Y. H. Yu, S. W. Lu, L. D. Liao, and C. T. Lin, "Design, fabrication, and experimental validation of novel flexible silicon-based dry sensors for electroencephalography signal measurements," *IEEE Journal of Translational Engineering in Health and Medicine*, vol. 2, pp. 1–7, Nov 2014.

[77] P. Salvo, R. Raedt, E. Carrette, D. Schaubroeck, J. Vanfleteren, and L. Cardon, "A 3d printed dry electrode for ecg/eeg recording," *Sensors and Actuators A: Physical*, vol. 174, no. Supplement C, pp. 96 – 102, 2012. [Online]. Available: http://www.sciencedirect.com/science/article/pii/S0924424711007151

[78] J.-C. Chiou, L.-W. Ko, C.-T. Lin, C.-T. Hong, T.-P. Jung, S.-F. Liang, and J.-L. Jeng, "Using novel mems eeg sensors in detecting drowsiness application," pp. 33–36, Nov 2006.

[79] R. Matthews, P. J. Turner, N. J. McDonald, K. Ermolaev, T. M. Manus, R. A. Shelby, and M. Steindorf, "Real time workload classification from an ambulatory wireless eeg system using hybrid eeg electrodes," in *2008 30th Annual International Conference of the IEEE Engineering in Medicine and Biology Society*, Aug 2008, pp. 5871–5875.

[80] Y. M. Chi and G. Cauwenberghs, "Wireless non-contact EEG/ECG electrodes for body sensor networks," in *2010 International Conference on Body Sensor Networks*, 2010, pp. 297–301.

[81] M. K. Hazrati, H. M. Husin, and U. G. Hofmann, "Wireless brain signal recordings based on capacitive electrodes," in *2013 IEEE 8th International Symposium on Intelligent Signal Processing, WISP 2013*, no. September, 2013, pp. 8–13.

[82] J. S. Lee, J. Heo, W. K. Yu Lee, Y. G. Yu Lim, Y. H. Kim, and K. S. uk Park, "Flexible capacitive electrodes for minimizing motion artifacts in ambulatory electrocardiograms," *Sensors*, vol. 14, no. 8, pp. 14 732–14 743, Aug 2014.

[83] L. Gourmelon and G. Langereis, "Contactless sensors for surface electromyography," in *2006 28th Annual International Conference of the IEEE Engineering in Medicine and Biology*, Aug 2006, pp. 2514–2517.

[84] T. J. Sullivan, S. R. Deiss, and G. Cauwenberghs, "A low-noise, non-contact eeg/ecg sensor," in *2007 IEEE Biomedical Circuits and Systems Conference*, Nov 2007, pp. 154–157.

[85] R. Matthews, N. J. Mcdonald, I. Fridman, P. Hervieux, and T. Nielsen, "The invisible electrode – zero prep time, ultra low capacitive sensing," in *11th International Conference on Human-Computer Interaction*, 2005, pp. 22–27.

[86] Y. Sun, "Non-contact wearable body area network for driver health and fatigue monitoring," Ph.D. dissertation, Case Western Reserve University, The address of the publisher, Jun 2014.

[87] D. Svärd, A. Cichocki, and A. Alvandpour, "Design and evaluation of a capacitively coupled sensor readout circuit, toward contact-less ecg and eeg," in *2010 Biomedical Circuits and Systems Conference (BioCAS)*, Nov 2010, pp. 302–305.

[88] T. Komensky, M. Jurcisin, K. Ruman, O. Kováč, D. Laqua, and P. Husar, "Ultra-wearable capacitive coupled and common electrode-free ecg monitoring system," in *34th Annual International Conference of the IEEE Engineering in Medicine and Biology Society. IEEE Engineering in Medicine and Biology Society*, vol. 2012, 08 2012, pp. 1594–7.

[89] G. Yang, Y. Lin, and P. Bhattacharya, "A driver fatigue recognition model based on information fusion and dynamic bayesian network," *Information Sciences*, vol. 180, no. 10, pp. 1942 – 1954, 2010, special Issue on Intelligent Distributed Information Systems. [Online]. Available: http://www.sciencedirect.com/science/article/pii/S0020025510000253

[90] C.-T. Lin, L.-D. Liao, Y.-H. Liu, I.-J. Wang, and B.-S. Lin, "Novel dry polymer foam electrodes for long-term eeg measurement," *IEEE Transactions on Biomedical Engineering*, vol. 58, no. 5, pp. 1200–7, May 2011.

[91] R. J. Prance, A. Debray, T. D. Clark, H. Prance, M. Nock, C. J. Harland, and A. J. Clippingdale, "An ultra-low-noise electrical-potential probe for human-body scanning," *Measurement Science and Technology*, vol. 11, no. 3, pp. 291–7, 2000. [Online]. Available: http://stacks.iop.org/0957-0233/11/i=3/a=318

[92] T. Linz, L. Gourmelon, and G. Langereis, "Contactless emg sensors embroidered onto textile," in *4th International Workshop on Wearable and Implantable Body Sensor Networks*, vol. 13, 2007, pp. 29–34.

[93] P. W. Hodegs and B. H. Bui, "A comparison of computer-based methods for the determination of onset of muscle contraction using electromyography," vol. 101, no. 6, pp. 511–519, Dec 1996.

[94] P. Bonato, T. D'Alessio, and M. Knaflitz, "A statistical method for the measurement of muscle activation intervals from surface myoelectric signal during gait," *IEEE Transactions on Biomedical Engineering*, vol. 45, no. 3, pp. 287–299, Mar 1998.

[95] Abbink, V. D. Bilt, and V. D. Glas, "Detection of onset and termination of muscle activity in surface electromyograms," *Journal of Oral Rehabilitation*, vol. 25, no. 5, pp. 365–369, 1998. [Online]. Available: http://dx.doi.org/10.1046/j.1365-2842.1998.00242.x

[96] M. Lidierth, "A computer based method for automated measurement of the periods of muscular activity from an emg and its application to locomotor emgs," *Electroencephalography and Clinical Neurophysiology*, vol. 64, no. 4, pp. 378–380, 1986. [Online]. Available: http://www.sciencedirect.com/science/article/pii/001346948690163X

[97] G. Severini, S. Conforto, M. Schmid, and T. D'Alessio, "Novel formulation of a double threshold algorithm for the estimation of muscle activation intervals designed for variable snr environments," *Journal of Electromyography and Kinesiology*, vol. 22, no. 6, pp. 878–885, 2012. [Online]. Available: http://www.sciencedirect.com/science/article/pii/S1050641112000855

[98] K. T. Ozgunen, U. Çelik, and S. S. Kurdak, "Determination of an optimal threshold value for muscle activity detection in emg analysis," *Journal of Sports Science and Medicine*, vol. 9, no. 4, pp. 620–628, Dec 2010.

[99] G. Staude, C. Flachenecker, M. Daumer, and W. Wolf, "Onset detection in surface electromyographic signals: A systematic comparison of methods," *EURASIP Journal on Advances in Signal Processing*, vol. 2001, no. 2, pp. 67–81, Jun 2001. [Online]. Available: https://doi.org/10.1155/S1110865701000191

[100] J. F. Kaiser, "On a simple algorithm to calculate the 'energy' of a signal," in *International Conference on Acoustics, Speech, and Signal Processing*, Apr 1990, pp. 381–384.

[101] S. Solnik, P. Rider, K. Steinweg, P. DeVita, and T. Hortobagyi, "Onset detection in surface electromyographic signals: A systematic comparison of methods," *European Journal of Applied Physiology*, vol. 110, no. 3, pp. 489–498, Oct 2010. [Online]. Available: https://doi.org/10.1007/s00421-010-1521-8

[102] S. Solnik, P. DeVita, P. Rider, B. Long, and T. Hortobagyi, "Teager-kaiser operator improves the accuracy of emg onset detection independent of signal-to-noise ratio." *Acta of Bioengineering and Biomechanics*, vol. 10, no. 2, pp. 65–68, Oct.

[103] R. Haddara, "Elbow patients' data collection and analysis: An examination of electromyography healing patterns," Master's thesis, Western University, Oct 2016.

[104] R. Pallas-Areny, J. Colominas, and J. Rosell, "An improved buffer for bioelectric signals," *IEEE Transactions on Biomedical Engineering*, vol. 36, no. 4, pp. 490–493, April 1989.

[105] N. V. Thakor and J. G. Webster, "Ground-free ecg recording with two electrodes," *IEEE Transactions on Biomedical Engineering*, vol. 27, no. 12, pp. 699–704, Dec 1980.

[106] B. Taheri, R. Knight, and R. Smith, "A dry electrode for eeg recording." *Electroencephalogr Clin Neurophysiol.*, vol. 90, no. 5, pp. 376–383, May 1994.

[107] R. L. Dumene, "Manufacture and characterization of additively manufactured ceramic electromagnetic structures," Master's thesis, Virginia Polytechnic Institute, Jun 2018.

# Appendix A

# Appendix A: Iterations of sleeve electronic designs and electrode modules

## A.1 Integrated systems board design

Initially, the main electronics component was designed as a singular board. The consequent schematic and board design are presented in Figures A.1 and A.2:

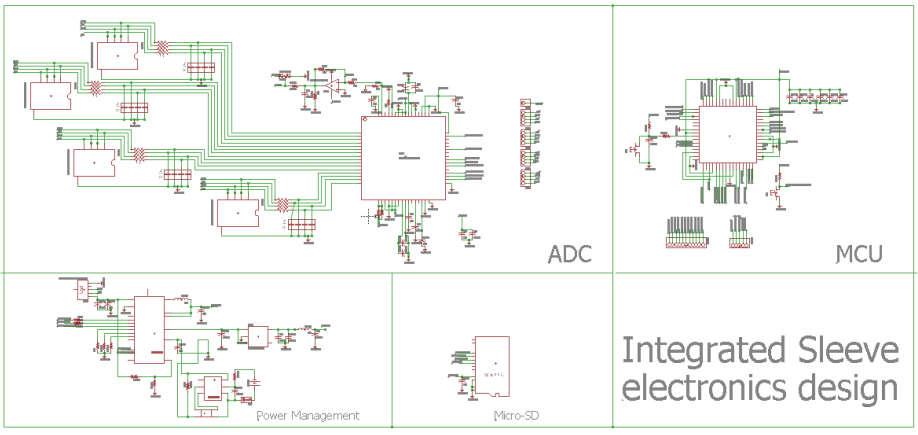


Figure A.1: Schematic of the integrated sleeve's main PCB

However, it was proven to be impractical to have this board fabricated. The design was large

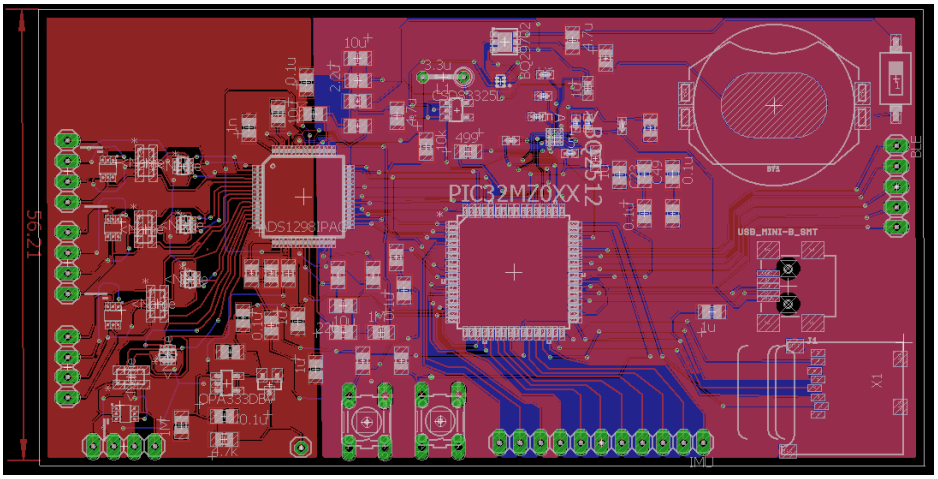


Figure A.2: Board layout of the integrated sleeve's PCB

and would have been cumbersome to attach to the sleeve itself. As well, particular portions of the board used ICs with many small pads and connections. These required extremely thin trace widths and hole sizes that either exceeded the capabilities of the manufacturing houses or scaled in price, based on board size, as the width and drill sizes were reduced.

## A.2 Power management board design

This section contains the initial design of the power management board. The schematic and board layout, created in OrCad's EAGLE 7.6.0 is displayed in Figures A.3 and A.4 below.

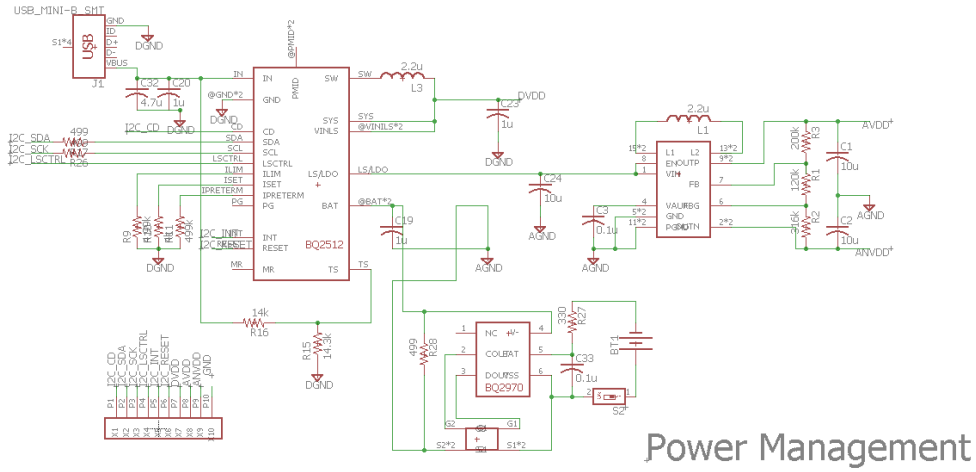


Figure A.3: Schematic diagram of the first iteration of power management circuitry

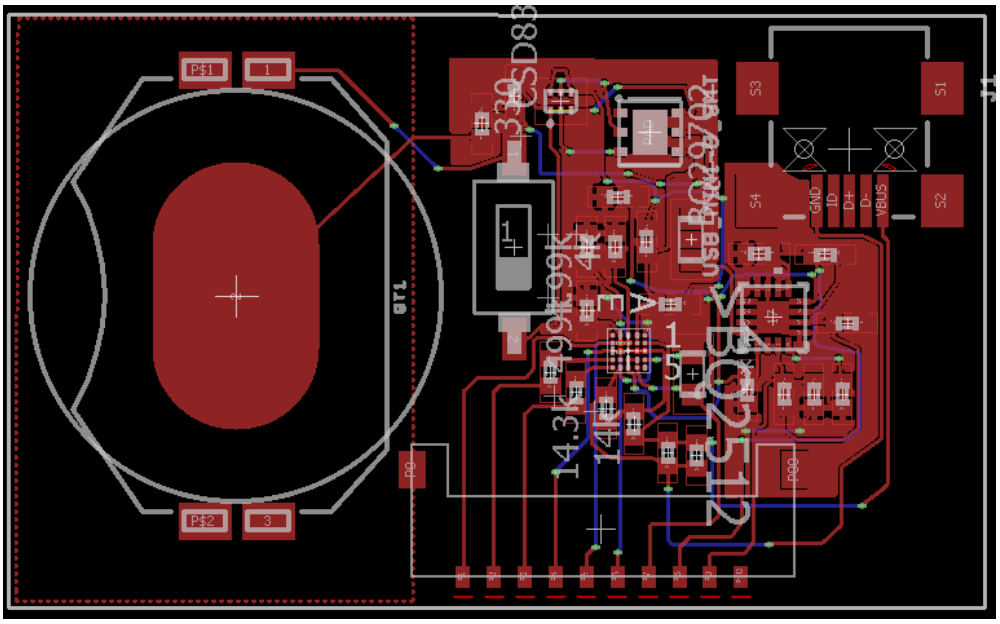


Figure A.4: Board layout of the first iteration of power management circuitry

To charge the battery, the BQ29702's output is connected to the designated terminal of Texas Instrument's BQ25121 IC. This chip has been designed specifically for power management of wearable and IoT applications; it contains a linear charger, regulated output, a load switch, and a buck converter with a low quiescent current to reduce the voltage from a 5V input. Such a power supply is introduced into the circuit via a mini-USB socket. The buck converter's output, as well as many of the chip's other features, are programmable via the MCU through its I2C channel. Here, the output voltage is set to 3.3V. This voltage can be accessed through the SYS pin and acts as the digital source for the system. It is used as a supply for the MCU, the IMU and MyoWare sensors,and the SD connector. The buck converter uses T.I.'s DCS (Direct Control with Seamless Transition into Power Saving Mode) topology, which combines hysteric, voltage, and current mode controls, and transitions between PWM and Power Save Modes without disturbances to voltage. This topology results in high accuracy voltage management with a low quiescent current, minimizing its consumption.

The LS/LDO pin is connected to an additional regulator in order to establish a separate +/- 5V analog power source for both the mixed-signal ADC and the electrode modules. A dual supply is output from this LDO, as many EMG analog front end circuit modules use differential amplification and require the use of both a positive and negative supply rail. Here, Texas Instrument's TPSXXX is incorporated to provide the desired output. The PMID pins are not needed in this application,

as the outputs are within the chip's natural range and do not require additional boost circuitry.

Insurmountable challenges presented themselves when attempting to have this board fabricated due to the ball grid array package of the BQ25121 IC. It was difficult to find a board house that was able to create trace width thin enough to prevent overlap of the signals to the chip's pads. As well, there is no machine on site capable of mounting the ball grid array chip; thus, this would have to be done externally. To have this done quickly became prohibitively expensive for a single prototype. back-and-forth communication and re-iterations of the board design, with long wait times in between correspondance, with Seeed Studio eventually lead to the discarding of this design.

## A.3 Electrode iteration 3

Regardless of the attempts to reduce noise, the environmental interference was insurmountable; consequently, another electrode module prototype was developed. This version, iteration 3, attempts to keep all components required for a clear EMG reading self-contained without increasing the sensor's size from previous versions. This iteration consists of a two-layer PCB fabricated by Seeed Studio (Shenzen, China), as well as the additional layers of copper tape and Tango-composite 3D-printed insulator materials used in design 1.3. Below are the schematic and EAGLE board design realizations of this iteration.

In this version, a SOTL-16 INA116 is the centerpiece of the design. Guard traces are placed around the positive and negative inputs and lead towards a hole through the bottom of the board; similarly, the positive input leads to a hole as well. The bypass capacitors remain at the supply pins, though the negative input pin is no longer grounded. All three bias and feedback configurations were realized and incorporated into this board: for the former, two sets of two-pin headers were placed between the shield and the input nets. The diode bias circuitry was placed across one of these headers and the resistor bias was placed across the other. Once printed, a jumper was used to create the chosen bias connection, or left open for no bias. Likewise, two sets of two-pin headers were placed across the shield net between the input and output. One connection results in basic feedback, the other to capacitive feedback, or open for no feedback. By having all of the configurations present on the board, the noise associated with breadboard and the wires heading to it are mitigated.

As well, the signal is digitized on the module itself using the 24-bit ADS1291 analog-to-digital converter. The output of the INA116 amplifier is routed to the positive input of one channel. Its negative input is grounded. A second channel is set up with amplification equal to the first channel for the connection of another electrode, which can be selected as the driven right leg signal through the chip. Following the printing and assembly of the two-layer PCB, the remainder of the module is fabricated. First, wires are soldered to the holes that pass through the board. Then, a single layer of copper fill with holes below those in the PCB layout is attached to the board using Gorilla Glue. The wires are passed through this plate.

As well, the signal is digitized on the module itself using the 24-bit ADS1291 analog-to-digital converter. The output of the INA116 amplifier is routed to the positive input of one channel. Its negative input is grounded. A second channel is set up with amplification equal to the first channel for the connection of another electrode, which can be selected as the driven right leg signal through the chip. Electrostatic discharge (ESD) circuitry was included between the signal origins and the ADC input pins. Following the printing and assembly of the two-layer PCB, the remainder of the module is fabricated. First, wires are soldered to the holes that pass through the board. Then, a single layer of copper fill with holes below those in the PCB layout is attached to the board using Gorilla Glue. The wires are passed through this plate.

A rectangular block of the same surface area as the PCB board was printed in the Tango-composite material with a Shore hardness of 50A using the Objet Innovator 3-D printer. The component had a hole through it where the connection from the sensing plate to the positive input is expected to be placed. The sensing plate was applied to the bottom of the printed interspatial material, and the wire from the PCB was passed through the rubber and soldered to the tape. Another piece of copper tape was adhered to the top of the interspatial material as the shielding plate; here, the wire from the shielding connection was soldered to the tape. The PCB structure and the tape—rubber structures are glued together. Finally, a wire was connected between the analog ground and a foil-based casing around the electronic components of the structure. Although significantly more components were included within this module, it is of comparable size to the previous iterations.

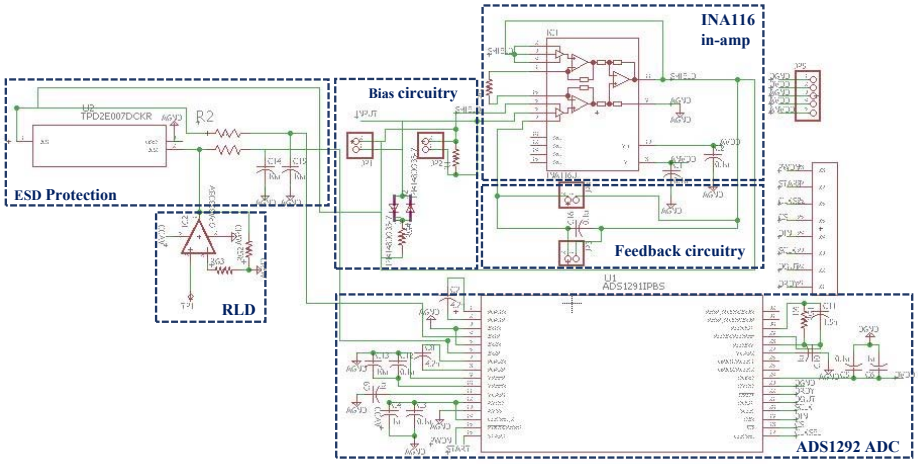


Figure A.5: Schematic of the third iteration of the electrode module.

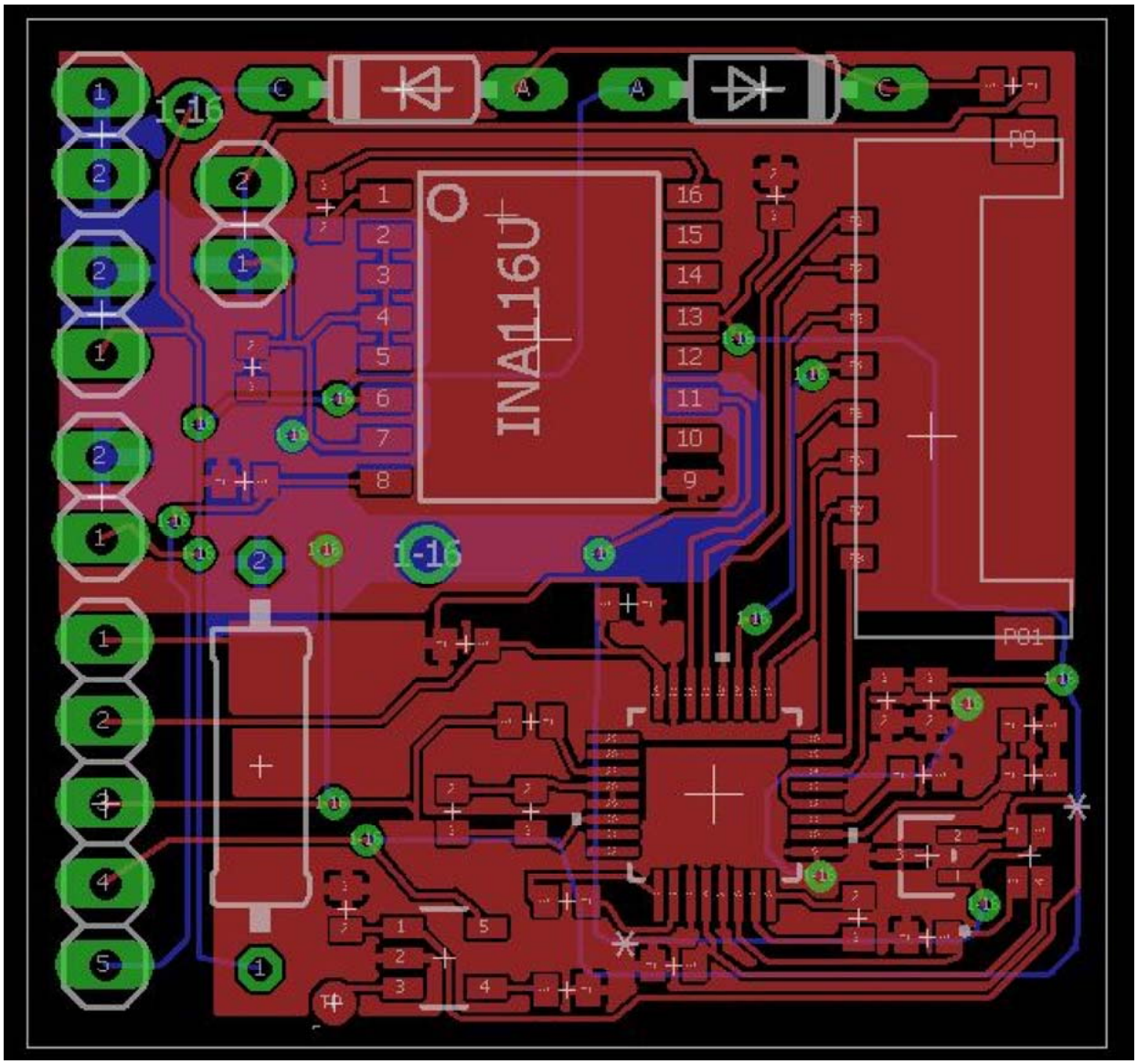


Figure A.6: EAGLE board layout of the third iteration of the electrode module.

# Appendix B

# Appendix B: Code

This appendix contains some of the scripts used to acquire and process data throughout this work.

## B.1 Biosignal Acquisition Sleeve Scripts

### B.1.1 Arduino sensor data acquisition script

*ArduinoCollect.ino*

```
// ----------------------------
//  Initialize needed libraries
// ----------------------------

#include <Wire.h>
#include <SPI.h>
#include <SparkFunLSM9DS1.h>
#include <LSM9DS1_Registers.h>
#include <SD.h>
#include <ADS.h>
//#include <TimeLib.h>
#include <String.h>

// -------------------------------------------
//    Create all possible instances of imus
// -------------------------------------------
LSM9DS1 imu1;
LSM9DS1 imu2;
LSM9DS1 imu3;
LSM9DS1 imu4;

int whichImus[] = {};
int whichAnalogs[] = {};

#define LSM9DS1_M_CS1 9
#define LSM9DS1_AG_CS1 10
#define LSM9DS1_M_CS2 7
#define LSM9DS1_AG_CS2 8
#define LSM9DS1_M_CS3 6
#define LSM9DS1_AG_CS3 5
#define LSM9DS1_M_CS4 25
#define LSM9DS1_AG_CS4 24

#define PRINT_CALCULATED
#define DECLINATION -9.1 // Declination (degrees)

String GyroString, DataString, FlexString, AnalogString;
int iNum;

// -----------------------------------------------
//  Define pins and variables for flex sensors
// -----------------------------------------------

int FLEX_PIN1 = A9;
int FLEX_PIN2 = A8;
String FlexString;
int flexNum = 0;

// -----------------------------------------------
//  Define pins and variables for analog sensors
// -----------------------------------------------
int ANum = 0;
int aPin1 = A3;
int aPin2 = A2;
int aPin3 = A5;
int aPin4 = A4;
// -----------------------------------------------
//  Define pins and variables for ADS1292
// -----------------------------------------------
ADS ADS1292;

volatile uint8_t  SPI_Dummy_Buff[30];
uint8_t DataPacketHeader[16];
volatile signed long s32DaqVals[8];
uint8_t data_len = 7;
volatile byte SPI_RX_Buff[15] ;
volatile static int SPI_RX_Buff_Count = 0;
volatile char *SPI_RX_Buff_Ptr;
volatile bool ads1292dataReceived = false;
```

```
unsigned long uecgtemp = 0;
signed long secgtemp = 0;
int y, z;
long status_byte = 0;
uint8_t LeadStatus = 0;
int chSet;
int isADC = 0;
char fileName[] = "sleeve00.csv";

// -----------------------------------------------
//  Define file and source of SD writing
// -----------------------------------------------
File dataFile;
const int SDSelect = BUILTIN_SDCARD;

// --------------------
//  Set-up sequence
// --------------------
void setup() {
  Serial.begin(115200);
  while (!Serial) ;
  Serial.flush();

  // -----------------------------------------------
  //     Initialize flex sensor inputs and count
  // -----------------------------------------------
  pinMode(FLEX_PIN1, INPUT); //Initialize flex sensors as inputs, count
  pinMode(FLEX_PIN2, INPUT);

  if (analogRead(FLEX_PIN1) > 300 && analogRead(FLEX_PIN2) > 300) {
    flexNum = 2;
  }
  else if (analogRead(FLEX_PIN1) > 100 || analogRead(FLEX_PIN2) > 100) {
    flexNum = 1;
  }
  else (flexNum = 0);

  // -----------------------------------------------
  //     Initialize analog sensor inputs and count
  // -----------------------------------------------
  pinMode(aPin1, INPUT); //Initialize flex sensors as inputs, count
  pinMode(aPin2, INPUT), pinMode(aPin3, INPUT), pinMode(aPin4, INPUT);
  int An1 = 0, An2 = 0, An3 = 0, An4 = 0;
  if (analogRead(aPin1) > 10) {
    An1 = 1;
  }
  if (analogRead(aPin2) > 500) {
    An2 = 1;
  }
  if (analogRead(aPin3) > 500) {
    An3 = 1;
  }
  if (analogRead(aPin4) > 500) {
    An4 = 1;
  }
  int Analoglist[] = {An1, An2, An3, An4};

  int As = 0;

  for (int i = 0; i <= 3; i++) {
    if (Analoglist[i] == 1) {
      whichAnalogs[As] = i + 1;
      As = As + 1;
    }
    if (Analoglist[i] == 1) {
      ANum = ANum + 1;
    }
  }
```

```
// ------------------------------------------------
// Set up SPI for IMUs, determine which are active
// ------------------------------------------------
imu1.settings.device.commInterface = IMU_MODE_SPI;
imu1.settings.device.mAddress = LSM9DS1_M_CS1;
imu1.settings.device.agAddress = LSM9DS1_AG_CS1;

imu2.settings.device.commInterface = IMU_MODE_SPI;
imu2.settings.device.mAddress = LSM9DS1_M_CS2;
imu2.settings.device.agAddress = LSM9DS1_AG_CS2;

imu3.settings.device.commInterface = IMU_MODE_SPI;
imu3.settings.device.mAddress = LSM9DS1_M_CS3;
imu3.settings.device.agAddress = LSM9DS1_AG_CS3;

imu4.settings.device.commInterface = IMU_MODE_SPI;
imu4.settings.device.mAddress = LSM9DS1_M_CS4;
imu4.settings.device.agAddress = LSM9DS1_AG_CS4;


int n;
int ONE = !(!(imu1.begin()));
int TWO = !(!(imu2.begin()));
int THREE = !(!(imu3.begin()));
int FOUR = !(!(imu4.begin()));
int IMUlist[] = {ONE, TWO, THREE, FOUR};
int Is = 0;

boolean _autocalc = true;
imu1.calibrate(_autocalc);
imu2.calibrate(_autocalc);
imu3.calibrate(_autocalc);
imu4.calibrate(_autocalc);

iNum = 0;
for (int i = 0; i <= 3; i++) {
  if (IMUlist[i] == 1) {
    whichImus[Is] = i + 1;
    Is = Is + 1;
  }
  if (IMUlist[i] == 1) {
    iNum = iNum + 1;
  }
}

// ------------------------------------------------
// Set up ADC, determine if active
// ------------------------------------------------
delay(2000);
pinMode(ADS1292_DRDY_PIN, INPUT);  //6
pinMode(ADS1292_CS_PIN, OUTPUT);    //7
pinMode(ADS1292_START_PIN, OUTPUT);  //5
pinMode(ADS1292_PWDN_PIN, OUTPUT);  //4
ADS1292.ads1292_Init();  //initalize ADS1292 slave
ADS1292.ads1292_Reg_Write(ADS1292_REG_CONFIG2, 0xA0);
ADS1292.ads1292_Reg_Write(ADS1292_REG_CONFIG1, 0b0000011);
ADS1292.ads1292_Reg_Write(ADS1292_REG_CH2SET, 0b01100000);
ADS1292.ads1292_Reg_Write(ADS1292_REG_CH1SET, 0b01100000);
ADS1292.ads1292_Reg_Write(ADS1292_REG_RLDSENS, 0b00101111);
ADS1292.ads1292_Reg_Write(ADS1292_REG_RESP1, 0b00000011);
delay(1000);
ADS1292.ads1292_Stop_Read_Data_Continuous();
delay(10);
chSet = read_ADCbyte(0x20 | 0x00);
if (chSet == 115)
{ isADC = 1;
}
ADS1292.ads1292_Start_Read_Data_Continuous();
digitalWrite(ADS1292_START_PIN, LOW);
```

```
delay(150);
ADS1292.ads1292_Start_Data_Conv_Command;

// ------------------------------------------------------
// Set up file name and create a data file to save on SD
// ------------------------------------------------------
Serial.flush();
if (!SD.begin(SDSelect)) {
  Serial.println("Card failed, or not present");
  return;
}
for (uint8_t k = 0; k < 100; k++) {
  fileName[6] = k / 10 + '0';
  fileName[7] = k % 10 + '0';
  if (! SD.exists(fileName)) {
    dataFile = SD.open(fileName, FILE_WRITE);
    Serial.println(fileName);
    break;
  }
  dataFile.close();
}


String hString;
String d = ",";
hString = "Time (ms)" + d;
String Gx = "Gx", Gy = "Gy", Gz = "Gz";
String Ax = "Ax", Ay = "Ay", Az = "Az";
String Mx = "Mx", My = "My", Mz = "Mz";

int v = 1;
String hTemp;
dataFile = SD.open(fileName, FILE_WRITE);
if (dataFile)
{
  hString = "Time,";
  if (isADC == 1) {
    hString += "ADC1" + d + "ADC2" + d;
  }

  if (iNum > 0) {
    hTemp = Gx + 1 + d + Gy + 1 + d + Gz + 1 + d + Ax + 1 + d + ...
    Ay + 1 + d + Az + 1 + d + Mx + 1 + d + My + 1 + d + Mz + 1 + d;
    hString += hTemp;
    if (iNum >= 2) {
      hTemp = Gx + 2 + d + Gy + 2 + d + Gz + 2 + d + Ax + 2 + d +...
      Ay + 2 + d + Az + 2 + d + Mx + 2 + d + My + 2 + d + Mz + 2 + d;
      hString += hTemp;
    }
    if (iNum >= 3) {
      hTemp = Gx + 3 + d + Gy + 3 + d + Gz + 3 + d + Ax + 3 + d + ...
      Ay + 3 + d + Az + 3 + d + Mx + 3 + d + My + 3 + d + Mz + 3 + d;
      hString += hTemp;
    }  if (iNum >= 4) {
      hTemp = Gx + 4 + d + Gy + 4 + d + Gz + 4 + d + Ax + 4 + d + ...
      Ay + 4 + d + Az + 4 + d + Mx + 4 + d + My + 4 + d + Mz + 4 + d;
      hString += hTemp;
    }
  }

  if (flexNum > 0) {
    hTemp = "FlexVal1"+ d+ "FlexAngle1" + d;
    hString += hTemp;
    if (flexNum == 2) {
      hTemp = "FlexVal1"+ d+"FlexAngle2" + d;
      hString += hTemp;
    }
  }
```

```
    if (ANum > 0) {
      hTemp = "Analog1" + d;
      hString += hTemp;
      if (ANum == 2) {
        hTemp = "Analog2" + d;;
        hString += hTemp;
      }
      if (ANum == 3) {
        hTemp = "Analog3" + d;;
        hString += hTemp;
      }
      if (ANum == 4) {
        hTemp = "Analog4" + d;;
        hString += hTemp;
      }
    }
    dataFile.println(hString);
    dataFile.close();
  }
  else {
    Serial.println("Error");
  }
  Serial.println(hString);
}

int read_ADCbyte(int reg_addr) {
  int out = 0;
  digitalWrite(ADS1292_CS_PIN, LOW);
  SPI1.transfer(0x20 | reg_addr);
  delayMicroseconds(5);
  SPI1.transfer(0x00);
  delayMicroseconds(5);
  out = SPI1.transfer(0x00);
  delayMicroseconds(1);
  digitalWrite(ADS1292_CS_PIN, HIGH);
  return (out);
}

String printG(int imuNum)
{
  String Gx, Gy, Gz, Ax, Ay, Az, Mx, My, Mz;
  String G;
  char buffer[10];
  String d = ",";
  switch (imuNum) {
    case 1: {
        imu1.readGyro();
        Gx = dtostrf(imu1.calcGyro(imu1.gx), 4, 2, buffer);
        Gy = dtostrf(imu1.calcGyro(imu1.gy), 4, 2, buffer);
        Gz = dtostrf(imu1.calcGyro(imu1.gz), 4, 2, buffer);
        imu1.readAccel();
        Ax = dtostrf(imu1.calcAccel(imu1.ax), 4, 2, buffer);
        Ay = dtostrf(imu1.calcAccel(imu1.ay), 4, 2, buffer);
        Az = dtostrf(imu1.calcAccel(imu1.az), 4, 2, buffer);
        imu1.readMag();
        Mx = dtostrf(imu1.calcMag(imu1.mx), 4, 2, buffer);
        My = dtostrf(imu1.calcMag(imu1.my), 4, 2, buffer);
        Mz = dtostrf(imu1.calcMag(imu1.mz), 4, 2, buffer);
      }
      break;
    case 2: {
        imu2.readGyro();
        Gx = dtostrf(imu2.calcGyro(imu2.gx), 4, 2, buffer);
        Gy = dtostrf(imu2.calcGyro(imu2.gy), 4, 2, buffer);
        Gz = dtostrf(imu2.calcGyro(imu2.gz), 4, 2, buffer);
        imu2.readAccel();
        Ax = dtostrf(imu2.calcAccel(imu2.ax), 4, 2, buffer);
        Ay = dtostrf(imu2.calcAccel(imu2.ay), 4, 2, buffer);
        Az = dtostrf(imu2.calcAccel(imu2.az), 4, 2, buffer);
```

```
        imu2.readMag();
        Mx = dtostrf(imu2.calcMag(imu2.mx), 4, 2, buffer);
        My = dtostrf(imu2.calcMag(imu2.my), 4, 2, buffer);
        Mz = dtostrf(imu2.calcMag(imu2.mz), 4, 2, buffer);
      }
      break;
    case 3: {
        imu3.readGyro();
        Gx = dtostrf(imu3.calcGyro(imu3.gx), 4, 2, buffer);
        Gy = dtostrf(imu3.calcGyro(imu3.gy), 4, 2, buffer);
        Gz = dtostrf(imu3.calcGyro(imu3.gz), 4, 2, buffer);
        imu3.readAccel();
        Ax = dtostrf(imu3.calcAccel(imu3.ax), 4, 2, buffer);
        Ay = dtostrf(imu3.calcAccel(imu3.ay), 4, 2, buffer);
        Az = dtostrf(imu3.calcAccel(imu3.az), 4, 2, buffer);
        imu3.readMag();
        Mx = dtostrf(imu3.calcMag(imu3.mx), 4, 2, buffer);
        My = dtostrf(imu3.calcMag(imu3.my), 4, 2, buffer);
        Mz = dtostrf(imu3.calcMag(imu3.mz), 4, 2, buffer);
      }
      break;
    case 4: {
        imu4.readGyro();
        Gx = dtostrf(imu4.calcGyro(imu4.gx), 4, 2, buffer);
        Gy = dtostrf(imu4.calcGyro(imu4.gy), 4, 2, buffer);
        Gz = dtostrf(imu4.calcGyro(imu4.gz), 4, 2, buffer);
        imu4.readAccel();
        Ax = dtostrf(imu4.calcAccel(imu4.ax), 4, 2, buffer);
        Ay = dtostrf(imu4.calcAccel(imu4.ay), 4, 2, buffer);
        Az = dtostrf(imu4.calcAccel(imu4.az), 4, 2, buffer);
        imu4.readMag();
        Mx = dtostrf(imu4.calcMag(imu4.mx), 4, 2, buffer);
        My = dtostrf(imu4.calcMag(imu4.my), 4, 2, buffer);
        Mz = dtostrf(imu4.calcMag(imu4.mz), 4, 2, buffer);
      }
      break;
  }
  GyroString = Gx + d + Gy + d + Gz + d + Ax + d + Ay + d ...
  + Az + d + Mx + d + My + d + Mz + d;
  return GyroString;
}

String printFlex(int flexNum)
{
  const float VCC = 3.3; // Measured voltage of Ardunio 5V line
  const float R_DIV = 47500.0; // Measured resistance of 3.3k resistor
  int flexADC ; float STRAIGHT_RESISTANCE; float BEND_RESISTANCE;
  if (flexNum == 1) {
    STRAIGHT_RESISTANCE = 37300.0; // resistance when straight
    BEND_RESISTANCE = 7406.78; // resistance at 90 deg
    flexADC = analogRead(FLEX_PIN1);
  }
  else if (flexNum == 2) {
    STRAIGHT_RESISTANCE = 17988.54; // resistance when straight
    BEND_RESISTANCE = 90000.0; // resistance at 90 deg
    flexADC = analogRead(FLEX_PIN2);
  }
  float flexV = flexADC * VCC / 1023.0;
  float flexR = R_DIV * (VCC / flexV - 1.0);
  float angle = map(flexR, STRAIGHT_RESISTANCE, BEND_RESISTANCE, 0, 90.0);

  String d = ",";
  char buffer[10];
  String angle2 = dtostrf(angle, 7, 3, buffer);
  String flexString = flexADC+d+angle2 + d;
  return flexString;
}

String printAnalog(int analogNum)
```

```
{
  String a, d = ",";
  char buffer[10];
  switch (analogNum) {
    case 1: {
        a = dtostrf(analogRead(aPin1), 4, 2, buffer);
      } break;
    case 2: {
        a = dtostrf(analogRead(aPin2), 4, 2, buffer);
      } break;
    case 3: {
        a = dtostrf(analogRead(aPin3), 4, 2, buffer);
      } break;
    case 4: {
        a = dtostrf(analogRead(aPin4), 4, 2, buffer);
      } break;
  }
  String AnalogString = a + d;
  return AnalogString;
}

String printADC() {
  int i; int j;
  digitalWrite(ADS1292_START_PIN, LOW);
  digitalWrite(ADS1292_START_PIN, HIGH);
  if ((digitalRead(ADS1292_DRDY_PIN)) == LOW)
  {
    SPI_RX_Buff_Ptr = ADS1292.ads1292_Read_Data();
    for (i = 0; i < 9; i++)
    { SPI_RX_Buff[SPI_RX_Buff_Count++] = *(SPI_RX_Buff_Ptr + i);
    }
    ads1292dataReceived = true;
  }

  if (ads1292dataReceived == true)      // process the data
  {{
      j = 0;
      for (i = 3; i < 9; i += 3)
      { uecgtemp = (unsigned long) (  ((unsigned long)SPI_RX_Buff[i + 0] << 16)  ...
      | ( (unsigned long) SPI_RX_Buff[i + 1] << 8) |  (unsigned long) SPI_RX_Buff[i + 2]);
        uecgtemp = (unsigned long) (uecgtemp << 8);
        secgtemp = (signed long) (uecgtemp);
        secgtemp = (signed long) (secgtemp >> 8);
        s32DaqVals[j++] = secgtemp;
      }
    }
  }
  char buffer[33];
  String d = ",";
  String ADC1 = ltoa(s32DaqVals[0], buffer, 10);
  String ADC2 = ltoa(s32DaqVals[1], buffer, 10);
  String ADCString = ADC1 + d + ADC2 + d;
  ads1292dataReceived = false;
  SPI_RX_Buff_Count = 0;
  return ADCString;

}


void loop() {
  String ADCString; String GyroString; String FlexString;
  String AnalogString; String DataString;
  String d = ",";

  DataString = millis() + d;
  int iN = 0, fN = 1;
  if (isADC == 1) {
    ADCString = printADC();
    DataString += ADCString;
```

```
  }

  if (iNum > 0) {
    GyroString += printG(1);
    if (iNum > 1) {
      GyroString += printG(2);
      if (iNum > 2) {
        GyroString += printG(3);
        if (iNum > 3) {
        GyroString += printG(4);
      }
      DataString += GyroString;
    }


    if (flexNum > 0) {
      FlexString += printFlex(1);
      DataString += FlexString;
      if (flexNum > 1) {
        FlexString += printFlex(2);
        DataString += FlexString;
      }
    }

    if (ANum > 0) {
      AnalogString += printAnalog(whichAnalogs[0]);
      DataString += AnalogString;
      if (ANum > 1) {
        AnalogString += printAnalog(whichAnalogs[1]);
        DataString += AnalogString;
      }
      if (ANum > 2) {
        AnalogString += printAnalog(whichAnalogs[2]);
        DataString += AnalogString;
      }
      if (ANum > 3) {
        AnalogString += printAnalog(whichAnalogs[3]);
        DataString += AnalogString;
      }
    }
    dataFile = SD.open(fileName, FILE_WRITE);
    if (dataFile) {
      dataFile.println(DataString);
      dataFile.close();
      Serial.println(DataString);
    }
  }
}
```

*SleeveCollect.ino*

```
addpath('quaternion_library');
uiopen;
filenum='SLEEVE27.';
time=eval(strcat(filenum,'Time'));
Ts=1000;

a1=[-eval(strcat(filenum,'Ay1')),-eval(strcat(filenum,'Ax1')) , eval(strcat(filenum,'Az1'))];
g1=[-eval(strcat(filenum,'Gy1')),-eval(strcat(filenum,'Gx1')), eval(strcat(filenum,'Gz1'))];
m1=[-eval(strcat(filenum,'My1')),-eval(strcat(filenum,'Mx1')), -eval(strcat(filenum,'Mz1'))];
A1=[1.8981    0.1267   -0.0890; 0    1.7398   -0.0415;  0  0  1.8930];
c1=  [0.3704,  -0.6698,   -0.5064]';
i1=m1-repmat(c1,1,length(m1))'; m1= (A1*m1')';
[c,d]=butter(3,0.1/(100/2),'high');
g1=filtfilt(c,d, g1);
windowSize = 25; b = (1/windowSize)*ones(1,windowSize); a=1;
g1 = filter(b,a, g1); a1 = filter(b,a, a1); m1 = filter(b,a, m1);
Cbn1 = TRIAD(a1(10,:)', m1(10,:)',[mean(a1(10:150,:))]', [mean(m1(10:150,:))]');
q1=dcm2quat(Cbn1);

a2=[-eval(strcat(filenum,'Ay2')), -eval(strcat(filenum,'Ax2')),eval(strcat(filenum,'Az2'))];
g2=[-eval(strcat(filenum,'Gy2')), -eval(strcat(filenum,'Gx2')), eval(strcat(filenum,'Gz2'))];
m2=[-eval(strcat(filenum,'My2')), -eval(strcat(filenum,'Mx2')),-eval(strcat(filenum,'Mz2'))];
A2= [1.8221    0.3075   -0.0007; 0    2.1160   -0.0372;  0   0    1.7718];
c2=[0.1013    0.3565     0.0562]';
i2=m2-repmat(c2,1,length(m2))'; m2= (A2*i2')';
g2=filtfilt(c, d, g2);
g2 = filter(b,a, g2);a2 = filter(b,a, a2); m2 = filter(b,a, m2);
Cbn2 = TRIAD(a2(10,:)', m2(10,:)',[mean(a2(10:150,:))]', [mean(m2(10:150,:))]');
q2=dcm2quat(Cbn2);

a3=[-eval(strcat(filenum,'Ay3')), -eval(strcat(filenum,'Ax3')), eval(strcat(filenum,'Az3'))];
g3=[-eval(strcat(filenum,'Gy3')), -eval(strcat(filenum,'Gx3')), eval(strcat(filenum,'Gz3'))];
m3=[-(eval(strcat(filenum,'My3'))), -eval(strcat(filenum,'Mx3')), -eval(strcat(filenum,'Mz3'))];
A3=[1.8938    0.2399   -0.0477;  0    1.8497   -0.0135; 0   0    1.7747];
c3 = [0.3743    0.1438     0.0605]';
i3=m3-repmat(c3,1,length(m3))'; m3= (A3*i3')';
g3=filtfilt(c, d, g3);
g3 = filter(b,a, g3); a3 = filter(b,a, a3);  m3 = filter(b,a, m3);
Cbn3 = TRIAD(a3(10,:)', m3(10,:)',[mean(a3(10:150,:))]', [mean(m3(10:150,:))]');
q3=dcm2quat(Cbn3);

a4=[-eval(strcat(filenum,'Ay4')), -eval(strcat(filenum,'Ax4')), eval(strcat(filenum,'Az4'))];
```

```
g4=[-eval(strcat(filenum,'Gy4')), -eval(strcat(filenum,'Gx4')), eval(strcat(filenum,'Gz4'))];
m4=[-(eval(strcat(filenum,'My4'))), -eval(strcat(filenum,'Mx4')), -eval(strcat(filenum,'Mz4'))];
A4 =[1.7039    0.1046    0.0729; 0    1.7736    0.0556; 0         0    1.7061];
c4 =[0.1574,   0.1399,   0.1425]';
i4=m4-repmat(c4,1,length(m4))';
m4= (A4*i4')';
g4=filtfilt(c,d, g4);
g4 = filter(b,a, g4);a4 = filter(b,a, a4); m4 = filter(b,a, m4);
Cbn4 = TRIAD(a4(10,:)', m4(10,:)',[mean(a4(10:150,:))]', [mean(m4(10:150,:))]');
q4=dcm2quat(Cbn4);


AHRS = MadgwickAHRS('SamplePeriod', 1/Ts, 'Quaternion', q1, 'Beta', 1);
AHRS2 = MadgwickAHRS('SamplePeriod', 1/Ts,'Quaternion', q2, 'Beta', 1);
AHRS3 = MadgwickAHRS('SamplePeriod', 1/Ts, 'Quaternion',q3,'Beta',  1);
AHRS4 = MadgwickAHRS('SamplePeriod', 1/Ts,'Quaternion', q4, 'Beta', 1);

quaternion1 = zeros(length(g1),4);
for t = 1:length(g1)
    AHRS.Update(g1(t,:) * (pi/180), a1(t,:), m1(t,:));  % gyroscope units must be radians
    quaternion1(t, :) = AHRS.Quaternion;
end

quaternion2 = zeros(length(g2),4);
r=zeros(length(g2),1);
for t = 1:length(g2)
    AHRS2.Update(g2(t,:) * (pi/180), a2(t,:), m2(t,:)); % gyroscope units must be radians
    quaternion2(t, :) = AHRS2.Quaternion;
end

quaternion3 = zeros(length(g3), 4);
for t = 1:length(g3)
    AHRS3.Update(g3(t,:) * (pi/180), a3(t,:), m3(t,:)); % gyroscope units must be radians
    quaternion3(t, :) = AHRS3.Quaternion;
  end


quaternion4 = zeros(length(g4)-4, 4);
for t = 1:length(g4)
    AHRS4.Update(g4(t,:) * (pi/180), a4(t,:),m4(t,:));  % gyroscope units must be radians
    quaternion4(t, :) = AHRS4.Quaternion;
 end

 %qd=quaternion1(200,:)-quaternion1(200,:);
```

```
%quaternion2=quaternion2+qd;
rUA=quat2rotm(quaternion1);
rUF=quat2rotm(quaternion2) ;
rLF=quat2rotm(quaternion3);
rH=quat2rotm(quaternion4) ;

Q1=zeros(3,3,length(rUA));
Q2=zeros(3,3,length(rUA));
Q3=zeros(3,3,length(rH));

 for i=1:length(rUF)
     Q1(:,:,i)=rUF(:,:,i)\rUA(:,:,i);
 end
Qmat1=rotm2quat(Q1);
Elbow=quat2dcm(Qmat1);
[eAlpha, eBeta, eGamma] = rad2deg(dcm2angle(Elbow, 'ZXY')) ;
figure; plot(eAlpha); title('Elbow orientation');
xlabel('Time (samples)'); ylabel('Angle (degrees)');

for i=1:length(rLF)
  Q2(:,:,i)=rLF(:,:,i)\rUF(:,:,i);
end
Qmat2=rotm2quat(Q2);
Forearm=quat2dcm(Qmat2);
[fAlpha, fBeta, fGamma] = rad2deg(dcm2angle(Forearm, 'XZY'));
figure; plot(fGamma); title('Forearm orientation');
xlabel('Time (samples)'); ylabel('Angle (degrees)');

for i=1:length(rH)
  Q3(:,:,i)=rUA(:,:,i)\rLF(:,:,i);
end
Qmat3=rotm2quat(Q3);
Wrist=quat2dcm(Qmat3);
[wAlpha, wBeta, wGamma] = rad2deg(dcm2angle(t, 'XYZ')) ;
figure; plot(wAlpha); hold on; plot(wBeta);
title('Forearm orientation');
xlabel('Time (samples)'); ylabel('Angle (degrees)');
```

### B.1.2 MATLAB IMU data processing script

*imuProcess.m*

```
addpath('quaternion_library');
uiopen;
filenum='SLEEVE27.';
time=eval(strcat(filenum,'Time'));
Ts=1000;

a1=[-eval(strcat(filenum,'Ay1')),-eval(strcat(filenum,'Ax1')) , eval(strcat(filenum,'Az1'))];
g1=[-eval(strcat(filenum,'Gy1')),-eval(strcat(filenum,'Gx1')), eval(strcat(filenum,'Gz1'))];
m1=[-eval(strcat(filenum,'My1')),-eval(strcat(filenum,'Mx1')), -eval(strcat(filenum,'Mz1'))];
A1=[1.8981    0.1267   -0.0890; 0    1.7398   -0.0415;  0  0  1.8930];
c1=  [0.3704,  -0.6698,   -0.5064]';
i1=m1-repmat(c1,1,length(m1))'; m1= (A1*m1')';
[c,d]=butter(3,0.1/(100/2),'high');
g1=filtfilt(c,d, g1);
windowSize = 25; b = (1/windowSize)*ones(1,windowSize); a=1;
g1 = filter(b,a, g1); a1 = filter(b,a, a1); m1 = filter(b,a, m1);
Cbn1 = TRIAD(a1(10,:)', m1(10,:)',[mean(a1(10:150,:))]', [mean(m1(10:150,:))]');
q1=dcm2quat(Cbn1);

a2=[-eval(strcat(filenum,'Ay2')), -eval(strcat(filenum,'Ax2')),eval(strcat(filenum,'Az2'))];
g2=[-eval(strcat(filenum,'Gy2')), -eval(strcat(filenum,'Gx2')), eval(strcat(filenum,'Gz2'))];
m2=[-eval(strcat(filenum,'My2')), -eval(strcat(filenum,'Mx2')),-eval(strcat(filenum,'Mz2'))];
A2= [1.8221    0.3075   -0.0007; 0    2.1160   -0.0372;  0   0    1.7718];
c2=[0.1013    0.3565     0.0562]';
i2=m2-repmat(c2,1,length(m2))'; m2= (A2*i2')';
g2=filtfilt(c, d, g2);
g2 = filter(b,a, g2);a2 = filter(b,a, a2); m2 = filter(b,a, m2);
Cbn2 = TRIAD(a2(10,:)', m2(10,:)',[mean(a2(10:150,:))]', [mean(m2(10:150,:))]');
q2=dcm2quat(Cbn2);

a3=[-eval(strcat(filenum,'Ay3')), -eval(strcat(filenum,'Ax3')), eval(strcat(filenum,'Az3'))];
g3=[-eval(strcat(filenum,'Gy3')), -eval(strcat(filenum,'Gx3')), eval(strcat(filenum,'Gz3'))];
m3=[-(eval(strcat(filenum,'My3'))), -eval(strcat(filenum,'Mx3')), -eval(strcat(filenum,'Mz3'))];
A3=[1.8938    0.2399   -0.0477;  0    1.8497   -0.0135; 0   0    1.7747];
c3 = [0.3743    0.1438     0.0605]';
i3=m3-repmat(c3,1,length(m3))'; m3= (A3*i3')';
g3=filtfilt(c, d, g3);
g3 = filter(b,a, g3); a3 = filter(b,a, a3);  m3 = filter(b,a, m3);
Cbn3 = TRIAD(a3(10,:)', m3(10,:)',[mean(a3(10:150,:))]', [mean(m3(10:150,:))]');
q3=dcm2quat(Cbn3);
```

```
a4=[-eval(strcat(filenum,'Ay4')), -eval(strcat(filenum,'Ax4')), eval(strcat(filenum,'Az4'))];
g4=[-eval(strcat(filenum,'Gy4')), -eval(strcat(filenum,'Gx4')), eval(strcat(filenum,'Gz4'))];
m4=[-(eval(strcat(filenum,'My4'))), -eval(strcat(filenum,'Mx4')), -eval(strcat(filenum,'Mz4'))];
A4 =[1.7039    0.1046    0.0729; 0    1.7736    0.0556; 0         0    1.7061];
c4 =[0.1574,   0.1399,   0.1425]';
i4=m4-repmat(c4,1,length(m4))';
m4= (A4*i4')';
g4=filtfilt(c,d, g4);
g4 = filter(b,a, g4);a4 = filter(b,a, a4); m4 = filter(b,a, m4);
Cbn4 = TRIAD(a4(10,:)', m4(10,:)',[mean(a4(10:150,:))]', [mean(m4(10:150,:))]');
q4=dcm2quat(Cbn4);


AHRS = MadgwickAHRS('SamplePeriod', 1/Ts, 'Quaternion', q1, 'Beta', 1);
AHRS2 = MadgwickAHRS('SamplePeriod', 1/Ts,'Quaternion', q2, 'Beta', 1);
AHRS3 = MadgwickAHRS('SamplePeriod', 1/Ts, 'Quaternion',q3,'Beta',  1);
AHRS4 = MadgwickAHRS('SamplePeriod', 1/Ts,'Quaternion', q4, 'Beta', 1);

quaternion1 = zeros(length(g1),4);
for t = 1:length(g1)
    AHRS.Update(g1(t,:) * (pi/180), a1(t,:), m1(t,:));  % gyroscope units must be radians
    quaternion1(t, :) = AHRS.Quaternion;
end

quaternion2 = zeros(length(g2),4);
r=zeros(length(g2),1);
for t = 1:length(g2)
    AHRS2.Update(g2(t,:) * (pi/180), a2(t,:), m2(t,:)); % gyroscope units must be radians
    quaternion2(t, :) = AHRS2.Quaternion;
end

quaternion3 = zeros(length(g3), 4);
for t = 1:length(g3)
    AHRS3.Update(g3(t,:) * (pi/180), a3(t,:), m3(t,:)); % gyroscope units must be radians
    quaternion3(t, :) = AHRS3.Quaternion;
  end


quaternion4 = zeros(length(g4)-4, 4);
for t = 1:length(g4)
    AHRS4.Update(g4(t,:) * (pi/180), a4(t,:),m4(t,:));  % gyroscope units must be radians
    quaternion4(t, :) = AHRS4.Quaternion;
 end
```

```
%qd=quaternion1(200,:)-quaternion1(200,:);
%quaternion2=quaternion2+qd;
rUA=quat2rotm(quaternion1);
rUF=quat2rotm(quaternion2) ;
rLF=quat2rotm(quaternion3);
rH=quat2rotm(quaternion4) ;

Q1=zeros(3,3,length(rUA));
Q2=zeros(3,3,length(rUA));
Q3=zeros(3,3,length(rH));

 for i=1:length(rUF)
     Q1(:,:,i)=rUF(:,:,i)\rUA(:,:,i);
 end
Qmat1=rotm2quat(Q1);
Elbow=quat2dcm(Qmat1);
[eAlpha, eBeta, eGamma] = rad2deg(dcm2angle(Elbow, 'ZXY')) ;
figure; plot(eAlpha); title('Elbow orientation');
xlabel('Time (samples)'); ylabel('Angle (degrees)');

for i=1:length(rLF)
  Q2(:,:,i)=rLF(:,:,i)\rUF(:,:,i);
end
Qmat2=rotm2quat(Q2);
Forearm=quat2dcm(Qmat2);
[fAlpha, fBeta, fGamma] = rad2deg(dcm2angle(Forearm, 'XZY'));
figure; plot(fGamma); title('Forearm orientation');
xlabel('Time (samples)'); ylabel('Angle (degrees)');

for i=1:length(rH)
  Q3(:,:,i)=rUA(:,:,i)\rLF(:,:,i);
end
Qmat3=rotm2quat(Q3);
Wrist=quat2dcm(Qmat3);
[wAlpha, wBeta, wGamma] = rad2deg(dcm2angle(t, 'XYZ')) ;
figure; plot(wAlpha); hold on; plot(wBeta);
title('Forearm orientation');
xlabel('Time (samples)'); ylabel('Angle (degrees)');
```

## B.2 Repetition Detection Algorithm for use on the Existing Database — MATLAB scripts

*loadup.m*

```
function [data, rVar1, rVar2]=loadUp(patientNum,motion)
location=strcat('C:\Users\gadx230\Dropbox\Raneems Data Analysis\Second Round of Trials\S',
    patientNum, '\S',patientNum,motion,'.edf');
[hdr, record] = edfread(location); %import file
samplef=4000; % sampling frequency  Hz
r=size(record);
l=r(2);

%Load, name, and filter the data for each channel of muscle information
[bb, bbFilt]=process(record(1,:),l);
[tb, tbFilt]=process(record(2,:),l);
[tbLong, tbLongFilt]=process(record(3,:),l);
[pt, ptFilt]=process(record(4,:),l);
[fcu, fcuFilt]=process(record(5,:),l);
[ecu, ecuFilt]=process(record(6,:),l);
data=[bbFilt;tbFilt;tbLongFilt;ptFilt;fcuFilt;ecuFilt];

% Based on the type of motion input, return data from the relevant channels
switch motion
    case 'EFE'
        rVar1= bb;
        rVar2= tbLong;
    case 'PS'
        rVar1= pt;
        rVar2= bb;
    case 'URD'
        rVar1= ecu;
        rVar2 = pt;
    case 'WFE'
        rVar1= fcu;
        rVar2= ecu;
    case 'HOC'
        rVar1=fcu;
        rVar2=ecu;
end

function [y,z]=process(rawsignal,l)
y = detrend(rawsignal);
```

```
%bandpass filter
[b,a]=butter(5,[10/(4000/2) ,500/(4000/2)]);
y = filtfilt(b,a,y);

%notch filter
wo = 60/(4000/2);
bw = wo/10;
[b,a] = iirnotch(wo,bw);
y = filtfilt(b,a,y);

%take the absolute value, then apply linear envelope
x=abs(y);
[c,d]=butter(5,3/(4000/2),'low');
z = filtfilt(c,d,x);

end

end
```

*repDetect.m*

```
function [ons, offs, onsTemp, offsTemp]=repDetect(y)
%Apply the TKEO
TKEO=zeros(1, length(y)-1);
for i=2:1:(length(y)-1)
    TKEO(i)=y(i)^2-y(i+1)*y(i-1);
end

%Find the absolute value of the TKEO
TKEO = abs(TKEO);
% Compute the threshold value
mu=mean(TKEO);
sigma=var(TKEO);
threshold = mu +7*sigma;

%Determine where the signal exceeds the threshold
TH=zeros(1,length(TKEO));
for i=1:1:length(TKEO)
    if TKEO(i) > threshold
        TH(i)=1;
    else
        TH(i) =0;
    end
end

j=2; k=2; l=1;flag=0; onsTemp=zeros(1,20); offsTemp=zeros(1,20);

%Determine temporary onset and offset points based on a moving window
for i=1:1:length(TH)-2000
     if sum(TH(i:i+500)) > 200 & flag==0
           if i-onsTemp(j-1) > 4000
              onsTemp(j)=i;
              flag =1;
              j=j+1;
           end
    elseif sum(TH(i:i+500))< 50 & flag==1
        if i-offsTemp(k-1) > 4000
        offsTemp(k)=i;
        flag=0;
        k=k+1;
        end
     end
end
```

```
offsTemp=offsTemp(offsTemp~=0);
onsTemp=onsTemp(onsTemp~=0);
m=1;

if length(onsTemp) > length(offsTemp)
    offsTemp=[offsTemp length(TKEO)];
end

if length(onsTemp) > 3
    for l=1:length(offsTemp)
      if offsTemp(l)-onsTemp(l) > 1500
          ons(m) = onsTemp(l);
          offs(m) = offsTemp(l);
         m=m+1;
      end
    end
 else
     for l=1:length(onsTemp)
     ons(l)=onsTemp(l);
     offs(l)=offsTemp(l);
     end
end

% Conditions for datasets that detect 4, 5, or 6 "on" and "off"
% pairs based on observations of EMG patterns
     if length(onsTemp) == 6
        for i= 1:length(ons)
            if mod(i,2)~=0
               ons(i)=ons(i);
               offs(i)=0;
            else
                ons(i)=0;
                offs (i)=offs(i);
            end
        end
     ons=ons(ons~=0);
     offs=offs(offs~=0);
     end

     if length(ons) == 4
         ons=ons(ons~=ons(4));
         offs=offs(offs~=offs(3));
     end
          ons=ons(ons~=ons(ind))
```

```
          repLengths=zeros(1, length(ons));
          for i=1:length(ons)
            repLengths(i)=offs(i)-ons(i);
          end
         [~,ind]=min(repLengths)
         if ind >1
         ons=ons(ons~=ons(ind))
         offs=offs(offs~=offs((ind)-1));
        else
             ons=ons(ons~=ons(ind+1));
             offs=offs(offs~=offs(ind));
        end
    end

    if length(ons) == 5
          for i= 1:length(ons)
             if mod(i,2)~=0
                ons(i)=ons(i);
                offs(i)=0;
             else ons(i)=0;
                 offs (i)=offs(i)
             end
          end
       ons=ons(ons~=0);
       offs=offs(offs~=0);
     end

% Add a 'safety factor', to account for further filtering (application of
% the linear envelope)
 for i=1:length(ons)
  if ons(i)> 150
     ons(i)=ons(i)-550
     if offs(i) < length(TKEO)
        offs(i)=offs(i)+500 %00
     else offs(i)=offs(i)-300;
     end
  end
 end

end
```

*createRep.m*

```
function [repData]= createRep(patientNum, motion)

[data, var1, var2]=loadUp2(patientNum);
[onsv1, offsv1]=repDetect2(var1);
[onsv2, offsv2]=repDetect2(var2);
 for i=1:length(onsv1)
   if onsv1(i) < onsv2(i)
      Reps(:,1)=onsv1(i);
   else Reps(:,1) =onsv2(i);
   end
   if offsv1(i) > offsv2(i)
     Reps(:,2)=offsv1(i);
   else Reps(:,2) =offsv2(i);
   end
 end
 repData=struct;
 for i=1:length(Reps)
   fieldName=strcat('rep',num2str(i));
   repData = setfield(repData, fieldName, data(:, Reps(i,1):Reps(i,2)));
    g=getfield(repData,fieldName);
    fileName=strcat('Subject',patientNum,motion,fieldName);
    save(fileName,'g');
  end
end
```

## CURRICULUM VITAE

| | |
|---|---|
| **Name:** | Allison Goldman |
| **Post-secondary Education and Degrees:** | Queen's University<br>Kingston, Ontario, Canada<br>2011–2015 B.Sc.<br>Electrical Engineering<br><br>The University of Western Ontario<br>London, Ontario, Canada<br>2015–2018 M.E.Sc.<br>Electrical and Computer Engineering |
| **Honours and Awards:** | Award for Outstanding Presentation in Graduate Symposium – Biomedical Systems, 2017 |
| **Related Work Experience:** | Teaching Assistant<br>The University of Western Ontario<br>*ELEC2205A – Electric Circuits I*<br>*ELEC3375B – Microprocessors*<br>*ELEC3374A – Introduction to Electronics for Mechanical Engineering*<br>*ELEC2241B – Electrical Laboratory II*<br>2015–2017<br><br>Research Assistant<br>The University of Western Ontario<br>2015–2018 |